The Education and Research 3D Radiative Transfer Toolbox – Applications to Airborne and Spaceborne Observations of Cloud and Aerosol Radiative Effects

by

Hong Chen

B.S., Florida State University, Tallahassee, 2013

M.S., Florida State University, Tallahassee, 2015

A thesis submitted to the
Faculty of the Graduate School of
the University of Colorado in partial fulfillment
of the requirement for the degree of
Doctor of Philosophy
Department of Atmospheric and Oceanic Sciences
2022

Committee Members:
K. Sebastian Schmidt
Peter Pilewskie
Michael King
O. Brian Toon
Jennifer Kay

Chen, Hong (Ph.D., Atmospheric and Oceanic Sciences)

The Education and Research 3D Radiative Transfer Toolbox – Applications to Airborne and Spaceborne Observations of Cloud and Aerosol Radiative Effects

Thesis directed by Professor K. Sebastian Schmidt

Satellite observations deliver essential information on clouds and aerosols and their radiative effects on a global scale, complemented by local and regional aircraft observations with a level of accuracy and detail that is often inaccessible from space. To obtain irradiances and radiative effects, satellite-derived cloud, aerosol and surface properties are fed into radiative transfer calculations, which can be validated with direct aircraft measurements. Often, this is only done for a fraction of the available observations, either because of the effort involved in analyzing large amounts of data, or because many real-world scenes are too complex for satellite retrievals to adequately capture. Examples include spatially inhomogeneous clouds that lead to significant biases in heritage imagery retrievals, thin clouds over bright and inhomogeneous surfaces that elude detection, and aerosols co-occurring with clouds that cannot be separately characterized without significant assumptions. The current frontier in radiation science is to embrace such challenging conditions, and confront satellite-derived radiative effects with aircraft observations systematically, rather than selectively. The Education and Research 3D Radiative Transfer Toolbox (EaR^{3}T), developed in this thesis, serves this goal. It automatically acquires data from a variety of user-selectable sources and computes irradiance and radiance fields for entire aircraft flight patterns, satellite orbits, or simulated cloud databases. It facilitates the direct comparison with independent data, enables radiative closure studies at a large scale, and provides complex synthetic training data for machine learning algorithms. The thesis showcases findings for complex atmospheric conditions that arise from a systematic use of aircraft observations with automated processing methods: (1) a third of the clouds as observed above bright surfaces during an Arctic mission were not detected by state-of-the-art satellite algorithms, and the surface variability is a more significant modulator of the shortwave cloud radiative effects than the cloud properties themselves; (2) cloud transmittance derived from geostationary imagery is biased low by 10% against aircraft observations during a tropical mission due to coarse imager resolution and cloud inhomogeneity biases; (3) regional aerosol radiative effects can be obtained from a combination of aircraft and satellite observations with fewer assumptions than in satellite algorithms. The thesis closes with a way to put novel machine learning algorithms on a physical footing, opening the door for the mitigation of complexity-induced biases in the near future.

Dedication

To

Father: Chen, Kuanlong (陈宽龙)

&

Mother: Yang, Hedi (杨荷娣)

Acknowledgement

First and foremost, I would like to express my highest gratitude to my advisor – Prof. Sebastian Schmidt, for his invaluable guidance and support, unparalleled patience and trust throughout the pursuit of my PhD. I will treasure the passion and enthusiasm he shared with me in science, and carry them with me throughout my life. My appreciation of his kindness and compassion outside scientific research is beyond what I can express in words. I will always remember his words to “be a human, have a heart” as they have been fueling me with confidence and strength to live through challenging times.

I would like to thank my former advisor – Prof. Xiaolei Zou, who lit up my passion for science and expanded my horizons during my graduate studies at Florida State University. I would also like to thank Steven Massie for his co-mentorship and generous offer of collaborative opportunities to work on various exciting research projects. My appreciation also goes to the past and present members of the atmospheric radiation group at the University of Colorado Boulder: Prof. Peter Pilewskie, Michael King, Odele Coddington, Bruce Kindel, Jeffery Drouet, Shi Song, Logan Wright, Sabrina Cochrane, Scott Kittelman, Steffen Mauceri, Julia Kent, Matthew Norgren, Vikas Nataraja, Yu-Wen Chen, Ken Hirata, and Katey Dong; all of my committee members: Prof. Peter Pilewskie, Michael King, Prof. Jennifer Kay, and Prof. Brian Toon; as well as other research professionals who have offered support to my graduate research: Prof. Hironobu Iwabuchi, Rintaro Okamura, Graham Feingold, Jake Gristey, Prof. Ming Cai, Yongjun Zheng, Zhengkun Qin, Xu Chen, Yifang Ren, Cheng Da, and Xiaoxu Tian.

During my PhD, I was fortunate enough to participate in the NASA ORACLES and CAMP^{2}Ex aircraft field campaigns. These special and valuable experiences made me appreciate the extensive resources and efforts contributed from a wide collection of research groups to successfully operate an airborne mission. I would like to express my appreciation to everyone involved in the mission projects.

I would also like to extend my gratitude to all the faculty, staff, and students from the ATOC department, especially Laurie Conway for her dedicated efforts of supporting graduate students both academically and personally.

Finally, I would like to express my deep love and sincere appreciation to my family and friends. It is all of you that make me who I am today.

Contents

DIURNAL DIRECT AEROSOL RADIATIVE EFFECTS ABOVE CLOUDS AND CLEAR SKY FROM AIRCRAFT MEASUREMENTS DURING ORACLES 2016-2018............. 104

Tables

Figures

Chapter 1

Introduction

Advanced satellite instruments, along with the development of cloud and aerosol retrieval techniques, have led to a new era of understanding regional and global cloud and aerosol radiative effects over the past two decades. The Moderate Resolution Imaging Spectroradiometer (MODIS, King et al., 1992), for example, is a passive multi-spectral imager that provides spectral radiance and reflectance measurements, which can be used to retrieve cloud and aerosol optical properties (Platnick et al., 2003; 2017; Remer et al., 2005). These optical properties are key parameters for deriving cloud and aerosol radiative effects. Satellite observations are widely used to constrain and improve numerical weather prediction models, and to advance the understanding of cloud and aerosol radiative effects in the context of their climate forcing. Meanwhile, the complexities of nature, e.g., heterogenous and bright snow surface in the Arctic, rapidly evolving clouds in the Tropics, complicated cloud and aerosol environments over polluted regions of the globe, beg the question how accurate the satellite-derived cloud and aerosol radiative effects (CRE and ARE) are under these conditions. The answer to this question is extremely important for understanding our climate system, which hinges on observations on a range of scales. It also leads to the next question how our observational system and algorithms can be improved to account for the complexities of nature.

Significant efforts have been invested into either quantifying the biases or minimizing the uncertainties associated with the satellite derived CRE and ARE. Active satellite remote sensing instruments such as lidar systems were developed, and used to perform cloud detection over bright surfaces in the Arctic (Kay and L'Ecuyer, 2013); in lower latitudes, high resolution geostationary satellite imagers are used increasingly to monitor fast evolving clouds continuously; satellite polarimeters are used to uncover the size distribution, horizontal and vertical distribution along with many other parameters for an improved characterization of atmospheric aerosols (Dubovik et al., 2019). Efforts in this regard extend beyond the advancement in space-borne instruments and measurement techniques – many aircraft field campaigns and airborne observations served as an important, in-detail observations of CRE and ARE, especially when clouds and aerosols occur in close proximity.

Compared to the space-borne observations, the advantages of airborne observations from an atmospheric radiation perspective lie in 1) their capability of providing not only remote sensing measurements of radiance but also radiative energy measurements of irradiance that cannot be measured by space-borne instruments, along with in-situ observations of cloud and aerosol microphysics and optical properties, 2) their superiority of providing observations at a much finer temporal and spatial scale, 3) their flexibility of taking measurements above, below, and within cloud and/or aerosol layers, providing constraints of radiative forcing that space-borne observations cannot deliver. These features of aircraft observations make them suitable for validating satellite observations and the associated retrieval-based radiative effects, evaluating atmospheric radiation processes at a finer scale such as 3D cloud radiative effects (detailed explained in Chapter 3), and developing techniques of directly deriving cloud and aerosol radiative effects from observations.

In the past, aircraft observations have been used extensively to evaluate satellite-derived CRE and ARE, to expand the understanding of CRE and ARE such as quantifying the 3D biases affecting cloud and aerosol radiative effects obtained through traditional radiative transfer approach, and to generally advance the development in algorithms for deriving CRE and ARE.

This was mostly done based on select cases, usually referred to as “golden cases”, e.g., cases where aircraft flew during a particular satellite overpass or over a ground or ship instrument. These “golden cases” usually consist of one or a few flight track segments that are coordinated with the other space/ground/ship instrument. For example, Schmidt et al. (2007) studied two particular cases from the Cirrus Regional Study of Tropical Anvils and Cirrus Layers – Florida Area Cirrus Experiment (CRYSTAL-FACE) that utilized aircraft measurements of spectral irradiance from the Solar Spectral Flux Radiometer (SSFR) to validate legacy cloud retrievals from the Moderate Resolution Imaging Spectroradiometer (MODIS) airborne simulator (MAS). 3D radiative transfer calculations based on MAS cloud retrievals were performed through a 3D Monte Carlo radiative transfer (RT) model (RTM), and intercompared with SSFR measured irradiance to gain insights of satellite-derived, e.g., MODIS, cloud radiative properties such as cloud albedo. Song et al. (2016) studied a case from the Tropical Composition, Cloud and Climate Coupling Experiment (TC^4) that utilized the approach developed by Schmidt et al. (2010a) to quantify the 3D biases in cloud transmittance associated with inhomogeneities of cloud fields. The case study revealed that 3D effects can contribute a bias of ±12-19% in traditional imagery-derived cloud transmittance. LeBlanc et al. (2012) studied two selected cases from two different aircraft campaigns – one flight from the Arctic Research of the Composition of the Troposphere from the Aircraft and Satellites (ARCTAS) and one flight from the Nexus of Air Quality and Climate Change (CalNex) to access an improved algorithm that can derive spectral aerosol optical depth from vertical aerosol extinction profile from the perspective of spectral relative forcing efficiency of aerosols. Additionally, case studies of aircraft observations have been used in many other studies in validating satellite derived CRE and ARE (Coddington et al., 2010), in evaluating 3D effects of

CRE and ARE (Schmidt et al., 2010a), and in developing measurement techniques for estimating CRE and ARE (Schmidt et al., 2010b).

Case studies further the understanding of atmospheric processes, and often elicit new scientific questions, while allowing to test scientific hypotheses through qualitative analysis of airborne along with space-borne observations. In addition to “case study mode”, an inclusive approach, which utilizes more data from field mission, has been gradually adapted to airborne radiation science. For example, instead of only studying selected “golden cases” of limited flight track segments, Cochrane et al. (2019) utilized aircraft observations from an entire field campaign to derive aerosol optical properties such as asymmetry parameter, single scattering albedo, followed by an aircraft observational based parameterization of direct aerosol radiative effects for the whole study region of the field campaign (Cochrane et al., 2021). The parameterization obtained from collective use of the data allows to capture both the properties of aerosols and clouds as well as their radiative effects, and it serves as constraints for satellite observations and modeling studies of various kinds, with minimum assumptions that are necessary in retrieval-based approaches.

Although the inclusive approach is more powerful as a tool for validating satellite-derived CRE and ARE, the transition from case studies has been slow, in part because real-world conditions during field campaigns are often too complex to lend themselves to analysis. This proved limiting for addressing the challenges in radiation science of our time, which are precisely the kinds of complex conditions that make analysis difficult and introduce systematic biases in the space-borne quantification of atmospheric radiative effects. The gap for the transition was an automated tool capable of reconstructing spatially complex scenes from a variety of data sources, and of subsequent automated 3D-RT calculations. Only automated processing of a large number of scenes, up to entire field missions, was going to break through these limitations, and this thesis addresses this challenge.

It will provide several examples that demonstrate how to approach atmospheric radiation problems by using aircraft and satellite observations statistically, as opposed to using isolated cases as done in many past radiation science studies, for answering a number of science questions as outlined below. To this end, I developed a toolbox – the Education and Research 3D Radiative Transfer Toolbox (EaR^{3}T, described in Section 1.4 and in Chapter 3), that can meet the need for extensive and automated 1D and 3D radiative transfer calculations required by the aforementioned inclusive approach.

Three science questions are addressed in the subsequent chapters of this thesis:

1. *What is the accuracy of satellite imagery-derived cloud radiative effects of thin clouds over ice as sampled during a NASA aircraft campaign in the Arctic?* (Chapter 2)

The Arctic is a challenging place on Earth to accurately quantify cloud radiative effects with satellite observations, and yet is only rarely sampled with aircraft, let alone surface-based observations. The surface, which is both bright and heterogeneous, makes traditional cloud detection algorithms and cloud retrieval algorithms challenging as they require accurate knowledge of surface albedo in the shortwave wavelength range to distinguish clouds from the surface. Platnick et al. (2001) proposed an improved cloud retrieval algorithm that instead of utilizing reflectance at visible wavelength, uses the shortwave-infrared wavelengths of 1630 nm and 2130 nm for retrieving cloud optical properties (referred to as "1621" cloud product) over snow surface, as snow and ice at those two wavelengths are dark and vary little. Still, Wendisch et al. (2019) showed that a third of clouds are missed from cloud detection through intercomparison of cloud fraction derived from MODIS and aircraft observations. This issue provided the motivation to evaluate satellite-derived CRE in the Arctic, and led to the work shown in Chapter 2. It evaluated the spectral and broadband irradiance calculated from the MODIS “1621” cloud product in the Arctic against aircraft measurements collected during the Arctic Radiation-IceBridge Sea and Ice Experiment (ARISE, described in Section 1.1). Specifically, the upwelling and downwelling shortwave spectral and broadband irradiance measured by the Solar Spectral Flux Radiometer (SSFR, described in Section 1.2) and the BroadBand Radiometer system (BBR, described in Chapter 2) were used to intercompare with MODIS-derived spectral and broadband irradiance pixel-by-pixel for two flight days – one above clouds and one below clouds. I aimed at obtaining the best-possible satellite-derived CRE in the Arctic to validate both MODIS capabilities of detecting and correctly characterizing clouds through the “1621” cloud product. Going beyond the challenges we face for clouds, the heterogeneity of the snow/ice surface in the Marginal Ice Zone (MIZ) of the Arctic is also a key factor that can alter the CRE. To account for the heterogeneous surface, I developed a spectral surface albedo parameterization, which utilizes clear-sky near-surface observations of aircraft camera imagery and SSFR measured albedo during multiple flights to statistically characterize surface albedo for the bright and dark regions of the MIZ. Finally, I answered the question by attributing the source of biases in satellite-derived CRE through a spectral dependence and variation analysis for the measured and calculated irradiance along the flight track. The aforementioned RT calculations based on MODIS were performed in a highly automated fashion, which was the precursor and motivation for EaR^{3}T. Encouraged by the insights gained from the statistical assessment of satellite-derived CRE in the Arctic, I turned my eye to the Tropics, where the heterogeneous cloud environment and fast changing clouds are extremely challenging for obtaining an accurate CRE representation from satellite observations. This allowed me to address the second science question:

2. *What is the accuracy of satellite imagery-derived cloud radiative effects of heterogeneous clouds as sampled during a NASA aircraft campaign in the Philippine tropics?* (Chapter 3)

The opportunity for answering this question was afforded to me by the Cloud, Aerosol and Monsoon Processes Philippines Experiment (CAMP^{2}Ex, described in Section 1.1), an aircraft campaign by NASA in 2019. Fortunately enough, NASA CAMP^{2}Ex collaborated with the Meteorological Satellite Center (MSC) of the Japanese Meteorological Agency (JMA), and so imagery from the Advanced Himawari Imager (AHI) onboard the geostationary satellite Himawari-8 was made available to the mission team. AHI takes continuous multi-channel reflectance measurements every 10 minutes to monitor the lifecycle of clouds, among other applications. The AHI reflectance can be fed into legacy cloud retrieval algorithms to produce cloud products. Moreover, I built upon the code base from the previous chapter and developed the EaR^{3}T, a toolbox that can automate the 1D and 3D-RT calculations for airborne and spaceborne radiation science. The availability of abundant data from CAMP^{2}Ex and AHI, and the capability of performing large-scale RT calculations with EaR^{3}T enable systematic intercomparisons between satellite imagery derived CRE and aircraft measurements. Specifically, 1D and 3D downwelling irradiance calculations were performed by EaR^{3}T using AHI cloud products, and compared with irradiance measurements from the Spectral Sunshine Pyranometer (SPN-S, described in Section 1.2) for all the below-cloud flight tracks during the entire CAMP^{2}Ex mission. These systematic intercomparisons between 3D-RT calculations and observations (for the first time with data from an entire field mission) allowed to quantify the bias associated with traditional 1D cloud retrieval in satellite imagery derived CRE.

While working on the quantification of imagery-derived biases in cloud radiative effects, a new cloud retrieval approach was being developed in the group, with the potential to mitigate 3D-RT biases in passive imagery cloud retrievals. Rather than mapping cloud reflectance to cloud optical thickness (COT) on a pixel-by-pixel basis, without considering the spatial context of a pixel as done in the heritage independent pixel approximation (IPA), it takes the context of a pixel into account. This context-aware Convolutional Neural Network (CNN) was developed by Nataraja et al. (2022, described in Section 1.5) in our group, where EaR^{3}T provided synthetic training data based on large eddy simulation (LES) data.

In this thesis (Chapter 3), the newly developed CNN, as well as the heritage IPA were applied to measurements for the very first time. I used high-resolution airborne imagery collected by an all-sky camera (described in Section 1.2) deployed during CAMP^{2}Ex to retrieve COT fields, and subsequently validated the outcome. For this validation, independent ground truth data was unavailable in addition to the imagery itself. Therefore, I developed a new validation metric, called ‘radiance self-consistency’, which can be applied to any imagery-based cloud retrievals. It uses 3D radiance calculations through EaR^{3}T based on given cloud retrievals, e.g. CNN-COT field, to validate against satellite radiance measurements themselves, which are always available. The consistency between the COT-generated 3D radiance and satellite measured radiance could give quality assessment for the COT.

Having studied cloud radiative effects for two challenging atmospheric conditions in two opposite climate zones – for thin clouds over bright surfaces in the Arctic and for spatially complex clouds in the Tropics, I now use the capabilities of automated data processing to study the radiative effects of aerosols in the presence of clouds, another area where satellite observations alone are currently challenged. A NASA field campaign – the ObseRvations of Aerosols above CLouds and their intEractionS (ORACLES, 2016-2018, described in Section 1.1) was dedicated to study clouds and aerosols in the southeast (SE) Atlantic – a region of the globe with biomass burning (BB) aerosols overlying a semi-permanent boundary layer cloud layer, with the central science question:

What is the direct radiative effect of the African biomass burning aerosol layer in clear- and cloudy-sky conditions over the SE Atlantic?

The question cannot be answered with aircraft measurements alone as they have limited spatial and temporal coverage. The successful use of geostationary satellite observations during the CAMP^{2}Ex study gave rise to the idea that the ORACLES science question could be addressed by relying on the relative strengths of both geostationary satellite observations (extensive regional and temporal coverages) and aircraft observations (accuracy of in-situ observations; resolution etc.) as discussed above, in order to arrive at the best estimate of the direct aerosol radiative effect (DARE). How to do this specifically is encompassed by the specific question underlying Chapter 4 of this thesis:

3. *How can detailed, accurate aircraft observations be combined with spatially and temporally extended satellite imagery to obtain the best estimate of the direct aerosol radiative effect for the study region of a set of NASA campaigns in the southeast Atlantic?* (Chapter 4)

The most commonly used approach for the evaluation of DARE derived from satellite cloud and aerosol products is through the evaluation of the satellite retrieval products against cloud and aerosol aircraft observations (Peers et al., 2021), and that was the original path here as well (see Section 1.3): to quantify the effect of the aerosol layer on COT retrievals from polar-orbiting and geostationary imagers, SSFR cloud retrievals were generated from all the below-aerosol above-cloud flight legs (referred to as BOL), where the aerosol effects on cloud retrievals are minimal, during the entire three-year campaign, and compared those against SSFR retrievals from a higher altitude, where the aerosol layer does affect the retrieval. This work was published by Chang et al. (2021).

Ultimately, it became clear that the cloud retrieval was biased not only by the aerosol layer, but also by cloud spatial inhomogeneities. Since the most important parameter for DARE besides the aerosol loading itself is the albedo that the aerosol layer experiences, the combined uncertainties in this parameter given aerosol-induced and cloud variability-induced biases made the retrieval-based approach impractical. Instead, I sought to arrive directly at DARE from aircraft observations, bypassing imagery-based cloud and aerosol retrievals. This was made possible by the work of Cochrane et al. (2021) who developed a parameterization of the instantaneous DARE parameterization based on the aircraft observations collected during ORACLES (referred to as C21). C21 can provide instantaneous broadband DARE estimates at any location of the campaign region based on minimum inputs such as mid-visible scene albedo and aerosol optical depth, both of which are available from direct aircraft observations.

This observationally based DARE parameterization avoids the error associated with various assumptions made in the aforementioned retrieval-to-DARE approach. On the other hand, DARE can also not be derived from aircraft measurements exclusively, even from the entire campaign. That is because the aircraft measurements alone do not fully represent the DARE of the study region as 1) diurnal variation of aerosols and clouds, especially clouds, are not considered, and 2) the spatial coverage of the aircraft measurements is limited. These two challenges can be resolved if geostationary satellite observations can be used as they offer extensive spatial and temporal coverage. Therefore, I incorporated geostationary satellite observations from the Spinning Enhanced Visible and InfraRed Imager (SEVIRI) with aircraft observations from ORACLES and developed a statistical based mapping that can directly translate SEVIRI measured reflectance into BOL scene albedo (referred to reflectance-to-albedo mapping). Such mapping allows diurnal and domain scene albedo to be obtained from SEVIRI as reflectance measurements that are taken every 15 minutes for the entire ORACLES study region throughout the day. Diurnal DARE for any given region can then be obtained from C21 based on the SEVIRI-derived scene albedo and aerosol properties from aircraft measurements. With the diurnal DARE, diurnally integrated DARE can be calculated by averaging the diurnal DARE over the course of the day. The combined process of 1) reflectance-to-albedo mapping, 2) DARE estimate from C21, and 3) integration of diurnal DARE into diurnally-integrated DARE is referred to as the diurnal DARE method. It enables the exploration of DARE at different temporal scales ranging from days to months, and at different spatial scales ranging from degree-size grid box to the entire study region, which addresses the ORACLES central science question.

The works of Chapter 2, 3, and 4 can be found in the following peer-review publications:

- Chen, H., Schmidt, S., King, M. D., Wind, G., Bucholtz, A., Reid, E. A., Segal-Rozenhaimer, M., Smith, W. L., Taylor, P. C., Kato, S., and Pilewskie, P.: The Effect of Low-Level Thin Arctic Clouds on Shortwave Irradiance: Evaluation of Estimates from Spaceborne Passive Imagery with Aircraft Observations, Atmos. Meas. Tech., 14, 2673–2697, https://doi.org/10.5194/amt-14-2673-2021, 2021.

- Chen, H., Schmidt, S., Massie, S. T., Nataraja, V., Norgren, M. S., Gristey, J. J., Feingold, G., Holz, R. E., and Iwabuchi, H.: The Education and Research 3D Radiative Transfer Toolbox (EaR^{3}T) – Towards the Mitigation of 3D Bias in Airborne and Spaceborne Passive Imagery Cloud Retrievals, Atmos. Meas. Tech. Discuss. [preprint], https://doi.org/10.5194/amt-2022-143, in review, 2022.

- Chen, H., Schmidt, S, Cochrane, S. P., Mallet, M., LeBlanc, S. E., Redemann, J., Pistone, K., Kacenelenbogen, M., Rozenhaimer, M. S., and Burton, S.: Diurnally Integrated Direct Aerosol Radiative Effect above Clouds and Clear-Sky from Aircraft Measurements during ORACLES 2016-2018, Atmos. Meas. Tech., *to be submitted*, 2022.

1.1 Field Campaigns

The data used in this thesis were collected during three field campaigns – 1) the Arctic Radiation-IceBridge Sea and Ice Experiment (ARISE, 2014), 2) the Cloud, Aerosol and Monsoon

Processes Philippines Experiment (CAMP^{2}Ex, 2019), and 3) the ObseRvations of Aerosols above CLouds and their intEractionS (ORACLES, 2016-2018). These three field campaigns were all funded by the National Aeronautics and Space Administration (NASA). ARISE was NASA's first Arctic aircraft campaign that focused on studying the cloud properties and radiative effects in the Arctic for a better understanding of Arctic sea ice decline and associated climate change (Smith et al., 2017). The campaign was executed in September 2014 based at Eielson Air Force Base (AFB) near Fairbanks, Alaska. A NASA C-130 aircraft carried a comprehensive set of remote sensing and in-situ instruments for measuring surface and cloud properties. More details of ARISE are described in Section 2.2.

CAMP^{2}Ex aimed at characterizing the coupling of aerosol processes, cloud physics, and atmospheric radiation during Monsoon season at the synoptic scale (Reid et al., 2022). The campaign was conducted from August to October in 2019 based at Clark International Airport in the Philippines. A NASA P-3 aircraft was deployed to carry advanced remote sensing and in-situ instruments to take measurements of clouds and aerosols. The Meteorological Satellite Center (MSC) of the Japanese Meteorological Agency provided high resolution geostationary satellite imagery from the Advanced Himawari Imager (AHI) onboard Himawari-8 for monitoring the fast-changing cloud environments over the study region. A more detailed instrumentation is described in Section 3.2.

ORACES was a three-year NASA aircraft field campaign to study the biomass burning aerosols and their influence on regional and global climate (Redemann et al., 2021). The campaign was executed from the end of August to the end of September in 2016, from early August to early September in 2017, and from late September to late October to cover the active African burning season. ORACLES 2016 was based at the Walvis Bay International Airport near the west coast of

Namibia. For ORACLES 2017 and 2018, the mission was based at the international airport of São Tomé and Príncipe. The NASA P-3 aircraft was deployed during the entire three-year ORACLES mission, while a NASA ER-2 aircraft was only deployed during the first year of ORACLES. A few changes were made to the instrumentation and measurement techniques to compensate for the unavailability of the ER-2 aircraft for ORACLES 2017 and 2018 due to various logistic reasons. A comprehensive set of advanced active and passive remote sensing, as well as in-situ instruments were deployed to make direct measurements of aerosol and cloud radiative properties. A detailed overview of the ORACLES mission can be found at Redemann et al. (2021), and is further described in Section 4.2.

1.2 Airborne Instrumentation

The data from various airborne instruments are used – the Solar Spectral Flux Radiometer (SSFR), the Spectral Sunshine Pyranometer (SPN-S), the airborne all-sky camera (ASC), the broadband radiometer system (BBR), an aircraft nadir-viewing camera (NVC), the Spectrometer for Sky-Scanning, Sun-Tracking Atmospheric Research (4STAR), and the High Spectral Resolution Lidar 2 (HSRL-2). I will only introduce the SSFR, SPN-S, and ASC in this subsection as they were key instruments developed in the Atmospheric Imaging, Radiation and Remote Sensing group at the University of Colorado Boulder (CU). The BBR (Section 2.2.1), NVC (Section 2.2.3), 4STAR and HSRL-2 (Section 4.2.2) will be described in the chapters where they occur.

The SSFR is the legacy instrument in the CU AIRS group. SSFR was originally designed and developed at NASA Ames in the early 2000s (Pilewskie et al., 2003). It was originally designed as an airborne instrument with two light collectors – nadir light collector and zenith light collector for simultaneously measuring upwelling and downwelling spectral irradiance range from

350 nm to 2150 nm, but it has also been deployed at multiple ground sites, e.g. at the Skywatch Observatory at CU, to take continuous measurements of solar radiation. SSFR has gone through several important development stages designed specifically for different aircraft field campaigns. For example, an active leveling platform was developed for counteracting the aircraft attitude to keep the zenith light collector look straight up for the ARISE campaign. Details of the instrument specifics will be described in Section 2.2.2 and Section 4.2.1.

The SPN-S and ASC are relatively new. They were developed for the deployment of ORACLES 2018, and also flown during CAMP^{2}Ex 2019. The SPN-S is a modified version of the commercially available global-diffuse SPN1 pyranometer (Wood et al., 2017). Similar to SPN1, SPN-S contains 7 detectors and a fix-mounted shadow mask that can simultaneously measure diffuse and global irradiance. However, SPN-S is a spectral version of SPN1; a prototype that enables the measurements of spectral irradiance from 350 nm to 1000 nm with spectral resolution of 1 nm and temporal resolution of 1 Hz (Norgren et al., 2022). The ASC is a commercially available all-sky camera – ALCOR ALPHEA 6.0CW. It contains fish-eye optics and provides hemispheric imaging through radiances in red, green, and blue channels. Radiometric and geometric calibrations are performed in the airborne radiation science laboratory at LASP before and after each deployment. Details of SPN-S and ASC can be found in Section 3.2.2.4 and Section 3.2.2.5.

1.3 Cloud Retrieval

Spectral albedo can be directly derived from the upwelling and downwelling irradiance measurements of SSFR. From the spectral albedo, cloud optical thickness (COT) and cloud effective radius (CER) can be retrieved through legacy cloud retrieval algorithms. Although not included in any of the three papers in the thesis, extensive efforts have been invested into processing cloud retrievals from SSFR measurements. Legacy cloud retrieval algorithms utilize RT calculations at one non-absorbing wavelength in the shortwave and at one weakly absorbing wavelength in the near-infrared to simultaneously retrieve COT and CER (e.g., Coddington et al., 2010). They use so-called "lookup tables" (LUTs), which are constructed from 1D-RT calculations under various cloud and solar conditions. Figure 1.1 shows an example of LUTs created based on the 1D-RT calculations of albedo at 860 nm and 1630 nm with and without overlying absorbing aerosols for water clouds. With SSFR provided albedo measurements at 860 nm and 1630nm, COT and CER can be estimated from the near-vertical gridding (red/blue solid lines) and near-horizontal gridding (red/blue dashed lines), respectively.

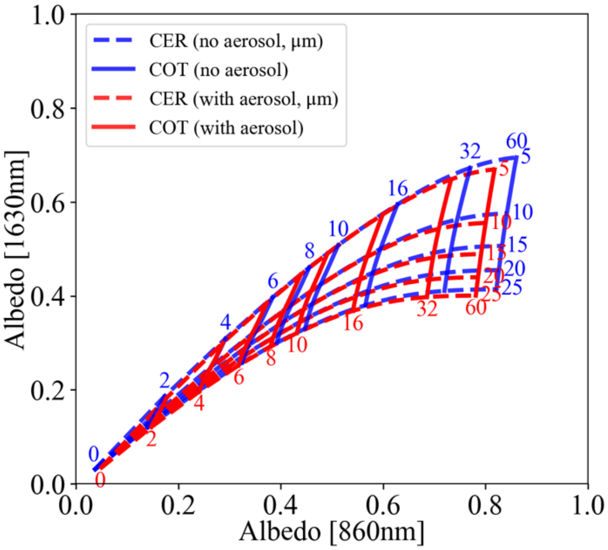

Figure 1.1. Albedo at 860 and 1630 nm at solar zenith angle of 35° with (red) and without aerosol (blue) included in the RT calculations. The solid lines (near-orthogonal) are albedos calculated with the same cloud optical thickness (COT). The dashed lines (near-horizontal) are albedos calculated with the same cloud effective radius (CER).

To evaluate the aerosol effects on satellite imagery derived cloud retrievals, SSFR cloud retrievals were processed for two flight legs collected from a "radiation wall" maneuver from the

P-3 on August 13, 2017 – one flight leg below-aerosol and above-cloud (referred to as BOL) and one flight track above both cloud and aerosol layer (referred to as TOL). As mentioned before, the advantage of aircraft flying at any altitude, here at BOL, is to take measurements of cloud reflectances that are unaffected by the aerosols. The TOL legs, where aircraft measurements of clouds are affected by the aerosols to the same degree as satellite measurements, can be used to emulate satellite retrievals. The BOL and TOL together allow an assessment of the bias in the cloud retrievals stemming from the aerosol layer. Figure 1.2 shows an illustration of COT and CER derived from SSFR measured albedo at 860 nm and 1630 nm for a BOL flight track and a flight track at TOL. The satellite cloud retrievals from MODIS (black) and SEVIRI (cyan and magenta) along the flight track that are closest in time with the aircraft observations were provided. Figure 1.2b indicates that 1) there is good agreement among SSFR COT, MODIS and SEVIRI imagery-derived COT, 2) the satellite imagery-derived COT is systematically low-biased due to the presence of aerosols in between the satellite instrument and the clouds from TOL/BOL intercomparisons. Such cloud retrieval validation, as demonstrated in Figure 1.2, helps in quantifying the aerosols effects on cloud retrievals. However, the cloud retrieval biases associated with other challenging natural environments such as 3D effects from cloud inhomogeneities are not addressed in this manner. All these challenges, prevent us from obtaining an unbiased DARE from satellite observations. Therefore, I pursued a different approach for obtaining DARE that bypasses satellite retrievals and was described previously for the last science question and later in Chapter 4.

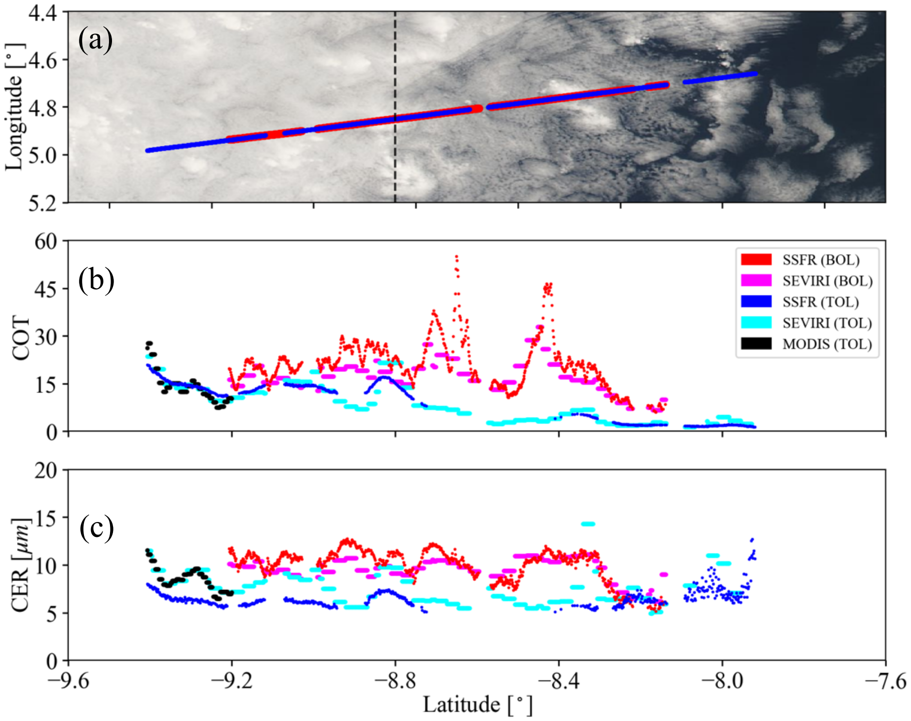

Figure 1.2. **(a)** BOL (red) and TOL (blue) flight tracks overlaid on MODIS RGB imagery from NASA WorldView on August 13, 2017. **(b)** Cloud optical thickness and **(c)** cloud effective radius retrieved from SSFR, MODIS, and SEVIRI along the two flight tracks.

1.4 EaR^{3}T

EaR^{3}T is a modularized Python package that provides high-level interfaces to automate the process of 1D and 3D radiative transfer (RT) calculations for radiative closure studies, radiative energy studies, and machine learning in atmospheric radiation. Specifically, EaR^{3}T can be used to facilitate 1) large-scale systematic radiation closure studies based on satellite remote sensing data products, 2) validation of imagery-derived cloud radiative effects using comprehensive measurement sets from airborne research campaigns, and 3) the training of CNNs with synthetic cloud fields, such as previously mentioned CNN retrieval framework developed by Nataraja et al. (2022). Figure 1.3 shows an illustration of the usage of EaR^{3}T to evaluate 3D aerosol effects in the context of the Radiation Working Group for the development of the NASA A-CCP (Aerosol and Cloud, Convection and Precipitation) study, now known as the AOS (Atmosphere Observing System) mission preparation study. Based on a cloud field from LES, 3D nadir radiance calculations at 532 nm were performed by EaR^{3}T to generate synthetic observations that would be made by a spaceborne radiometer. To evaluate the aerosol effect, the calculations were performed with and without aerosols, as well as with and without 3D-RT effects Visually, the radiance fields are similar, and the aerosol does not show a significant impact on the radiance on a transect along the white dashed line. However, when looking at the radiance histogram in the full domain, discrepancies are found in the shape and location of peaks. Such subtle, but important differences were previously studied mainly in irradiance fields (Schmidt et al., 2009), and are now becoming important for remote sensing, and therefore radiances. However, systematic studies require large quantities of synthetic data. Such data can be generated with other LES cloud fields in an automated way with various different aerosol properties, e.g., absorbing aerosols, scattering aerosols etc. The EaR^{3}T is publicly available at https://github.com/hong-chen/er3t, and is maintained and extended by graduate students at the University of Colorado Boulder. It aims at minimizing the barrier of using 3D-RT calculations and promoting 3D radiation science with anticipation of systematically quantifying and mitigating 3D-RT biases of imagery-derived cloud and aerosol radiative effects in the future.

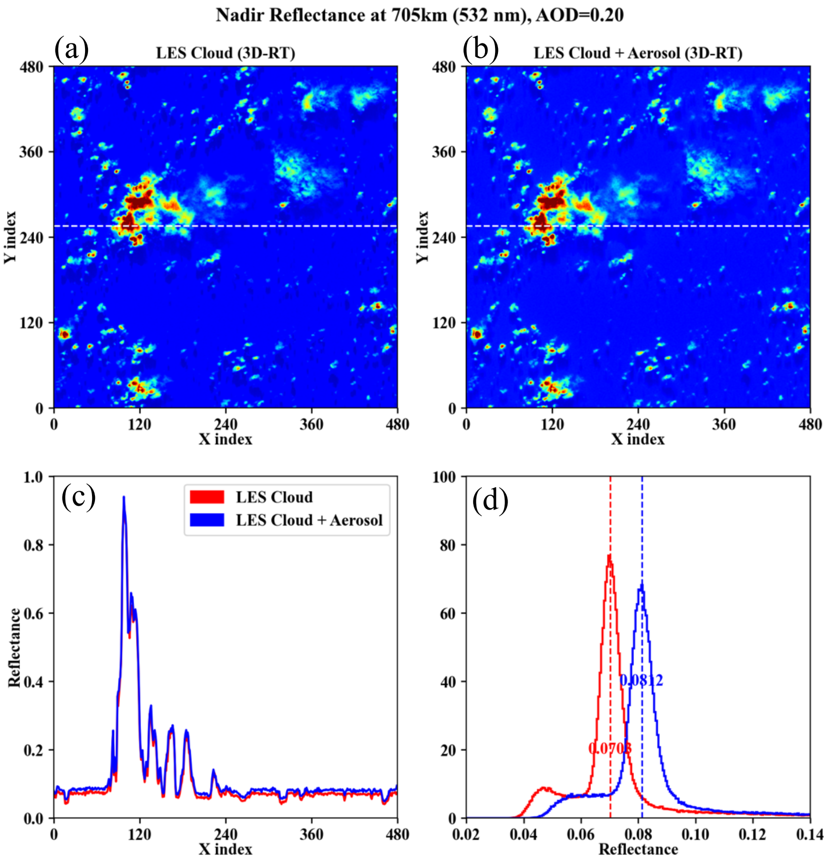

Figure 1.3. 3D reflectance calculations for **(a)** a LES cloud field only, **(b)** the same LES cloud field with overlying aerosol layer at 532 nm. The reflectance along the white dashed line is shown in **(c)** and the histograms for the reflectance calculations are shown in **(d)**.

1.5 CNN COT Retrieval Framework

The CNN COT retrieval framework was developed by Nataraja et al. (2022) and is a new machine learning approach to retrieve COT. It adapts a U-Net architecture and treats the retrieval of COT from radiance as a segmentation problem – probabilities of 36 COT classes range from COT of 0 to 100 are returned as final COT retrieval for a given radiance field of clouds. It accounts for the spatial context of clouds or in other words, horizontal photon transport, which is neglected in traditional cloud retrieval algorithms. It was trained on synthetic cloud fields generated by the Large Eddy Simulation (LES) model, which contains the ground truth of COT. EaR^{3}T was used to produce 3D-RT radiance calculations at 600 nm for the LES cloud fields, which establish a mapping between radiance to COT. Figure 1.4 shows a collection of samples from the training data as an illustration. The training data are in 64x64 tile format with spatial resolution of 100 m. The COT shown on the left panel is obtained directly from the LES dataset by column integrating the cloud extinction coefficients. The right panel shows realistic radiance fields that in nature would correspond to the COT fields, which are 3D radiance calculations at 600 nm produced by EaR^{3}T. Details of the training dataset can be found in Nataraja et al. (2022). The CNN has been tested on LES data different from the training dataset as well as satellite and airborne imageries. Results are generally promising as 3D biases in the traditional IPA retrievals are mitigated to a large degree. More development efforts are currently being invested into building more comprehensive CNNs with the goal of mitigating 3D bias in satellite imagery-derived cloud optical properties. The big challenge for practical applications of machine learning tools for operational retrievals is to establish trust that they represent the underlying physics of a retrieval problem at hand. To achieve this, the radiance self-consistency approach that I developed in the framework of this thesis provides a metric that we explore in Chapter 3. I will show that this self-consistency metric has the potential to lead to a breakthrough for machine learning based passive imagery cloud retrievals.

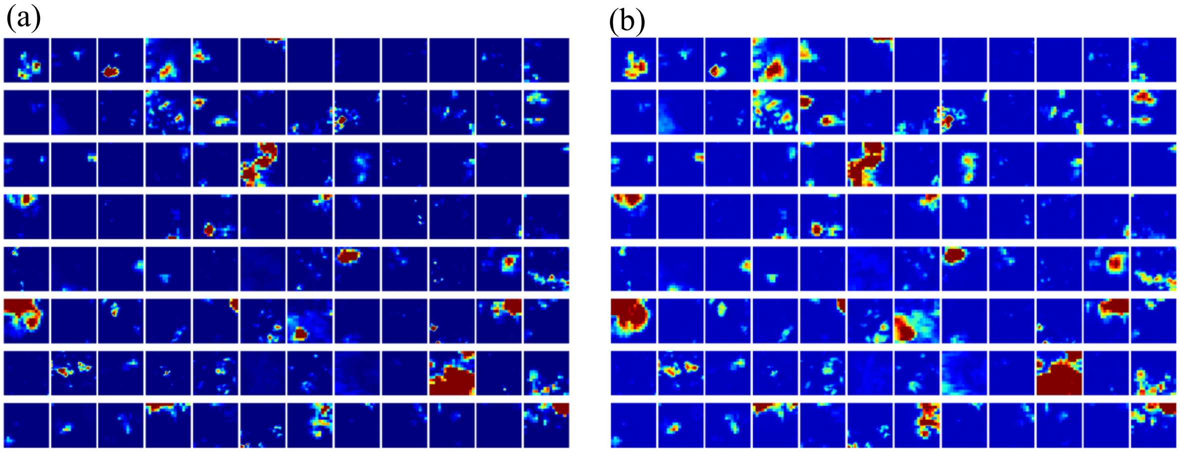

Figure 1.4. Illustrations of 64x64 tiles of (a) cloud optical thickness from LES data and (b) calculated 3D radiance from EaR^{3}T for CNN training.

Chapter 2

The Effect of Low-Level Thin Arctic Clouds on Shortwave Irradiance: Evaluation of Estimates from Spaceborne Passive Imagery with Aircraft Observations

2.1 Background

Understanding the warming of the Arctic necessitates an understanding of the radiative impact of clouds and surface albedo, especially at the surface where the interaction with the cryosphere occurs (Curry et al., 1996; Shupe and Intrieri, 2004). Clouds cool the surface in the shortwave (SW) wavelength range by reflecting solar radiation and warm the surface in the longwave (LW). Low-level, liquid-bearing clouds have recently received special attention because they significantly contributed to the 2012 enhanced Greenland ice melt (Bennartz et al., 2013). When they are optically thin (LWP smaller than 20 gm^{-2}), their SW cooling effect is small because they do not reflect much sunlight, especially when the surface is already bright. In the LW, on the other hand, their emissivity increases rapidly with the liquid water path (LWP), making them blackbodies and warm the surface especially if they are at a low altitude. For larger LWP, the SW cooling eventually dominates as the cloud becomes more reflective.

Valuable data on Arctic clouds has been collected by ground-based observations over the past few decades (Curry et al., 1996, Shupe et al., 2011), but they are limited in spatial coverage and needed to be augmented by additional observations, especially from space-borne remote sensing measurements to help gain meaningful insights of cloud radiative effects in the Arctic as a whole.

Hartmann and Ceppi (2014) used the dataset from the Clouds and the Earth's Radiant Energy System (CERES) and showed that every 10^6 km^2 decrease in September sea ice extent is associated with a 2.5 Wm^{-2} increase in annual-mean absorbed solar radiation averaged over the region from 75º N to 90º N. Kay and L'Ecuyer (2013) used combined products from active and passive remote sensing and showed that during the 2007 summer, the cloud reduction and sea ice loss in the Arctic resulted in more than 20 Wm^{-2} anomalies in shortwave radiation at the top of the atmosphere (TOA). The radiation products used in these studies, e.g., CERES-EBAF (Clouds and Earth's Radiant Energy Systems – Energy Balanced And Filled, Loeb et al., 2012), 2B-FLXHR-LIDAR (Level 2B radiative fluxes and heating rates calculated from radiative transfer model by utilizing radar-lidar cloud and aerosol retrievals from A-Train satellites, Henderson et al., 2013), all rely on coincident cloud observations from the Moderate Resolution Imaging Spectroradiometer (MODIS).

MODIS is a 36-band passive imager onboard the Terra and Aqua satellites. It provides cloud optical parameters (COPs), e.g., cloud optical thickness (COT), cloud effective radius (CER), and cloud thermodynamic phase, from which irradiance can be derived. The COPs from MODIS have been used extensively in studies of cloud radiative effects (e.g., Wielicki et al., 1996; Platnick et al., 2003; Loeb and Manalo-Smith, 2005; Oreopoulos et al., 2016). Due to the lack of temperature and reflectance contrast between clouds and the underlying surface in the Arctic, detecting the clouds is challenging for passive remote sensing, especially when they are thin and occur at a low level. Liu et al. (2010) showed that the MODIS cloud detection algorithm performs better over the ocean than over the ice. The traditional cloud retrieval algorithm (Nakajima and King, 1990) retrieves COT and CER from the reflectance at two channels, one where clouds do not absorb (660, 860, or 1240 nm), and one where cloud drops are weakly absorbing (1630 or 2130 nm). Over snow and ice, the surface albedo is already high in the visible and near-infrared (leaving little dynamic range for cloud remote sensing of optical thickness) and varies regionally and temporally (leading to uncertainties in the retrieval products). This, in combination with low-sun conditions, makes it difficult to obtain accurate cloud optical properties from passive remote sensing. To improve the reliability of MODIS cloud retrievals in the Arctic, an algorithm has been developed that uses two shortwave-infrared bands of 1630 nm and 2130 nm, where snow and ice are relatively dark (Platnick et al., 2001; King et al., 2004). However, the surface albedo varies with surface type even for these bands, and the operational algorithm assumes constant values obtained from a climatology based on 5 years of Terra/MODIS data (Moody et al., 2007).

In addition to the COPs themselves, the snow/ice surface albedo also plays an important role in determining the cloud radiative effect and radiation energy budget in the Arctic (Curry et al., 1995; Shupe and Intrieri, 2004). The surface albedo changes significantly from the visible to the near-infrared wavelength range (Wiscombe and Warren, 1981; Brandt et al., 2005) with different spectral dependence depending on the surface conditions (e.g., snow and ice). Inhomogeneous surface conditions such as floes of partially snow-covered ice, varying snow depth and snow grain size, and surface topography (e.g., sastrugi), all affect the spectral shape and magnitude of the surface albedo. To improve the understanding the inhomogeneous Arctic surface and the spectral dependence of surface albedo, spectral surface albedo measurements for snow and ice have been collected during ground-based field experiments in the polar regions (e.g., Perovich et al., 2002; Brandt et al., 2005). In addition, Perovich et al. (2002) showed that different surface types, e.g., ice, ponds, leads etc., can be identified from aerial camera images through an image processing software. Moreover, a spectral surface albedo model has been developed for different Arctic surfaces such as white sea ice, snow, and melting ponds on sea ice (Malinka et al., 2016 and 2018). However, an operational surface albedo product based on space-borne observations is still not available for the polar regions – in contrast to the land surfaces of the lower latitudes (Strahler et al., 1999).

Finally, accurate knowledge of the water vapor is also important, even in the shortwave (as we will show in this paper). In summary, the challenges for deriving shortwave irradiance from passive remote sensing are (a) inaccurate detection of clouds and cloud optical property retrievals over snow or ice surfaces; (b) lack of accurate surface albedo as a constraint in the radiative transfer model (RTM); (c) insufficient knowledge about the water vapor profile.

The aim of this paper is to use aircraft radiation measurements collected during the NASA Arctic Radiation – IceBridge Sea & Ice Experiment (ARISE, Smith et al., 2017) to evaluate irradiance as derived from coincident satellite imagery, and to investigate the causes of any biases. In the first step, the spectral snow surface albedo was derived from upwelling and downwelling irradiance measurements, accounting for partially snow-covered scenes by the snow fraction estimated from aircraft camera imagery. In the second step, we used an RTM to calculate the upwelling and downwelling broadband and spectral irradiance at flight level, incorporating the MODIS-derived COPs and spectral surface albedo derived from the aircraft measurements as inputs.

The calculated irradiances were then compared with the measured broadband and spectral irradiance pixel by pixel for two cases – above-cloud and below-cloud. Section 2.2 describes the data and method used in this study. Section 2.3 provides the results and discussions for the measured spectral surface albedo, as well as for the comparisons between irradiance calculations and measurements. Conclusions are drawn in Section 2.4.

2.2 Data and Methods

ARISE was a NASA airborne measurement campaign to study snow and ice properties in the Arctic marginal ice zone (MIZ) in conjunction with cloud microphysics and radiation (Smith et al., 2017). The NASA C-130 aircraft was instrumented with shortwave and longwave radiometers, described in this section, along with cloud microphysics probes, aerosol optical properties instruments, and snow and ice remote sensors. The experiment was based at Eielson Air Force Base near Fairbanks, Alaska, from 2 September to 2 October 2014, to capture the September sea ice minimum. In the Arctic, overpasses of polar-orbiting satellites are fairly common. ARISE targeted multiple overpasses of MODIS and CERES on Aqua, Terra, or VIIRS on Suomi NPP on almost every flight. One of the primary objectives of ARISE was to validate irradiance (or flux densities) derived from CERES-MODIS observations with aircraft radiation measurements. Figure 2.1 shows two science flights on 11 September and 13 September that sampled above- and below-cloud conditions, respectively. These flights include so-called “lawnmower” patterns, a series of parallel flight legs laterally offset by about 20 km. They were specifically designed for ARISE to sample one or two 100×100 km^2 grid boxes per flight with a sufficient number of coincident CERES footprints (each with a 20-km diameter at nadir), as to acquire statistically significant above- or below-cloud aircraft measurements for the validation of CERES-MODIS derived irradiance.

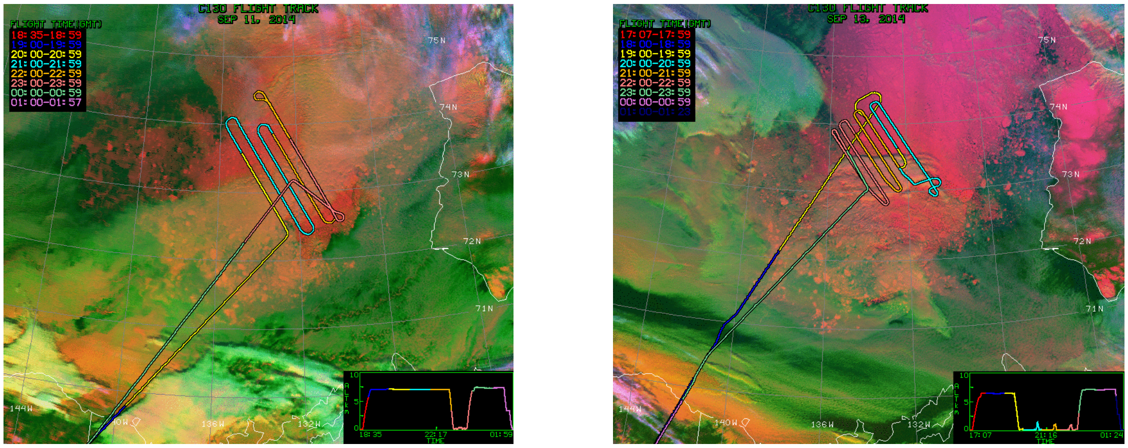

11 September

13 September

Figure 2.1. ARISE flight tracks overlaid on MODIS false color imagery (0.65 μm for red, 11 μm for blue, and 3.7-11 μm for green) from NASA Langley Research Center on 11 September and 13 September 2014. The focus region if these two research flights was [136 ° W, 130 ° W, 72.5 ° N, 74.5 ° N] in the marginal ice zone.

Comparing the aggregated data from ARISE directly with the CERES-MODIS flux products within the grid box, e.g., using histograms, is challenging because of the heterogeneity of the scenes in terms of surface albedo, cloud conditions, and changing solar zenith angle. Therefore, in this paper, we instead compare aircraft observations directly (pixel by pixel) with calculations based on MODIS cloud retrievals along the flight track. The comparison of the aggregated data with CERES-MODIS products is done in a separate publication; we do not use CERES in our analysis because its large footprint does not lend itself to a direct comparison with aircraft data in a heterogeneous environment.

The first step is to merge observations of the broadband shortwave irradiance from the BroadBand Radiometer system (BBR, details in Section 2.2.1) and of the spectral shortwave irradiance from the solar spectral flux radiometer (SSFR, details in Section 2.2.2). This merged product combines the high radiometric accuracy and high-fidelity angular response from BBR with the spectral resolution from SSFR, and is referred to as "SSFR-BBR" data. From these data, the surface albedo is derived for low-level legs under clear-sky conditions. To account for the heterogeneous surface (dark ice mixed with snow-covered ice), the surface albedo is acquired as a function of snow fraction, which is estimated from images of a downward-looking video camera (Section 2.2.3; details on the snow-cover dependent surface albedo derivation in Section 2.3.1). Finally, atmospheric profiles and reanalysis data (Section 2.2.4) along with MODIS cloud products are used to calculate all-sky spectral and broadband irradiances along the flight track (Section 2.2.5), for subsequent comparison with the observations in Sections 2.3.2 and 2.3.3.

2.2.1 BroadBand Radiometer System (BBR)

The BBRs deployed during ARISE are modified CM 22 Precision Pyranometers from Kipp & Zonen (Bucholtz et al., 2010). The BBR included downward-looking and upward-looking sensors. The radiometers were fix-mounted on the aircraft and measured upwelling and downwelling broadband irradiance (unit: W m^{-2}), that is, the spectrally integrated irradiance from 200 nm to 3600 nm. To account for the change of sun-sensor geometry due to aircraft attitude (pitch and roll), a software attitude correction (Long et al., 2010) was applied to the BBR data. In addition, a sunshine pyranometer (SPN-1) was flown to measure diffuse and global radiative fluxes (Badosa et al., 2014; Long et al., 2010). The SPN-1 radiometer was originally intended for ground-based use, but is suited for airborne measurements of global and diffuse radiative fluxes because it does not have any moving parts, unlike traditional instruments such as the Multifilter Rotating Shadowband Radiometer (MFRSR). Smith et al. (2017) provide mission-specific details on both instruments. The BBR has a reported uncertainty of 3% (Smith et al., 2017).

2.2.2 Solar Spectral Flux Radiometer (SSFR)

To attribute discrepancies between satellite-derived irradiance and airborne observations to causes such as erroneous water vapor, cloud properties, or three-dimensional radiative transfer effects, spectrally resolved measurements are needed (Schmidt and Pilewskie, 2012). SSFR is a moderate resolution flux spectrometer built at the Laboratory for Atmospheric and Space Physics (LASP, University of Colorado Boulder). It is an updated version of the heritage spectrometer system originally developed at NASA Ames (Pilewskie et al., 2003). The SSFR radiometer system consists of two spectrometers for each viewing direction (zenith and nadir): 1) a Zeiss grating spectrometer with a Silicon linear photodiode detector array covering a wavelength range from 350 nm to 950 nm and 2) a Zeiss grating spectrometer with an InGaAs linear photodiode detector array covering a wavelength range from 950 nm to 2150 nm. The spectral resolution of the Silicon channels is 6 nm with a sampling of 4 nm. For the InGaAs channels, the spectral resolution is coarser – 12 nm with 6 nm sampling. From the SSFR measurements, spectral albedo, net flux, and absorption can be derived.

SSFR is typically flown in conjunction with an Active Leveling Platform (ALP, also built at LASP), which was developed for counteracting the changing aircraft attitude to keep the zenith light collector horizontally aligned (the nadir light collector was fix mounted). This is particularly important in the Arctic, where low sun elevations lead to large systematic errors for fix-mounted or poorly stabilized sensors (Wendisch et al., 2001). One reason is that radiation from the lower hemisphere (for example, from clouds below or at the aircraft altitude) is registered by the zenith detector when it is tilted, which leads to systematic biases that cannot be corrected. Another reason lies in the specific design of the SSFR light collectors, which are realized as integrating spheres with a circular aperture on top. They diffuse the incoming light collected by the aperture and bundle it into a fiber optics cable that transmits it to the radiometer system inside the aircraft (Schmidt and Pilewskie, 2012). The integrating sphere has an imperfect response to the incidence (polar) angle θ (Kindel, 2010), in contrast to the response of broadband radiometers such as BBR, which are closer to cos(θ) as required for irradiance. At high sun elevations, a so-called hot spot arises from a baffle that prevents light from being directly transmitted into the fiber optics. Since the response deviates significantly from cos(θ), the direct and the diffuse light need to be corrected. This is done by separating the diffuse and direct component, using radiative transfer calculations in conjunction with SPN-1 measurements (details are provided in Appendix 2.A), and further assuming that the downwelling diffuse radiation is close to isotropic. This assumption is an approximation, which becomes invalid if parts of the lower hemisphere are in the light collector's field of view.

The light collector's angular response to the azimuthal angle also needs to be considered. Throughout the course of the mission, the zenith data revealed a dependence on the relative azimuth of the sun to the aircraft. This dependence was characterized at the end of the mission, by two calibration circles flown on 2 October. The non-homogeneous azimuthal response of the zenith light collector occurred for solar zenith angles greater than 66°. Generally, an azimuthally variable response could either be attributed to aircraft interference (e.g., by the tail and/or propellers of the host aircraft), or to the light collector itself. For the former, BBR and SPN-1 (both fix-mounted on the C-130) would also be affected. To assess their azimuthal response, the attitude-corrected BBR data (Bannehr and Schwiesow, 1993; Bucholtz et al., 2008; Long et al., 2010) was compared with the SPN-1 global irradiance data, as well as with radiative transfer calculations. This comparison revealed that in this case, aircraft interferences were minor compared to atmospheric effects (e.g., cirrus), and that only SSFR measurements, but not BBR and SPN-1, had a significant azimuthal dependence, suggesting the SSFR light collector as the source, rather than aircraft interferences. In order to determine the azimuthal dependence, the SSFR measurements were referenced to the BBR measurement[1] during the calibration circle (details in Appendix 2.B). This azimuthal correction function (dependent on the relative azimuth angle of the aircraft and the sun) was then used for the zenith SSFR data for all research flights. After azimuthal correction, the SSFR downwelling irradiance was scaled to BBR using the method described in Appendix 2.D. It is in this sense that the BBR and SSFR measurements are merged. By using BBR, SPN-1, and SSFR in such a way, the redundancies between the instruments were used to capitalize on the strengths of the individual instruments (BBR: un-biased angular response and high radiometric accuracy; SPN-1: diffuse/global separation; SSFR; spectral resolution for sub-range of BBR and SPN-1). The SSFR nadir signal was also referenced to the BBR data in a similar manner (see Appendix 2.D) because BBR has the better angular response, whereas SSFR provides spectral resolution. The details about the merging method and the uncertainties of the merged irradiance product are provided in Appendix 2.D.

The angular dependence of SSFR was verified in the laboratory. In addition, wavelength and radiometric calibrations were performed before and after the mission. The wavelength calibrations ensured spectral accuracy by referencing the SSFR measurements to several line sources. The primary radiometric calibration, performed with a NIST-traceable calibrated lamp, links SSFR measured digital counts to spectral irradiance. The radiometric calibration was also transferred to a so-called secondary radiometric field standard, which monitored the stability of the radiometers throughout the mission.

---

[1] Since BBR has a near-ideal angular response, the attitude correction with respect to the polar angle can be performed by software as long as data are limited to small deviations from level. By contrast, SSFR with its non-ideal angular response requires an active leveling platform.

2.2.3 Imagery from Downward-Looking Video Camera

A downward-looking video camera (referred to as “nadir camera”) is often included as a standard payload on NASA aircraft. It is a standard, commercially available video camera and typically records scenes for context only and is not radiometrically or geometrically calibrated. Despite this shortcoming, the videos recorded by the nadir camera are used for quantitative image analysis. From the video, we first extract image frames with an average rate of 2 Hz (2 frames per second). The extracted image has a pixel resolution of 2592 (width) $\times 1944$ (height). To co-register the aircraft nadir imagery with the measurements from other instruments, the times for the individual image frames are needed, but the image frames themselves did not contain a digitally stored time. They include a timestamp located at the lower left side that contains time information, and we used Optical Character Recognition (OCR) to retrieve the time from this information.

In the second step, the nadir camera imagery was used to quantify the fractional snow coverage. The snow fraction, which is the fraction of bright pixels of the image, was estimated. To this end, the image was converted from RGB (red, green, and blue) into grayscale by

$$Gray = 0.299R + 0.587G + 0.114B \tag{2.1}$$

for each pixel. The weights come from standardized encoding recommendations for television (referred to as BT.601[2]). Another choice would have been to use a single-color channel, or even use the color information to distinguish surface types, but that was not necessary here. For more sophisticated imagery analysis, see Perovich et al. (2002).

One issue of the nadir camera imagery was the darkening effect from the center to the edge of its field of view, which is known as the vignette effect. To compensate, the brightness of the

---

[2] https://www.itu.int/dms_pubrec/itu-r/rec/bt/R-REC-BT.601-7-201103-I!!PDF-E.pdf

image was linearly increased from edge to center through an image blending and interpolation technique by Haeberli and Voorhies (1994):

$$out = (1 - \beta) \times Black + \beta \times Gray \tag{2.2}$$

where $Black$ is a black image with the same dimensions as Gray, and β is the image blending factor, a 2D matrix with increasing values of 1.1-1.5 from the image center to the edge. The operator "×" denotes element-by-element multiplication. To avoid the vignetting extremes in the corners, only the imagery within a concentric sampling area was used to derive snow fraction (left panel of Figure 2.2a). The key step of the snow fraction detection algorithm is the separation of dark versus bright pixels. To do this, an adaptive thresholding technique was applied. It is an approach for handling an image with unevenly distributed intensities by dividing the image into subimages and assigning different thresholds for each of the subimages (Gonzalez et al., 2002). The details of the adaptive thresholding are described in Appendix 2.C. The snow fraction is then estimated by

$$Frac = \frac{N_{bright}}{N_{total}} \tag{2.3}$$

where N_{bright} is the number of pixels above the variable threshold, and N_{total} is the total number of pixels within the sampling area. The imagery and detection results are illustrated in Figure 2.2a, whereas Figure 2.2b shows the simultaneously measured upwelling and downwelling spectral flux. The uncertainties associated with the estimated snow fraction are discussed in Appendix 2.D.

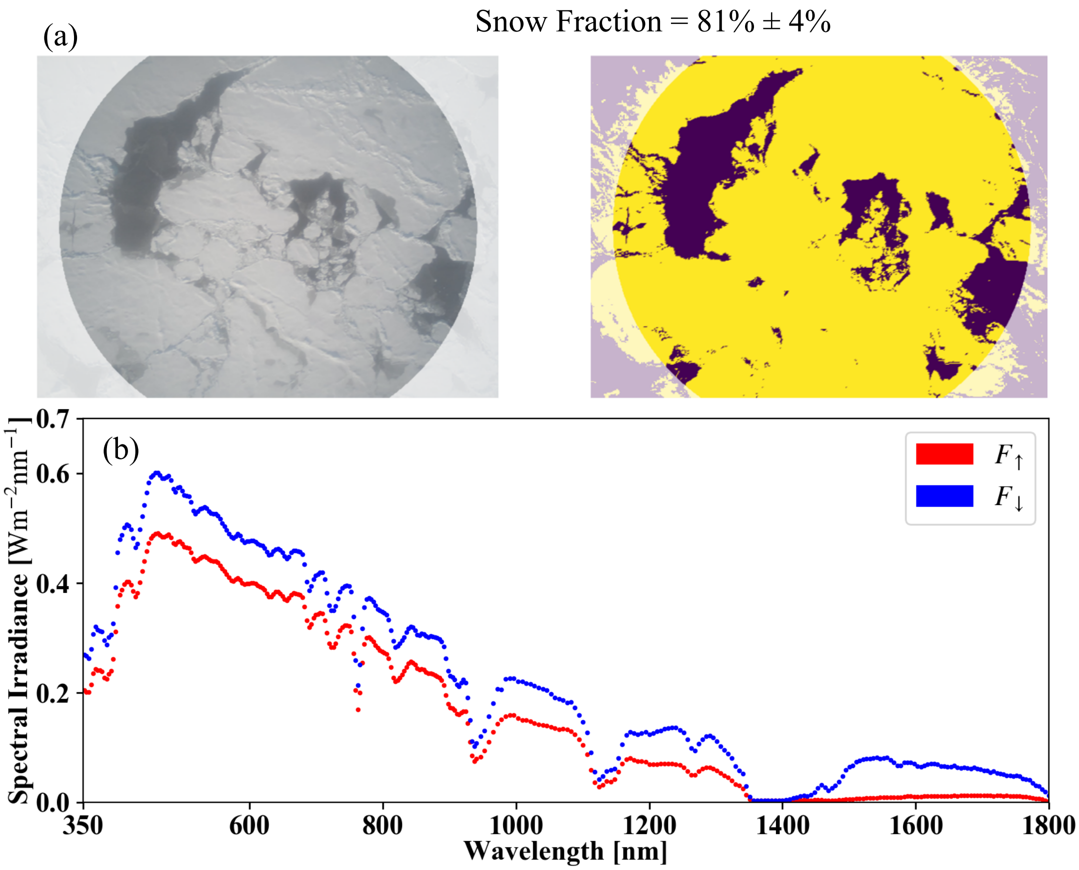

Figure 2.2. **(a)** An example of the snow fraction along with its uncertainty estimated from the nadir camera imagery at 20:03:32 UTC on 13 September, at a location of [132.95ºW, 73.85ºN]. The flight altitude was 134 m. The left panel is the nadir camera imagery. The radius of the field of view was about 380 m. The right panel uses yellow and purple to indicate bright and dark pixels as detected by the adaptive thresholding method. The snow fraction is derived from the abundance of yellow pixels. **(b)** The upwelling and downwelling irradiance from SSFR-BBR at the same time.

2.2.4 C-130 Thermometer and Hygrometer and Modern-Era Retrospective analysis for Research and Applications version 2 (MERRA-2)

The NASA C-130 aircraft was equipped with a thermometer and a hygrometer to measure air temperature and relative humidity, but it did not carry a dropsonde system. Figure 2.2.3b shows the profiles derived from the C-130 during a descending leg from 19:31:14 (altitude: 6.447 km) to 19:50:05 (altitude: 0.258 km) on 13 September, 2014. Due to a malfunction of the hygrometer on

11 September, 2014, no water vapor profile from the C-130 is available on this day. Instead (Figure 2.3a), we used the temperature and water vapor content profiles from MERRA-2, which is an atmospheric reanalysis dataset from NASA (Bosilovich et. al., 2015). MERRA-2 (M2I3NVASM) provides 3-hourly assimilated 3D meteorological fields (dimensions: 576 in longitude; 361 in latitude; 72 pressure levels from 985 hPa to 0.01 hPa). The comparison of the in-situ profiles and MERRA-2 (Figure 2.3b) shows good agreement, although the reanalysis does not reproduce the details of the vertical profile. A more systematic comparison of reanalysis and in-situ data from ARISE is done by Rozenhaimer et al. (2018) and is not the focus of this paper. The observations reveal much drier and slightly colder conditions than captured in the subarctic climatology from Anderson et al. (1986), referred to here as AFGL. Nevertheless, we used the climatology above 6.5 km to provide complete temperature and water vapor profiles from 0 to 120 km, after rescaling them to the observed temperature and water vapor values at 6.5 km. The constructed atmospheric profiles were then used in the RTM (described in the next subsection) to obtain irradiance calculations.

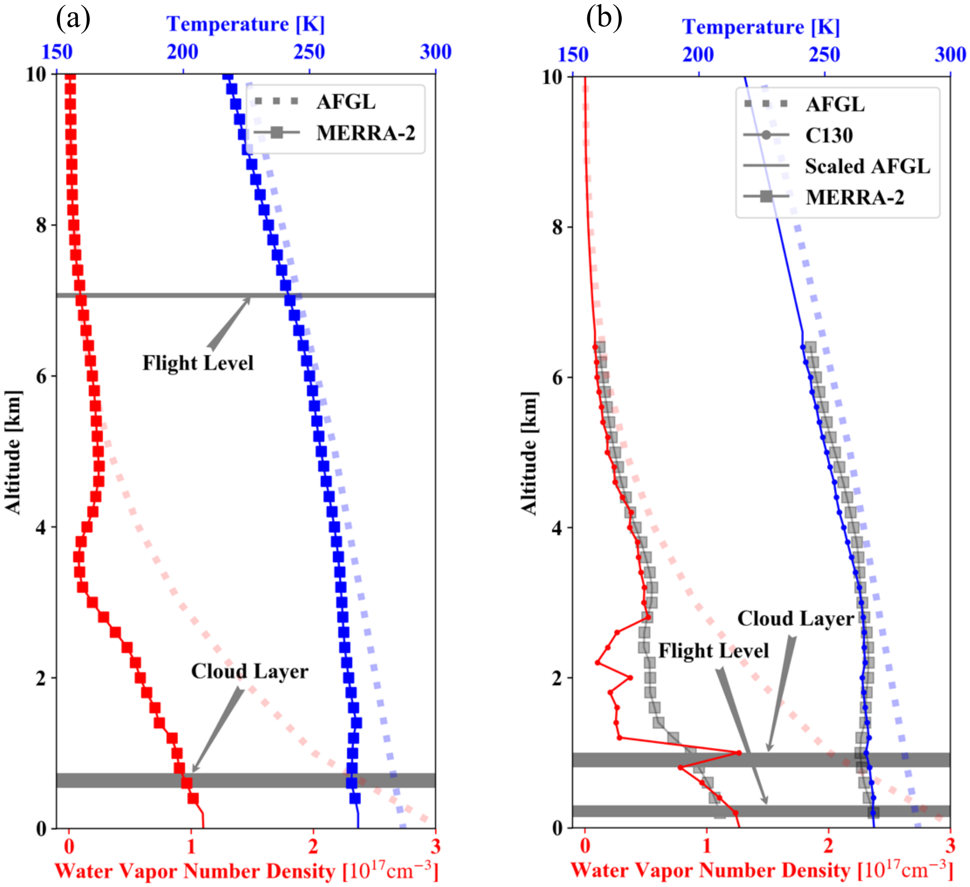

Figure 2.3. Vertical profiles of temperature and water vapor from MERRA-2 and from the climatology (AFGL) for (a) 11 September and (b) from the C130 for 13 September 2014. On 11 September, MERRA-2 data at 21:00 UTC was averaged over the region of [135 º W, 130.625 º W, 72.5 º N, 74 º N] to represent the atmospheric profile there. The vertical cloud distribution was unavailable from the in-situ data. On 13 September, aircraft data from a descending leg (19:31 UTC to 19:50 UTC at 133.8 º W, 74.1 º N) was used for the atmospheric profiles. Based on the water vapor profile, the cloud was likely located below 1.0 km (indicated in grey). Since hygrometer measurements were not available on 11 September, the cloud top height (1.1 km) was obtained from the MODIS L2 product), and the geometric thickness was set to 0.2 km (just like on September 13). The flight level range is also shown. The solid lines for both days represent the temperature and water vapor profiles that went into the radiative transfer calculations.

2.2.5 Radiative Transfer Calculations based on MODIS Cloud Products

The publicly available pixel-level MODIS cloud products (MOD/MYD06, collection 6.1), which are provided in 5-minute granules (Platnick et al., 2017), are used in this study. The MODIS cloud product includes COPs such as COT, CER, and cloud thermodynamic phase, which are essential parameters for calculating cloud radiative effects. As described before, the MODIS COT and CER are retrieved simultaneously using a bi-spectral reflectance method (Nakajima and King, 1990). To minimize the influence of the surface on cloud retrievals, the 1630 nm and 2130 nm bands are used since the snow and ice surface are relatively dark at those two bands (Platnick et al., 2001; King et al., 2004). These retrievals are included in the MOD/MYD06 files and will be referred to as the "1621" cloud product. Limited in-situ observations suggested that the clouds consisted primarily of liquid water, and the MODIS cloud phase product showed less than 2% of ice clouds along the flight track. Therefore, the clouds were assumed to be liquid.

The MODIS "1621" product includes COPs for cloudy and partially cloudy conditions. The latter are denoted as "PCL" in the MODIS data variable name. The product was extracted along the flight track and then input into a radiative transfer model (RTM) to calculate spectral and broadband irradiance at flight level. A 1-D RTM (libRadtran version 2.0.1, Emde et al., 2016) was used for the calculations. It requires the following inputs:

1) Day of the year (for accurate Sun-Earth distance);
2) Atmospheric profile; here, the subarctic summer atmospheric profile from Anderson et al. (1986) along with:
    a) Water vapor content profile from MERRA-2 for 11 September and from the C-130 hygrometer for 13 September, 2014;

    b) Temperature profile from MERRA-2 for 11 September and from the C-130 thermometer for 13 September, 2014;

3) Solar zenith angle;
4) Wavelength;
5) Surface albedo at the specified wavelength (see Section 2.3.1);
6) Slit functions (also known as instrument line shape), which describe the bandpass function of the spectrometer. Here, SSFR slit functions as measured in the laboratory are used (full width at half maximum (FWHM) of 6 nm for the Silicon channels and FWHM of 12 nm for InGaAs channels);
7) Cloud optical thickness, and cloud effective radius; here, from MODIS-COPs;
8) Phase functions; here, from Mie calculations distributed with libRadtran;
9) Output altitude grid; here: only at the aircraft flight level.

The RTM uses a solar spectrum with 1 nm resolution as solar source at TOA (Kurucz, 1992). The Discrete Ordinates Radiative Transfer Program (DISORT, Stamnes et al, 1988) is used as the radiative transfer solver. LOWTRAN 7 (Pierluissi and Peng, 1985) is used for the molecular absorption parameterization. The cloud layer altitude was set to 0.8 km to 1.0 km for 13 September according to the water vapor profile from the aircraft hygrometer. Since the hygrometer data was not available for 11 September and the cloud layer could not be identified from the temperature profile, the mean of cloud top height from MODIS and a cloud geometrical thickness of 0.2 km were used in the calculations. The RTM output includes downwelling (global and direct) and upwelling irradiance at the specified wavelengths and output altitude (in this case, at the flight altitude). The cloud layer location and flight level altitude range were indicated in Figure 2.3. The wavelength range of the calculations is set to 200 to 3600 nm, which encompasses both BBR and SSFR.

2.3 Analysis and Results

This section shows the results for the spectral surface albedo derivation from the irradiance data and the aircraft camera imagery, as well as the comparison of broadband and spectral irradiance between aircraft measurements and radiative transfer calculations. The spectral mixed-scene surface albedo parametrization (described first) is used as input to the RTM calculations in the subsequent comparisons with broadband and spectral irradiance observations. Finally, any biases are attributed to different sources based on their spectral fingerprint.

2.3.1 Spectral Surface Albedo

From the simultaneous measurements of spectral downwelling and upwelling irradiances ($F(\lambda)^{\downarrow}$ and $F(\lambda)^{\uparrow}$), the surface albedo

$$\alpha(\lambda) = \frac{F(\lambda)^{\uparrow}}{F(\lambda)^{\downarrow}} \tag{2.4}$$

can be derived through atmospheric correction (Appendix 2.E) from low near-surface legs under clear-sky conditions. Clear-sky measurements were a rare occurrence because low-level clouds were ubiquitous. In this study, we used clear-sky measurements of SSFR-BBR from 20:00:26 UTC to 20:10:51 UTC on 13 September (referred to as “0913-clear-sky”). A time-synchronized video of the flight is provided as supplementary material (S1 “s1_flight-video_0913-clear-sky.mp4”). This video shows that the Arctic surface varied significantly – from snow scenes to scenes with a large amount of dark ice. Clear-sky scenes (no clouds above or below) were identified from the forward and nadir cameras. During the “0913-clear-sky” case, the aircraft flew at an altitude at around 149 m.

To make full use of the direct measurements of the spectral surface albedo from SSFR-BBR, we parameterized the surface albedo by snow fraction, which can be estimated from the nadir camera imagery (described in Section 2.2.3). The parameterization was done through a data aggregation technique that combines collective measurements in a partially snow-covered environment. Figure 2.2.4 shows the surface albedo at 640 nm, 1240 nm, and 1630 nm plotted versus the snow fraction. The uncertainties of the surface albedo and snow fraction are indicated as vertical and horizontal error bars, respectively (details are provided in Appendix 2.D). The data showed that linear regression can be used to establish a simple relationship between snow fraction and albedo, assuming that each observed spectrum is a mixture of only two so-called end-members: the spectral albedos of a dark and a bright surface. These end-members can vary depending on the local conditions. For example, the dark component can either be open ocean or young ice. The bright component can either be thick ice or a snow-covered surface. The resulting spectral surface albedo for a mixed sampling region is established through the slopes s_λ and intercepts i_λ of the linear fit, with the snow fraction SF ranging from 0 to 1 as the independent variable:

$$\alpha_\lambda = i_\lambda + s_\lambda \, SF \tag{2.5}$$

The linear regression coefficients (i_λ and s_λ) and associated uncertainties were obtained through orthogonal distance regression (Boggs and Rogers, 1990) for all the SSFR wavelengths except for the water absorption bands, and those less than 350 nm or greater than 1800 nm because of a low signal-to-noise ratio. We provided the coefficients as a supplementary material (see S2 "s2_surface-albedo-coefficients.h5"). This simple surface albedo parameterization has obvious drawbacks; for example, the implicit linear-mixing assumption, the variability of the end-members, and data sparsity of the individual end members (in the example in Figure 2.2.4, snow fractions below 0.6 rarely occur).

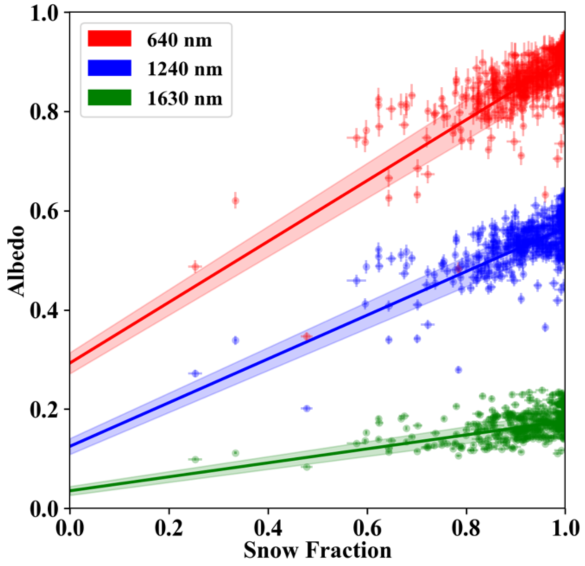

Figure 2.4. Estimated snow fraction from nadir imagery versus SSFR-BBR measured surface albedo at 640 nm, 1240 nm, and 1630 nm. The surface albedo and snow fraction uncertainties are indicated as vertical and horizontal error bars. The solid lines show linear regression fits, and the shaded region indicates their uncertainties.

The snow spectral end-member (snow fraction of 1) of the mixed-scene spectral surface albedo (referred to as “2014-09-13 surface albedo”) is shown in Figure 2.2.5. The error bars of the surface albedo are larger in shortwave than in the near-infrared. As expected, the surface albedo is high in the shortwave range from 400 to 900 nm and decreases in the near-infrared. The SSFR-BBR derived albedo spectra resemble the ground-based measurements of thick snow over ice near Davis Station, Antarctica (Brandt et al., 2005), and they are also close to spring-time aircraft measurements near Barrow (Alaska, Lyapustin et al., 2010). Figure 2.2.5 also shows the surface albedo with zero snow fraction. As pointed out above, snow fractions below 0.6 were extremely rare during “0913-clear-sky”. Nevertheless, the mixed-surface data, extrapolated to 0 snow fraction, compares surprisingly well to ground-based measurements of young gray ice, taken during the Australian National Antarctic Research Expeditions (ANARE) in 1996 (Warren et al., 1997). The spectra shape of the surface albedo at 0 snow fraction (along with the nadir camera imagery from S1) suggests that during the sampled time period, the dark pixels were ice at various freezing states instead of open ocean. As mentioned above, the binary representation of surface types oversimplifies the actual mixture of ice and snow, but is adequate to serve as surface albedo input for the RTM to constrain the irradiance calculations over mixed surfaces, which is our primary goal here.

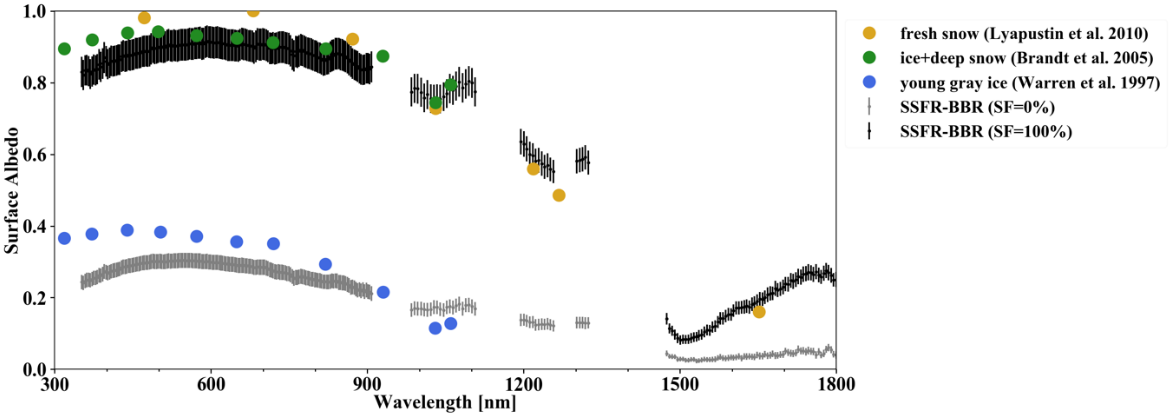

Figure 2.5. Spectral surface albedo derived from SSFR-BBR measurements for *SF*=100% (black) and *SF*=0 (gray), along with their uncertainties. In addition, different albedos from the literature are shown for comparison.

2.3.2 Broadband Irradiance Comparison

In this section, we show broadband irradiance comparisons between SSFR and BBR measurements and MODIS-COPs based RTM calculations at aircraft flight level for an above-cloud case (referred to as "0911-above-cloud") and a below-cloud case (referred to as "0913-below-cloud"), collected by the research flights on 11 September and 13 September, respectively.

The RTM irradiances were calculated for wavelengths from 200 nm to 3600 nm. Since the SSFR-BBR derived surface albedo described in previous subsection was not available at wavelengths shorter than 350 nm, in gas absorption bands, and for wavelengths greater than 1800 nm due to a low signal-to-noise ratio, several techniques were applied to fill in the surface albedo spectra (details in Appendix 2.F). For both the “0911-above-cloud” and “0913-below-cloud” cases, the surface albedo along the flight track was calculated from *SF* as driving parameter to Equation (2.5). The *SF* was determined differently for the two cases. For “0913-below-cloud”, *SF* was obtained from the camera imagery; for “0911-above-cloud”, that was not possible because the surface was not visible through the clouds, and SF was instead set to a constant value of 76.4%, which was obtained by varying *SF* in Equation (2.5) until $\alpha_{1640\ \mathrm{nm}}$ reproduced the observed clear-sky baseline for the upwelling irradiance at 1640 nm. Since *SF* is inferred from the albedo at a single wavelength in this case, it may reflect an “effective”, rather than the actual snow fraction (as obtained from the camera imagery where available), unless the spectral shape of the albedo as acquired for “0913-clear-sky” matches the one of “0911-above-cloud”. This is not necessarily the case. For example, changes in snow grain size between the two cases would disproportionately affect 1640nm. It should also be noted that the observed albedo is the blue-sky albedo (direct beam and diffuse light conditions), whereas the albedo required for the cloud cases is the white-sky albedo (diffuse light only). However, MODIS-derived surface albedo in the Arctic (not shown here) shows that usually the blue-sky albedo of snow does not deviate significantly from the white-sky albedo. The difference between the two is discussed by Gardner and Sharp (2010). In addition, it is assumed that the simple parameterization as expressed in Equation (2.5) holds for the whole study region. This is justified because the measurements occurred in the same general area. Figure 2.2.6 shows the surface albedo calculated for *SF*=76.4% for “0911-above-cloud”. Comparing with dry- and wet-season surface albedo climatology from Kay and L’Ecuyer (2013), the wet-season climatology agrees well with SSFR-BBR derived surface albedo in the shortwave (wavelength less than 900 nm) except for wavelength 660 nm, where climatology has a higher surface albedo. In the shortwave near-infrared (wavelength greater than 900 nm) however, the dry-season climatology agrees better with SSFR-BBR derived albedo than wet-season. It is worth noting that the surface albedo assumed in MODIS 1621 cloud retrievals (Platnick et al., 2018) agrees with the surface albedo we obtained from SSFR-BBR.

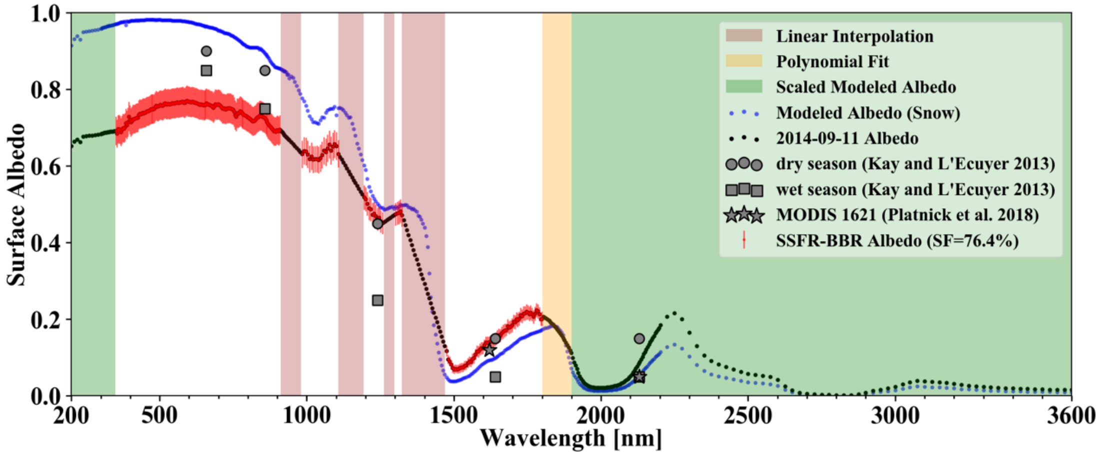

Figure 2.6. Spectral surface albedo (black) along with their uncertainties used in the RTM for the 2014-09-11 calculations. The spectral albedo uses the SSFR-BBR derived albedo with *SF*=76.4% (red) except for the wavelength ranges marked (1) in green: replaced by scaled modeled snow albedo (blue); (2) in red (gas absorption bands): linear interpolation; and (3) in yellow (1800nm to 1900nm): polynomial fit using SSFR-BBR derived albedo from 1650nm to 1800nm.

Figure 2.2.7 shows the broadband irradiances from SSFR-BBR, BBR, and the calculations (Figure 2.2.7a: downwelling; Figure 2.2.7b: upwelling) for the “0911-above-cloud”, where the aircraft was flying at an altitude around 7 km. The observed variability in the downwelling signal is due to the occurrence of cirrus above the aircraft, which is confirmed by the forward camera (Figure 2.7 1-3). In Figure 2.7a, cirrus-free regions are highlighted in green.

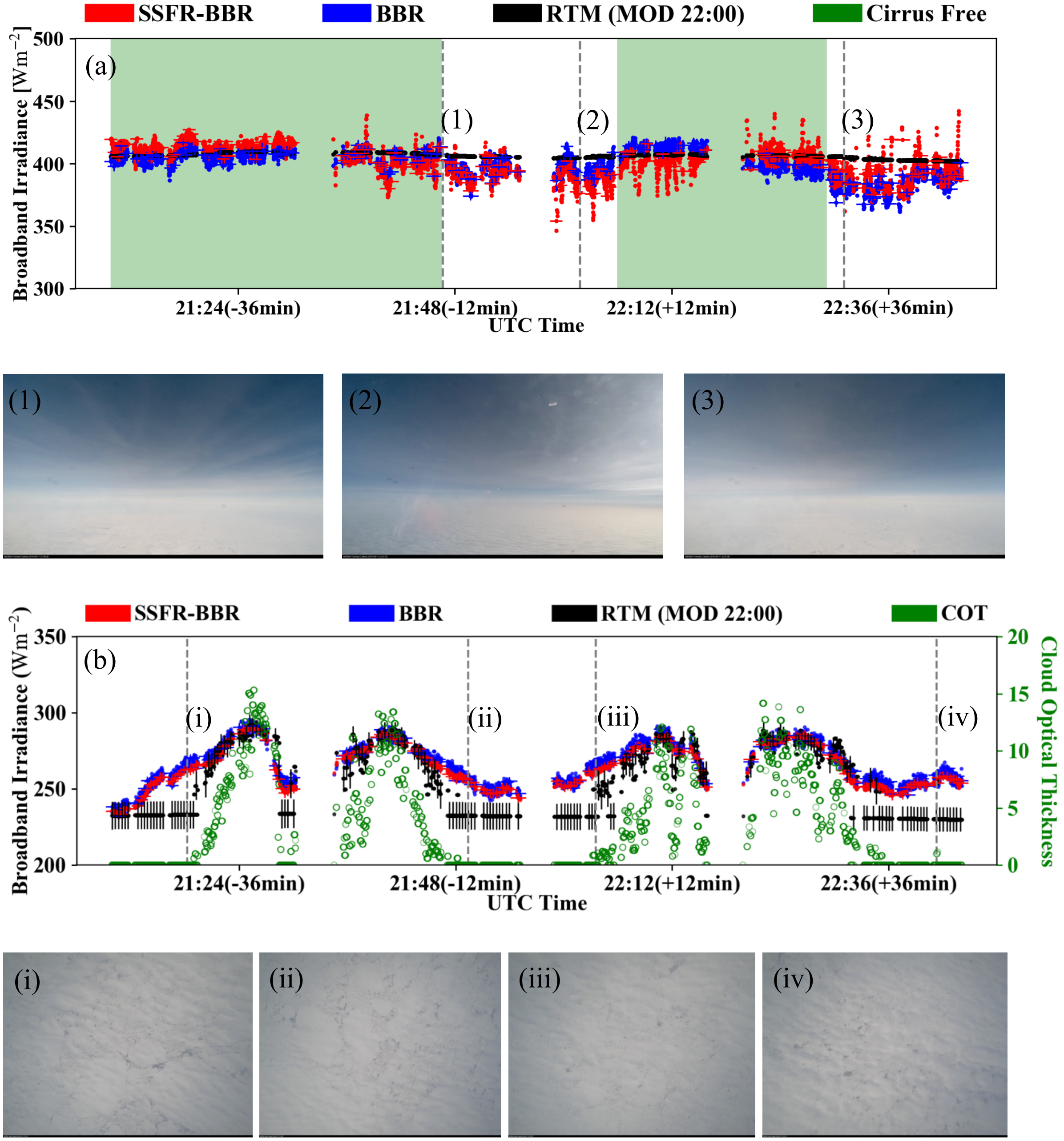

Figure 2.7. Broadband **(a)** downwelling and **(b)** upwelling irradiance from SSFR-BBR, BBR, and MODIS-COPs (Terra MODIS at 22:00) based RTM calculations on 11 September (above-clouds) along with their uncertainties (c) and (d) the histograms. The observed irradiances include a horizontal error bar (indicating the size of the SSFR-BBR FOV) in addition to the vertical error bar (indicating the uncertainty of SSFR-BBR irradiance). The cloud optical thickness from MODIS is indicated in green. The average cloud optical thickness is 6.03. The forward camera images are provided at **(1)** 21:46:39, **(2)** 22:01:53, and **(3)** 22:31:05. The nadir camera images are provided at **(i)** 21:18:15, **(ii)** 21:49:22, **(iii)** 22:03:28, and **(iv)** 22:41:18 UTC. The time differences between aircraft measurements and MODIS granule are indicated in the axis labels. The average flight altitude was 7 km and the average aircraft ground speed was 150 m/s.

It shows that the cirrus decreases the measured downwelling irradiance by up to 10% (40 Wm^{-2}). However, there is no appreciable cirrus cover in the regions where low-level clouds are present. Since those are the focus of the manuscript, cirrus were not considered in the RTM. For the upwelling irradiance, the MODIS-derived baseline value of 230 Wm^{-2} corresponds to locations where MODIS did not detect any clouds. It is important to note that the value of the baseline indicates the RTM calculations under clear-sky condition, which would change if a different surface albedo parameterization or a different snow fraction were used. For a SF=76.4%, the calculations agree with the measurements within 10%. The cloud optical thickness along the flight track (included in Figure 2.2.7b) ranges from 0.5 to 15.3, with a median of 5.7, suggesting that MODIS does not retrieve clouds with an optical thickness below 0.5. In contrast to the calculations, the measurements show a continuous variation from leg to leg, suggesting that the clouds actually extended beyond the locations where MODIS detected them. Since the SSFR/BBR sensors integrate the cosine-weighted radiances hemispherically, they do not the same field of view (FOV) as MODIS pixels. The clouds detected by SSFR/BBR but not by MODIS could therefore be caused by clouds located outside the FOV of MODIS. To take this into account, we assume a 90° (±45°) FOV for the SSFR/BBR that encompasses roughly half of the irradiance signal for an isotropic radiance distribution. When the aircraft was flying at 7 km, the FOV diameter of SSFR/BBR is 14 km (indicated as horizontal bars in Figure 2.7b, translated into a time range using the aircraft speed). This is larger than the 1 km MODIS pixel-level product FOV. However, the results indicate that cloud portion missed by MODIS exceeds the FOV of the aircraft radiometer and therefore cannot be explained by the mismatch in the observational geometry. To further corroborate that the MODIS algorithm is indeed missing clouds, a sequence of nadir camera imagery (Figure 2.2.7b i-

iv) is considered. At close inspection, the images reveal wave patterns, suggesting the existence of thin clouds in regions where MODIS does not detect any. In this case, undetected, optically thin clouds made up more than one fifth of the points along the flight track. Figure 2.2.7b indicates that these undetected clouds lead to an underestimation of the upwelling irradiance by 30 Wm^{-2} averaged over these pixels (>10% discrepancy). Figure 2.8 shows the histograms of the (a) downwelling and (b) upwelling irradiance of the cirrus free data (marked in green in Figure 2.7a). Without including the data affected by the cirrus, the downwelling irradiances from RTM agree with observations within measurement uncertainty. The upwelling irradiances from the RTM show two distinct modes. The mode on the left corresponds to clear-sky, and the mode on the right to a range of somewhat higher reflected irradiance due to those clouds that are detected by MODIS. From the clear-sky mode (black dashed line on the left at 233 Wm^{-2}) to the thinnest detectable cloud (green line at 246 Wm^{-2}), there is a gap, which, according to the measurements, is actually filled with a continuum of values from thinner clouds and/or from a variable surface albedo. Because of this gap, the low bias due to undetected clouds is smaller than or equal to 13 Wm^{-2}. Whereas this bias caused by undetected clouds in the upwelling irradiance is almost negligible, it becomes significant for the transmitted irradiance (see below). The calculated irradiances for the locations where MODIS does detect clouds are only 10 Wm^{-2} lower than the measurements (4%), which is only slightly larger than the BBR/SSFR measurement uncertainty (3%, see Appendix 2.D) and can be explained either by (a) incorrect COPs (optical thickness, effective radius, or thermodynamic phase) and/or (b) inaccurate or variable surface albedo. To quantify the contributions of these effects to the total discrepancy, the spectral information from SSFR is used in Section 2.3.3.

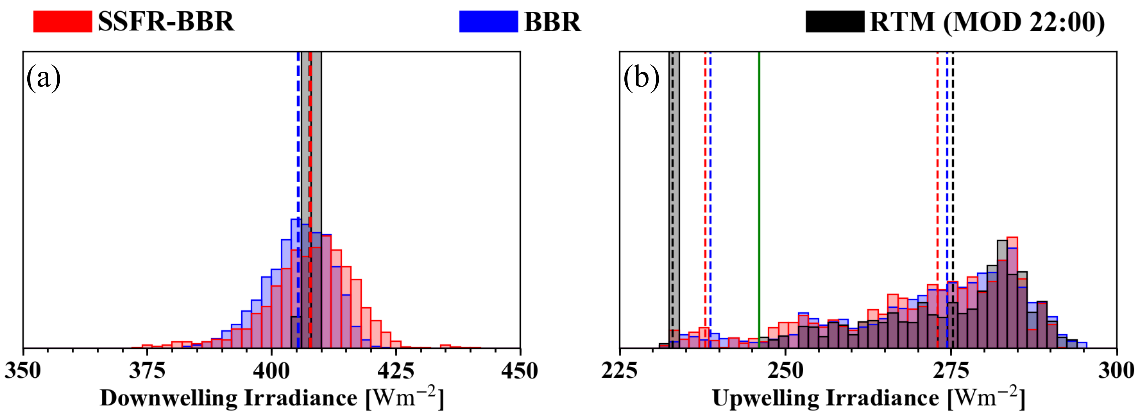

Figure 2.8. Histograms of broadband **(a)** downwelling and **(b)** upwelling irradiance from SSFR-BBR (red), BBR (blue), and MODIS-COPs (black, Terra MODIS at 22:00) based RTM calculations on 11 September (above-clouds). Only "cirrus free" data (marked in green in Figure 2.7 (a)) is included. For (a), the mean values of BBR, SSFR-BBR, and RTM calculations are indicated by the colored dashed lines. For (b), the mean is calculated for each of the two modes separated by the green line and indicated by the colored dashed lines.

After the investigation of the above-cloud case for MODIS-derived irradiance, we turn our attention to the below-cloud case – "0913-below-cloud", which relates to near-surface irradiance. The primary cloud layer consisted of stratocumulus cloud and was located between 0.8 and 1.2 km. The cloud optical thickness (indicated in Figure 2.9a) ranges from 4.1 to 8.1, with a median of 5.8. A secondary cloud layer close to the surface, located below the aircraft's minimum flight altitude of 500 ft (approximately 150 m), frequently occurs due to a temperature inversion close to the surface, where leads and cracks in the ice provide the necessary moisture for their formation. These clouds also need to be considered to quantify the radiative surface budget, but they are excluded from the analysis here because the aircraft could not underfly them. As a result, only the data from 22:21:00 to 22:25:48 (minimal occurrence of the secondary cloud layer as indicated by the forward and nadir camera imagery) was selected for comparison. A time-synced video for this flight leg is provided in the supplementary materials (see S3 "s3_flight-video_0913-below-cloud.mp4"). As mentioned before, in contrast to the above-cloud case where the surface albedo was held constant in the RTM, the surface albedo variability on the below-cloud leg was considered here. Figure 2.9 shows the upwelling and downwelling broadband irradiance comparison between calculations and observations from SSFR-BBR and BBR. When incorporating the “13 September surface albedo” into the RTM, the upwelling irradiance calculations resemble the SSFR-BBR and BBR measurements (Figure 2.9b). The calculations agreed well with SSFR-BBR and BBR when clouds were detected except for the time period before 22:22:48 UTC when the aircraft was entering the cloud field. The MODIS granule from Aqua was a snapshot of the cloud scene at 22:10, 10 minutes prior to the beginning of the flight leg. Measurement-model discrepancies for specific pixels can therefore be explained by changes of the cloud field over time.

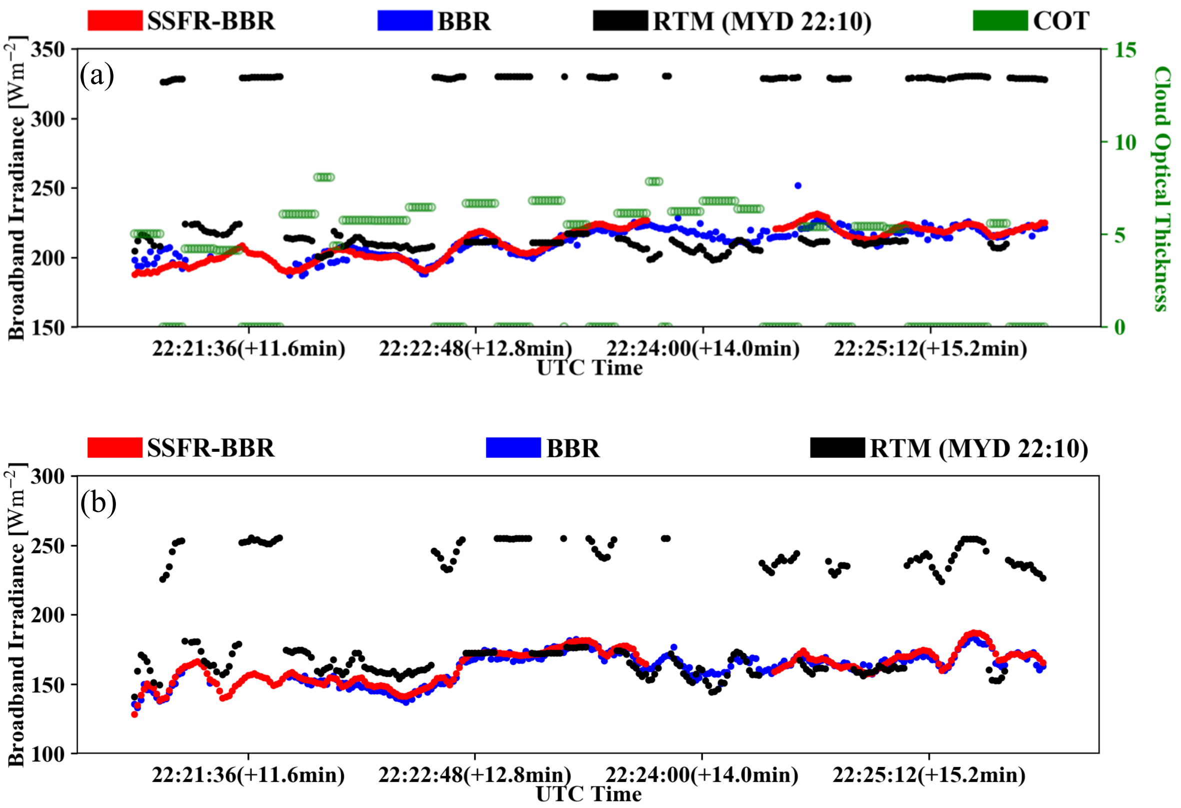

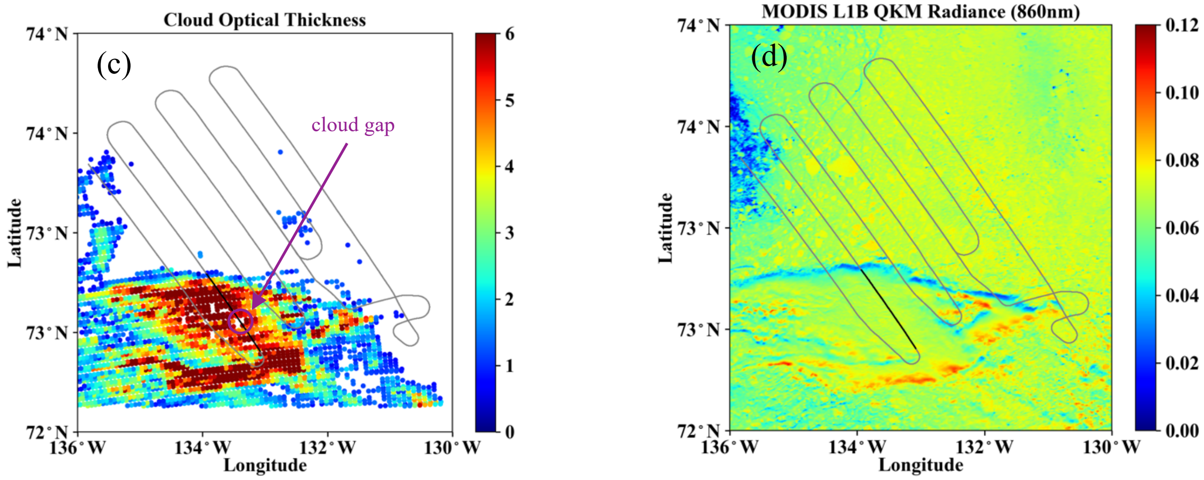

Figure 2.9. Broadband **(a)** downwelling and **(b)** upwelling irradiance from SSFR-BBR, BBR, and MODIS-COPs (Aqua MODIS at 22:10) based RTM calculations on 13 September (below-clouds). The time difference between aircraft measurements and MODIS granule is indicated in the axis labels. In addition, the field of cloud optical thickness and radiance at 860 nm from MODIS are provided in **(c)** and **(d)**. On the map, the black line indicates the flight track studied in (a) and (b). The average flight altitude was 235 m, and the average aircraft ground speed was 106 m/s.

The bimodal behavior that is apparent in the time series (Figure 2.9a and 2.9b) as well as in the histograms (Figure 2.10) stems from time periods with and without clouds in the model input. The observations show no evidence of any cloud gap – hence only one mode appears. The "cloud gaps" apparent in the satellite but not aircraft measurements could be caused by different viewing and sun-sensor geometries between the satellite and aircraft instruments. For example, tall clouds could block the direct sun beam measured by the aircraft radiometer when flying below clouds under low-sun conditions. By evaluating the fields of cloud optical thickness and radiance at 860 nm from MODIS (Figures 2.9c and 2.9d) and the supplementary flight video S3, we found that any cloud gaps are not large or frequent enough permit the direct beam to be transmitted. This leads to a smooth irradiance time series in the aircraft measurements. The gaps (circled in Figure 2.9c, most likely at sub-grid scale for the 1 km product), however infrequent, do occur in the satellite retrievals. From the histograms of Figure 2.10, one can estimate the pixel-level bias caused by undetected clouds. In this case, the thinnest detectable clouds are associated with 234 Wm^{-2} in the calculations, as opposed to the clear-sky value of 330 Wm^{-2} (bias of 86 Wm^{-2}). For the upwelling irradiance, the bias is 57 (245-188) Wm^{-2}, and the net irradiance high bias due to undetected clouds is therefore 29 W m^{-2}.

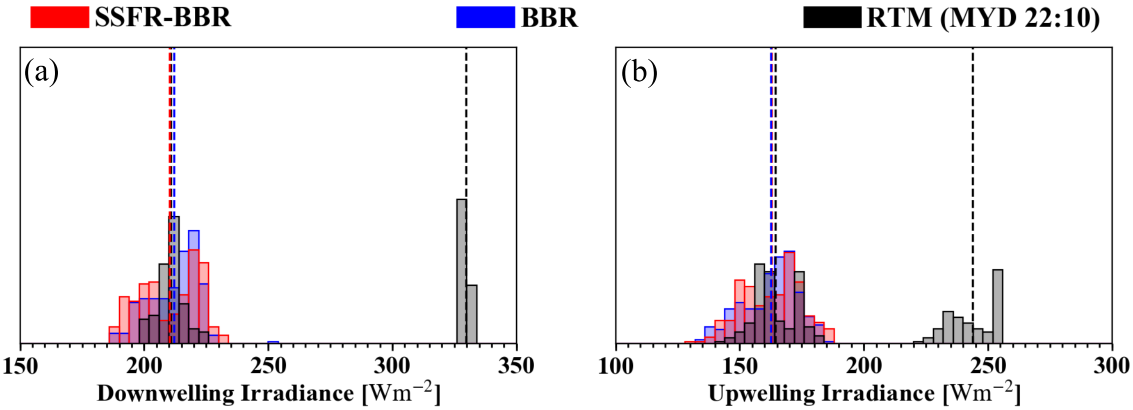

Figure 2.10. Histograms of broadband **(a)** downwelling and **(b)** upwelling irradiance from SSFR-BBR (red), BBR (blue), and MODIS-COPs (black, Aqua MODIS at 22:10) based RTM calculations on 13 September (below-clouds). The mean value of the SSFR-BBR and BBR data is calculated and indicated by red and blue dashed lines. For the RTM calculations, the mean value is calculated for each of the two modes separated by the green solid line and indicated by the black dashed lines.

2.3.3 Spectral Irradiance Comparison

Although the model-measurement biases in the broadband irradiances are negligible when clouds were detected, the time series as shown in Figure 2.2.7b do not quite match, especially for the thin parts of the clouds near the edge of a field. To diagnose the cause, we use the spectrally resolved measurements by SSFR-BBR in this section.

For “0911-above-cloud”, Figure 2.11 presents the spectral upwelling irradiance comparison at 860nm and 1640nm. To put these results into context, the RTM calculations were not only performed with a surface albedo from Equation (2.5) (with *SF*=76.4%), but also with climatological surface albedos of the Arctic dry and wet seasons (0.85 and 0.75) for 860nm from Kay and L'Ecuyer (2013). As shown in Figure 2.11a, the baseline of the clear-sky RTM calculations varied significantly with surface albedo. The clear-sky measurements from 21:12:25-21:15:35 UTC are slightly below the *SF*=76.4% baseline calculation for 860 nm, and above for other times. It is impossible to tell whether the variability at this wavelength stems from surface albedo variability or from undetected clouds. For 1640 nm (Figure 2.11b), however, the clear-sky baseline is much more defined and less variable than other wavelengths, which is why we determined the *SF* value based on that wavelength.

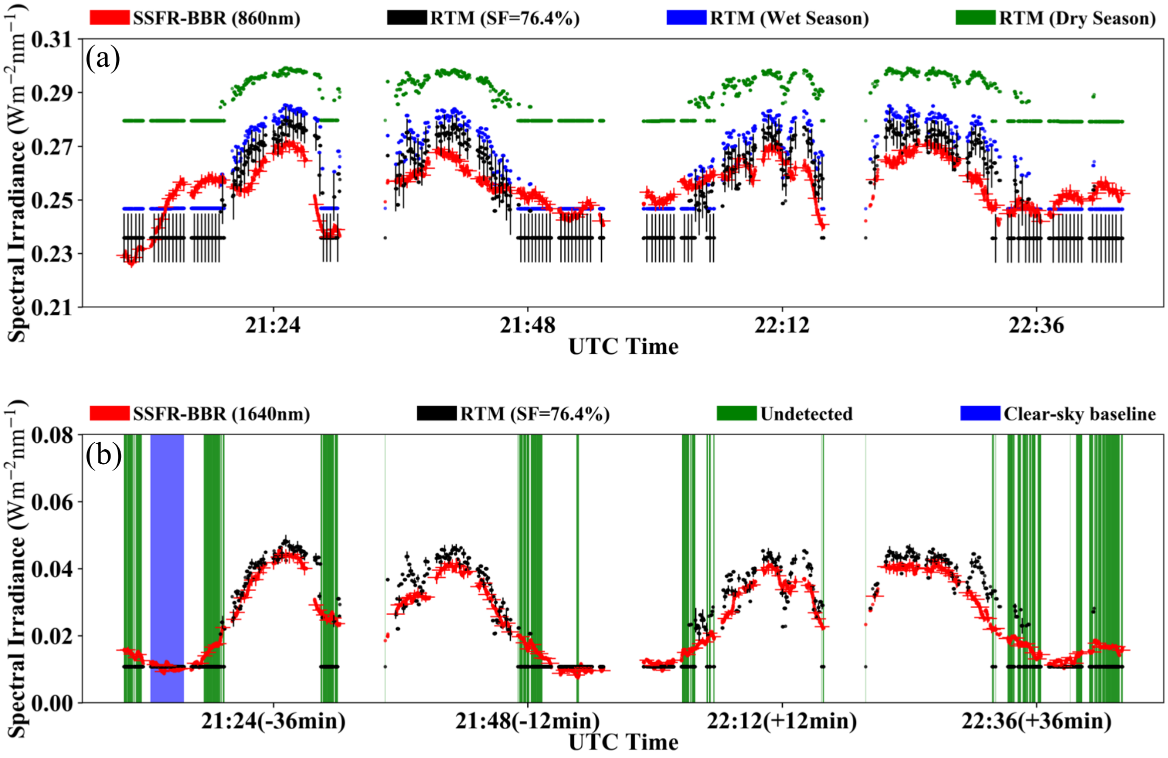

Figure 2.11. Spectral upwelling irradiance at 860nm (panel **a**) and 1640nm (panel **b**) from SSFR-BBR (red) and MODIS-COPs based RTM calculations using "13 September surface albedo" with *SF*=76.4% (black) on 11 September. In addition, calculations with climatological snow albedos are shown in panel (a) (Arctic wet season: 0.75; Arctic dry season: 0.85). The time periods where clouds were not detected are marked in green

in panel (b). The clear-sky period that was used to determine the snow fraction is highlighted in blue in panel (b). The uncertainties of the spectral irradiances are indicated as vertical error bars, and the horizontal error bars correspond to the radiometer FOV as in Figure 2.7. Both need to be considered to identify undetected clouds.

Since any inaccuracies in the spectral surface albedo will propagate into model biases for both cloudy and clear-sky conditions, an operational surface albedo retrieval in the Arctic would be highly desirable. In this context, it is important to note that the small broadband model-measurement discrepancy of 8 Wm^{-2} from Figure 2.7 is only achieved when the SSFR-BBR derived surface albedo is used in the RTM calculations; when using a climatology instead, it would be larger. In other words, in absence of an operational product, the surface albedo variability dominates the uncertainty in clear- and cloudy sky irradiance calculations.

At 1640 nm (Figure 2.11b), there is good model-measurement agreement for the clear-sky baseline and for cloudy pixels that MODIS detects. That is because snow is dark in the shortwave infrared, and because MODIS COPs in the Arctic are primarily based on these wavelengths. Because of the obvious distinction between cloudy and clear pixels in the measurements and calculations, it is possible to estimate the fraction of partially or fully cloudy pixels that are not detected by MODIS. Among all the cloudy pixels along the flight leg (i.e., pixels with clouds above or below the MODIS detection threshold), 27% (highlighted in green) are actually cloudy even though MODIS identifies them as clear sky. One interesting finding from the broadband irradiance comparison (Figure 2.7b) is that the calculations are low-biased relative to the observations. However, from the spectral comparison (Figure 2.11), the calculations have larger/similar values than the SSFR measurements at 860 nm/1640 nm. To reconcile the apparently contradictory results, we use the full spectrum from the calculations and observations at 21:24 UTC on 11 September, when the broadband calculation indicates a 6 Wm^{-2} low bias.

Figures 2.12a and 2.12b show the spectral upwelling irradiance from the RTM calculations and from the SSFR-BBR measurements, as well as the difference between RTM and SSFR-BBR. In addition to the RTM calculations with atmospheric profiles from MERRA-2 (referred to as RTM_{MERRA}), we provided the calculations with the atmospheric profile climatology (AFGL subarctic summer, Anderson et al., 1986, referred to as RTM_{AFGL}). The agreement between RTM_{MERRA} and SSFR-BBR in the water vapor absorption bands indicates that MERRA-2 is sufficient to prescribe the water vapor content in the calculations. The broadband irradiance difference between RTM_{MERRA} and RTM_{AFGL} due to water vapor is 13.5 Wm^{-2}. Outside of the gas absorption bands, the calculations agree with the measurements at wavelengths smaller than around 850nm, but are slightly low-biased at near-infrared wavelengths. Spectral discrepancies are caused by the use of inaccurate 1) surface albedo 2) cloud optical parameters, some of which compensate each other in the broadband integral. Such error compensation may lead to an improved model-measurements agreement for the "wrong reasons"; therefore, validation efforts should include spectrally resolved measurements.

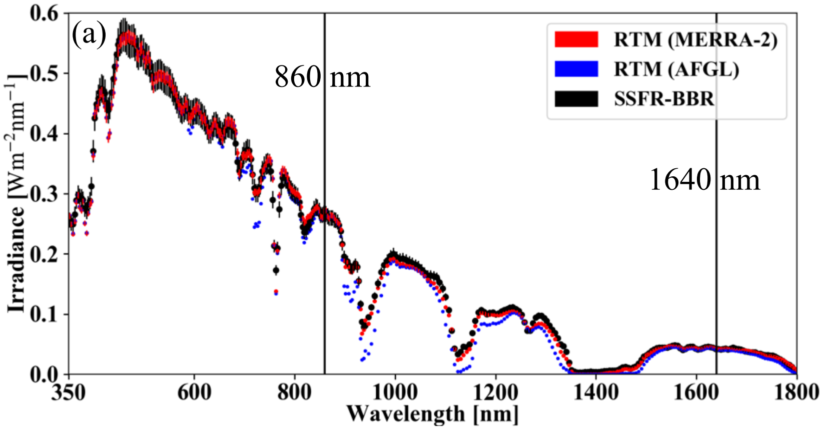

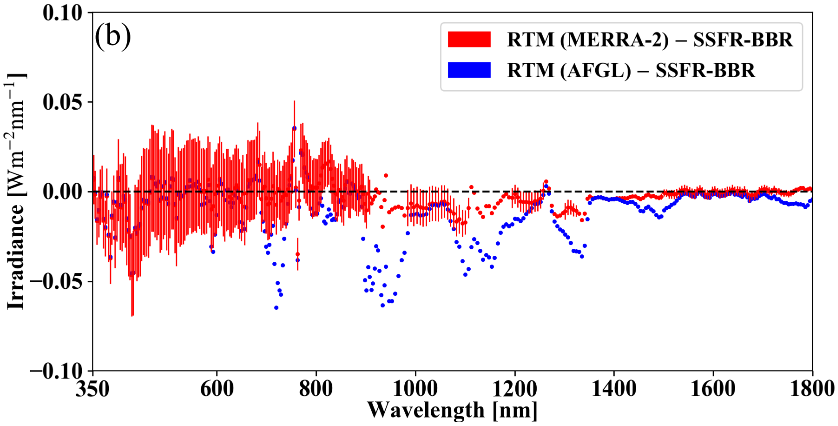

Figure 2.12. **(a)** Spectral upwelling irradiance from SSFR-BBR (black) and MODIS-COPs based RTM calculations with atmospheric profiles from MERRA-2 (red) and with AFGL subarctic summer climatology (blue) at 21:24 UTC on 11 September. **(b)** Irradiance difference between RTM and SSFR-BBR. The uncertainty of the SSFR-BBR irradiance is indicated as error bars (for one spectrum only).

So far, the analysis did not reveal whether the observed model-measurement discrepancies are due to biases in the COPs or in the surface albedo. Figures 2. **2.1**3-2.2.14 are an attempt to disentangle both sources of uncertainty despite the limited number of observations during ARISE. Figure 2. **2.1**3 shows the ratio between modeled (labeled "RTM") and measured ("SSFR-BBR") upwelling broadband irradiance at flight-level as a function of the retrieved COT for the collection of cloudy pixels from 11 September. At large COT, clouds dominate the upwelling irradiance, whereas the surface dominates in the limit of zero COT (as stated above, the retrieved minimum is 0.5). The ratio of RTM/SSFR-BBR can be used to indicate how biased the surface albedo is in the RTM when COT is approaching to 0 and how biased the cloud optical properties are when the COT approaches large values. The data reveal a functional relationship between COT and the RTM/SSFR-BBR ratio.

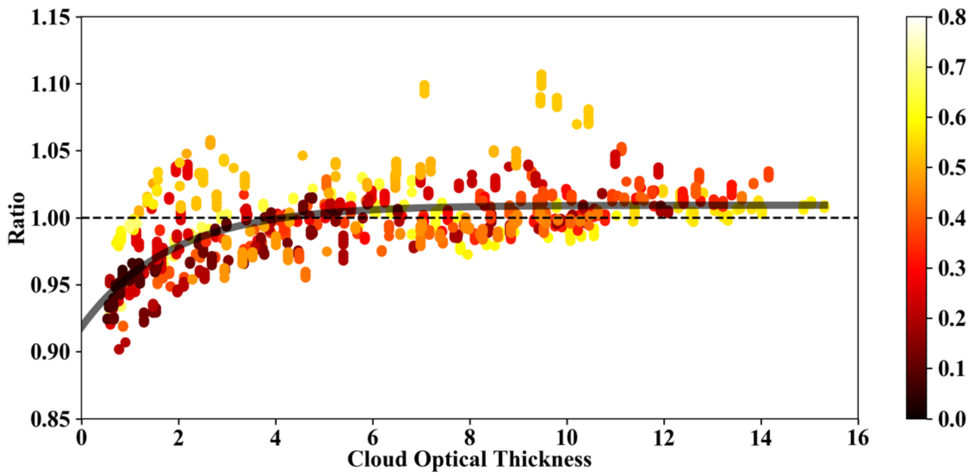

Figure 2.13. Ratio (RTM/SSFR-BBR) of upwelling broadband irradiance as a function of cloud optical thickness from MODIS "1621" cloud product on 11 September. The time differences between aircraft measurements and MODIS granule (unit: hour) is color-coded. The black curve is an exponentially fitted line using $r = a - e^{b \cdot COT + c}$, where $a = 1.0093$, $b = -0.5464$, and $c = -2.3954$.

An exponential fitting of

$$r = a - e^{b \cdot COT + c} \tag{2.6}$$

is used to parameterize the upwelling irradiance ratio as a function of COT. The black curve in Figure 2. **2.1**3 suggests that the surface albedo in the calculations is biased low by about 8%, whereas almost no bias is detectable in the cloud properties (a of ~1.01). Figure 2.2.14 shows the spectral fits for the wavelengths between 350 and 1800nm. Two spectra are calculated: the spectrum of the ratio when $COT = 0$ (denoted as $r_0(\lambda)$), corresponding to cloud-free conditions; and the spectrum of ratio at infinite COT (denoted as $r_\infty(\lambda)$), corresponding to cloudy conditions. The $r_0(\lambda)$ spectrum (red) is consistently lower than 1.0 at short wavelengths (< 1300 nm) and slightly greater than 1.0 for wavelengths longer than 1500 nm. This suggests that the surface albedo is underestimated for the shorter wavelengths and overestimated for the longer wavelengths. Since changing the snow fraction will only increase or decrease surface albedo for all wavelengths, simply changing the snow fraction does not improve the agreement for both long and short wavelengths. As mentioned before, the albedo we used in the RTM is so called blue-sky albedo, which differs from the white-sky albedo that captured by the measured upwelling irradiance under cloudy condition. Instead, the discrepancies could be caused by the physical changes of the surface, different sun angles, and/or instrument performance changes. The $r_{\infty}(\lambda)$ spectrum (blue) oscillates around 1.0 for the shorter wavelengths and is consistently larger than 1.0 for longer wavelengths, which suggest that the retrieved effective radius is slightly biased. Unfortunately, owing to limited sampling time, the below-cloud flight (13 September) leg does not lend itself to any conclusions from a cloud transmittance perspective since it is not the same cloud field as on 11 September. In future flight campaigns, coordinated above- and below-cloud legs will furnish more information on bias analyses than possible from ARISE.

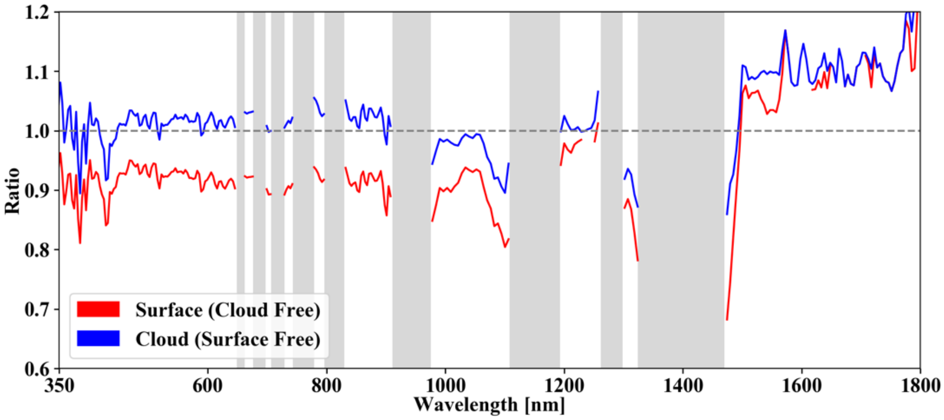

Figure 2.14. The spectrum of ratio when $COT = 0$ (red, indicating cloud free) and when $COT = \infty$ (blue, indicating surface free) for wavelengths range from 350 nm to 1800 nm. The gas absorption bands are indicated in gray. Ratios at the gas absorption bands are excluded.

2.4 Conclusions

In this paper, we used aircraft observations to validate shortwave irradiance derived from satellite passive imagery (MODIS) of low-level cloud fields. This was done with two consecutive flights from the NASA ARISE campaign, which sampled the radiation below and above a cloud field in a similar location of the MIZ. Such validation studies are especially important in the Arctic because observations from the surface are sparse. Despite their limitations, passive imagery products are one of the essential data sources for observationally-based estimates of the surface radiative flux under cloudy conditions, which necessitates a quality assessment of cloud detection and the derivation of cloud optical parameters for a variety of specific cloud and surface types as well as surface angles. In addition, accurate knowledge of the surface albedo and of the water vapor vertical distribution is required to derive the net fluxes at the surface, above the cloud layer, and at the top of atmosphere. The two cases analyzed here only focused on one region with one specific surface and cloud type, but this allowed developing a validation approach that did help answer specific questions such as:

1. What is the reliability of passive imagery cloud detection in the MIZ and over solid snow-covered regions?
2. How much do undetected clouds bias imagery-derived irradiance, especially at the surface?
3. What is the relative magnitude of irradiance errors caused by undetected clouds, biased cloud properties, incorrect surface albedo parameterization, and water vapor?

This paper sheds some light on these questions using the combined measured broadband and spectral irradiance in the study region, but these results are far from representative for the Arctic as a whole. To gain a statistically based understanding, validation data from multiple experiments will have to be combined. By aggregating data from multiple missions, it should be possible to answer more general questions, which a single case study cannot address:

- Do existing cloud climatologies from space-borne passive imagery observations accurately reproduce the frequency of low-level optically thin clouds over different surface types?

- Do existing climatologies of surface albedo capture the spatial and temporal variability sufficiently to keep errors in the derived all-sky irradiance and cloud radiative effects to an acceptable level?

It is unclear what "acceptable" would mean for the second question, but our study showed that the actual surface albedo deviates from commonly used climatologies. Throughout the Arctic, inaccurate knowledge of the surface albedo and its variability will lead to an inaccurate estimation of cloud radiative effects and net surface fluxes, even under clear-sky conditions. This is especially important in the visible part of the spectrum where most of the shortwave energy resides, and where the albedo of different surface types (ice, fresh and old snow) varies significantly. Of course, knowledge of the near-infrared variability of snow and ice albedo (via grain size) is also important because it affects the accuracy of imagery-derived cloud products.

To capture the spatial and spectral variability of the surface, we developed a data aggregation technique that combines collective measurements in a partially snow-covered environment into one spectral surface albedo dataset that is parameterized by snow fraction ("binary" representation of the radiative surface properties). The dataset we obtained agrees with ground-based measurements for the two extremes (called spectral end-members): snow and thin ice. In our case, ice-free open ocean was radiatively insignificant, and the two end-members were sufficient to represent the surface variability. In more complex, more general cases, more end-members will be required.

In assessing the relative magnitude of different errors (question 3 above), we found that undetected clouds have the most significant impact on the imagery-derived irradiance. In the case studied here, MODIS did not detect clouds below a threshold of 0.5 in optical thickness, even when including partially cloud-covered pixels. For the above cloud case, this led to a low bias of up to 13 Wm^{-2} for the upwelling shortwave irradiance. The below cloud case was harder to interpret due to the limited data and the lack of knowledge about the irradiances at cloud top. However, the model-measurement comparison indicated a high bias of at least 86 Wm^{-2} in downwelling shortwave irradiance if clouds are not detected, which again suggested undetected clouds as the dominating error source. While the cloud reflectance (and thereby the TOA cloud radiative effect) bias is minimal (above-cloud case), the cloud transmittance bias (and thereby the surface cloud radiative effect) is significant (below-cloud case). This means that (in reality) the surface would receive less shortwave radiation than derived from satellite imagery and melt less rapidly. Of course, low-level clouds have a warming effect in the longwave. There is, in fact, some indication from land observations (Greenland) that the (longwave) warming effect from thin liquid-bearing clouds dominates (Bennartz et al., 2012). If a large fraction of clouds in the Arctic are not detected (as also reported by Wendisch et al., 2019), this would mean that the surface melt due to clouds would be significantly underestimated. In any case, the performance of passive imagery detection algorithms in the Arctic, along with shortwave and longwave flux biases needs to be systematically studied in the future.

In addition to the bias from undetected clouds, secondary error sources are (a) surface albedo, (b) water vapor content, and (c) cloud optical properties. By using an SSFR-BBR derived surface albedo along with atmospheric profiles from aircraft measurements and MODIS-COPs in the RTM calculations, they agreed with the measured spectral and broadband shortwave irradiance within the range of uncertainties, except in regions where MODIS did not detect clouds. It should be pointed out that in absence of an operational surface albedo product, the surface albedo uncertainty by far dominates the calculated shortwave irradiance error.

While the radiation calculations at TOA can be constrained through the radiation product from satellite observations (e.g., CERES), the radiation calculations at the surface do not have such constraints. The attribution of the individual error contributions was done based on measurements from the SSFR-BBR, by distinguishing the different physical mechanisms based on their spectral dependence. Under some circumstances, the different errors compensate partially in the broadband irradiance.

Generalizing the findings from airborne studies such as these will only be possible by improving satellite remote sensing along the way, which in turn requires airborne observations for the development and validation of a new generation of cloud retrievals in the Arctic. Such retrievals (e.g., Ehrlich et al., 2017) will need to account for surface and cloud variability, and address the issue of undetected thin clouds. A database of spectral albedos, acquired with similar techniques as proposed here, would provide the necessary testbed for developing operational space-based retrievals for surface reflectance as available for the lower latitudes. With lower COT thresholds for cloud detection, spatially and temporally dependent surface albedo, accurate cloud retrievals even for thin clouds, passive remote sensing will significantly improve our current understanding of cloud radiative effects in the Arctic.

Chapter 3

The Education and Research 3D Radiative Transfer Toolbox (EaR^{3}T) – Towards the Mitigation of 3D Bias in Airborne and Spaceborne Passive Imagery Cloud Retrievals

3.1 Background

Three-dimensional cloud effects in imagery-derived cloud properties have long been considered an unavoidable error source when estimating the radiative effect of clouds and aerosols. Consequently, research efforts involving satellite, aircraft, and surface observations in conjunction with modeled clouds and radiative transfer calculations have focused on systematic bias quantification under different atmospheric conditions. Barker and Liu (1995) studied the so-called independent pixel approximation (IPA) bias in cloud optical thickness (COT) retrievals from shortwave cloud reflectance. The bias arises when approximating the radiative transfer relating to COT and measured reflectance at the pixel or cloud column level through one-dimensional (1D) radiative transfer (RT) calculations, while ignoring its radiative context. However, net horizontal photon transport and other effects such as shading engender column-to-column radiative interactions that can only be captured in a three-dimensional (3D) framework, and can be regarded as a 3D perturbation or bias relative to the 1D-RT (IPA) baseline. 3D biases affect not only cloud remote sensing but they also propagate into the derived irradiance fields and cloud radiative effects (CRE). Since the derivation of regional and global CRE relies heavily on satellite imagery, any systematic 3D bias impacts the accuracy of the Earth's radiative budget. Likewise, imagery-based aerosol remote sensing in the vicinity of clouds can be biased by net horizontal photon transport (Marshak et al., 2008). Additionally, satellite shortwave spectroscopy retrievals of CO_2 mixing ratio are affected by nearby clouds (Massie et al., 2017), albeit through a different physical mechanism than in aerosol and cloud remote sensing (Schmidt et al., 2022).

Given the importance of 3D perturbations for atmospheric remote sensing, ongoing research seeks to mitigate the 3D effects. Cloud tomography, for example, inverts multi-angle radiances to infer the 3D cloud extinction distribution (Levis et al., 2020). This is achieved through iterative adjustments to the cloud field until the calculated radiances match the observations. Convolutional neural networks (CNNs, Masuda et al., 2019; Nataraja et al., 2022) account for 3D-RT perturbations in COT retrievals through pattern-based machine learning that operates on collections of imagery pixels, rather than treating them in isolation like IPA. Unlike tomography, CNNs require training based on extensive cloud-type specific synthetic data with the ground truth of cloud optical properties and their associated radiances from 3D-RT calculations. Once the CNNs are trained, they do not require real-time 3D-RT calculations and can therefore be useful in an operational setting. Whatever the future may hold for context-aware multi-pixel or multi-sensor cloud retrievals, there is a paradigm shift on the horizon that started when the radiation concept for the Earth Clouds, Aerosol and Radiation Explorer (EarthCARE, Illingworth et al., 2015) was first proposed (Barker et al., 2012). It foresees a closure loop where broadband radiances, along with irradiance, are calculated in a 3D-RT framework from multi-sensor input fields (Barker et al., 2011), and subsequently compared to independent observations by radiometers pointing in three directions (nadir, forward-, and backward-viewing along the orbit). This built-in radiance closure can serve as an accuracy metric for any downstream radiation products such as heating rates and CRE. Any inconsistencies can be used to nudge the input fields towards the truth in subsequent loop iterations akin to optimal estimation, or propagated into uncertainties of the cloud and radiation products.

This general approach to radiative closure is also being considered for the National Aeronautics and Space Administration (NASA) Atmospheric Observation System (AOS, developed under the A-CCP, Aerosol and Cloud, Convection and Precipitation study), a mission that is currently in its early implementation stages. Owing to its focus on studying aerosol-cloud-precipitation-radiation interactions at the process level, it requires radiation observables at a finer spatial resolution than achieved with missions to date. At target scales close to 1 km, 3D-RT effects are much more pronounced than at the traditional 20 km scale of NASA radiation products (O'Hirok and Gautier, 2005; Ham et al., 2014; Song et al., 2016; Gristey et al., 2020a). Since this leads to biases beyond the desired accuracy of the radiation products, mitigation of 3D-RT cloud remote sensing biases needs to be actively pursued over the next few years.

Transitioning to an explicit treatment of 3D-RT in operational approaches entails a new generation of code architectures that can be easily configured for various instrument constellations, interlink remote sensing parameters with irradiances, heating rates, and other radiative effects, and can be used for automated processing of large data quantities.

Here, we introduce one such tool that could serve as the seed for this transition: the Education and Research 3D Radiative Transfer Toolbox (EaR^{3}T). It has been developed over the past few years at the University of Colorado to automate 3D-RT calculations based on imagery or model cloud fields with minimal user input. EaR^{3}T is maintained and extended by graduate students as part of their education, and applied to various different research projects including machine learning for atmospheric radiation and remote sensing (Gristey et al., 2020b; 2022; Nataraja et al., 2022), as well as radiative closure and satellite simulators (this paper and Schmidt et al., 2022). It is implemented as a modularized Python package with various application codes that combine the functionality in different ways.

The goal of the paper is to introduce EaR^{3}T as a versatile tool for systematically quantifying and mitigating 3D cloud effects in radiation science as foreseen in future missions. To do so, we will first showcase EaR^{3}T as an automated radiance simulator for two satellite instruments, the Orbiting Carbon Observatory-2 (OCO-2, this application is referred to as APP1 in this manuscript) and the Moderate Resolution Imaging Spectroradiometer (MODIS, application code 2, APP2) from publicly available satellite retrieval products. In the spirit of radiance closure, the intended use is the comparison of modeled radiances with the original measurements to assess the accuracy of the input data, as follows: operational IPA COT products are made using 1D-RT, and thus the accompanying radiances are consistent with the original measurements under that 1D-RT assumption only. That is, self-consistency is assured if 1D-RT is used in both the inversion and radiance simulation. However, since nature operates on 3D-RT, we break this traditional symmetry in this manuscript and introduce the concept of 3D radiance consistency where closure is only achieved if the original measurements are consistent with the 3D-RT (rather than the 1D-RT) simulations. The level of inconsistency is then used as a metric for the magnitude of 3D-RT retrieval artifacts as envisioned by the architects of the EarthCARE radiation concept (Barker et al., 2012).

Subsequently, we discuss applications where EaR^{3}T performs radiative closure in the traditional sense, i.e., between irradiances derived from satellite products and collocated airborne or ground-based observations. The aircraft Cloud, Aerosol and Monsoon Processes Philippines Experiment (CAMP^{2}Ex, Reid et al., 2022), conducted by NASA in the Philippines in 2019, serves as a testbed of this approach. Here, we use EaR^{3}T's automated processing capabilities to derive irradiance from geostationary imagery cloud products and then compare these to cumulative measurements made along all flight legs of the campaign (application code 3, APP3). In contrast to previous studies that often rely on a number of cases (e.g., Schmidt et al., 2010a; Kindel et al., 2010), we perform closure systematically for the entire data set, enabling us to identify 3D-RT biases in a statistically significant manner. Finally, we apply a regionally and cloud type specific CNN, introduced by Nataraja et al. (2022) that is included with the EaR^{3}T distribution, to high-resolution camera imagery from CAMP^{2}Ex. This last example demonstrates mitigation of 3D-RT biases in cloud retrievals using the concept of radiance closure to quantify its performance against the baseline IPA (application code 4).

The general concept of EaR^{3}T with an overview of the applications, along with the data used for both parts of the paper is presented in Section 3.2, followed by a description of the procedures of EaR^{3}T in Section 3.3. Results for the OCO-2 and MODIS satellite simulators (part 1) are shown in Section 3.4, followed by the quantification and mitigation of 3D-RT biases with CAMP^{2}Ex data in Section 3.5 and Section 3.6 (part 2). A summary and conclusion are provided in Section 3.7. The code, along with the applications presented in this paper, can be downloaded from the github repository: https://github.com/hong-chen/er3t.

3.2 Functionality and Data Flow within EaR^{3}T

3.2.1 Overview

To introduce EaR^{3}T as a satellite radiance simulator tool and to demonstrate its use for the quantification and mitigation of 3D cloud remote sensing biases, five applications (Figure 3.1) are included in the github software release, four of which are discussed in this paper:

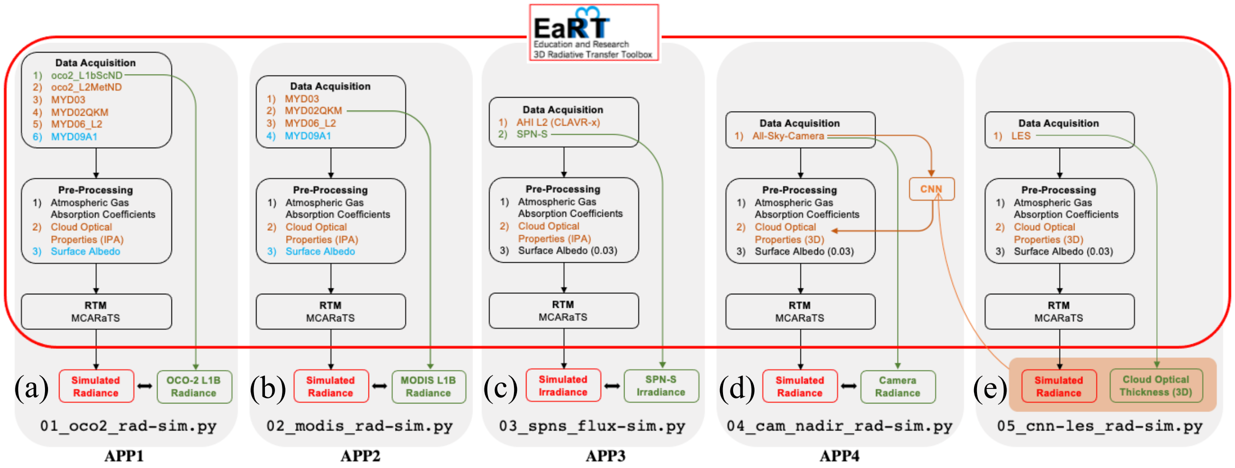

Figure 3.1. Flow charts of EaR^{3}T applications for (a) OCO-2 radiance simulation at 768.52 nm (data described in Section 3.2.2.1 and 3.2.2.2, results discussed in Section 3.4), (b) MODIS radiance simulation at 650 nm (data described in Section 3.2.2.1, results discussed in Section 3.4), (c) SPN-S irradiance simulation at 745 nm (data described in Section 3.2.2.3 and 3.2.2.4, results discussed in Section 3.5), (d) all-sky camera radiance simulation at 600 nm (data described in Section 3.2.2.5, results discussed in Section 3.6), and (e) radiance simulation at 600 nm based on LES data for CNN training (not included in this paper). The data products and their abbreviations are described in Section 3.2.2.

1. APP1, Section 3.4.1 (`examples/01_oco2_rad-sim.py`): Radiance simulations along the track of OCO-2 , based on data products from MODIS and others – to assess consistency (closure) between simulated and measured radiance;
2. APP2, Section 3.4.2 (`examples/02_modis_rad-sim.py`): MODIS radiance simulations – to assess self-consistency of MODIS level-2 (L2) products with the associated radiance fields (L1B product) under spatially inhomogeneous conditions;
3. APP3, Section 3.5 (`examples/03_spns_flux-sim.py`): Irradiance simulations along aircraft flight tracks, utilizing the L2 cloud products of the AHI , and comparison with aircraft measurements – to quantify retrieval biases due to 3D cloud structure based with data from an entire aircraft field campaign;

4. APP4, Section 3.6 (`examples/04_cam_nadir_rad-sim.py`): Mitigation of 3D cloud biases in passive imagery COT retrievals from an airborne camera, application of a convolutional neural network (CNN) and subsequent comparison of CNN-derived radiances with the original measurements – to illustrate how the radiance self-consistency concept assesses the fidelity of cloud retrievals.

Figure 3.1 shows the high-level workflow of the applications. The first four share the general concept of evaluating simulations (the output from the EaR^{3}T, indicated in red at the bottom of each column) with observations (indicated in green at the bottom) from various satellite and aircraft instruments. The results for the four applications are interpreted in Section 3.4.1, Section 3.4.2, Section 3.5, and Section 3.6. The workflow of each application consists of three parts – 1) data acquisition, 2) pre-processing, and 3) RTM setup and execution. EaR^{3}T includes functions to ingest data from various different sources, e.g., satellite data from publicly available data archives, which can be combined in different ways to accommodate input data depending on the application specifics. For example, in APP1, EaR^{3}T is used to automatically download and process MODIS and OCO-2 data files based on the user-specified region, date and time. Building on the templates provided in the current code distribution, the functionality can be extended to new spaceborne or airborne instruments. The fifth column of Figure 3.1 shows an application that differs from the first four, and was developed for earlier papers (Gristey et al., 2020a and 2020b; Nataraja et al., 2022; Gristey et al., 2022). In contrast to the first four, which use imagery products as input, the fifth application ingests model output from a Large Eddy Simulation (LES) and produces irradiance data for surface energy budget applications, or synthetic radiance fields for training a CNN. Details and results are described in the respective papers. Furthermore, Schmidt et al. (2022) builds upon APP1 to study the mechanism of 3D cloud biases in OCO-2 passive spectroscopy retrievals.

After the required data files have been downloaded in the data acquisition step, EaR^{3}T pre-processes them and generates the optical properties of atmospheric gases, clouds, aerosols, and the surface. In Figure 3.1, the mapping from input data to these properties is color-coded component-wise (brown for associated cloud property processing if available, blue for associated surface property processing if available, green for associated ground truth property). Although the current version only includes Monte Carlo Atmospheric Radiative Transfer Simulator (MCARaTS, Iwabuchi, 2006) as the 3D RT solver, EaR^{3}T is designed to be modular so as to employ various different solvers. To achieve this flexibility, pre-processing is a required intermediate step since different RT solvers interface with the input data differently. Although the four applications included in this paper do not take aerosol layers into consideration, the setup of processing optical properties for aerosols is supported and has been used in other applications, such as studying cloud-aerosol radiative effects based on LES data (Gristey et al., 2022). After pre-processing, the optical properties are fed into the RT solver. Finally, the user obtains radiation output from EaR^{3}T, either radiance or irradiance. The output is saved in HDF5 format and can be easily distributed and accessed by various programming languages. The data variables contained in the HDF5 output are provided in Table 3.1.

Metadata			
Variable Name	Description	Data Type	Dimension
`mean/N_photon`	Number of photons per run	Array	N_g
`mean/N_run`	Number of runs	Integer value	N/A
`mean/toa`	TOA downwelling flux	Float value	N/A

Radiance			
Variable Name	Description	Data Type	Dimension
`mean/rad`	Radiance field at user specified altitude averaged over different runs	Array	(N_x, N_y)
`mean/rad_std`	Standard deviation of the radiance fields from different runs	Array	(N_x, N_y)
Irradiance			
Variable Name	Description	Data Type	Dimension
`mean/f_down`	Downwelling irradiance averaged over different runs	Array	(N_x, N_y, N_z)
`mean/f_down_std`	Standard deviation of the downwelling irradiance from different runs	Array	(N_x, N_y, N_z)
`mean/f_down_diffuse`	Diffuse downwelling irradiance averaged over different runs	Array	(N_x, N_y, N_z)
`mean/f_down_diffuse_std`	Standard deviation of the diffuse downwelling irradiance from different runs	Array	(N_x, N_y, N_z)
`mean/f_down_direct`	Direct downwelling irradiance averaged over different runs	Array	(N_x, N_y, N_z)
`mean/f_down_direct_std`	Standard deviation of the direct downwelling irradiance from different runs	Array	(N_x, N_y, N_z)
`mean/f_up`	Upwelling irradiance averaged over different runs	Array	(N_x, N_y, N_z)
`mean/f_up_std`	Standard deviation of the upwelling irradiance from different runs	Array	(N_x, N_y, N_z)

Table 3.1. Data variables contained in the output HDF5 file from EaR^{3}T for radiance and irradiance calculations. The radiance is simulated with a user-specified sensor geometry at a given altitude using forward photon tracing. The data variables listed under Metadata are included for both radiance and irradiance calculations. N_x, N_y, and N_z are the number of pixels along x, y, and z direction, respectively. N_g is the number of g, explained in Section 3.3.

The aforementioned three steps – data acquisition, pre-processing, and RTM setup and execution are automated such that the 3D/1D-RT calculations can be performed for any region at any date and time using satellite or aircraft data or other data resources such as LES. EaR^{3}T is hosted on Github at https://www.github.com/hong-chen/er3t. Since it is developed as an educational and research 3D-RT tool collection by students, it is a living code base, intended to be updated over time. The master code modules for the four applications as listed in Figure 3.1 are included in the EaR^{3}T package under the `examples` directory.

3.2.2 Data

The radiance simulations in APP1 and APP2 use data from the OCO-2 and MODIS-Aqua instruments, both of which are in a sun-synchronous polar orbit with an early-afternoon equator crossing time within NASA's A-Train satellite constellation. Figure 3.2 visualizes radiance measurements by OCO-2 in the context of MODIS Aqua imagery over a partially vegetated and partially cloud-covered land, illustrating that MODIS provides imagery and scene context for OCO-2, which in turn observes radiances from a narrow swath. The region is located in southwest Colorado in the United States of America. We selected this case because both the surface and clouds are varied along with diverse surface types. The surface features green forest and brown soil, whereas clouds include small cumulus and large cumulonimbus. In addition, this scene contains relatively homogeneous cloud fields in the north and inhomogeneous cloud fields in the south, which allows us to evaluate the simulations from various aspects of cloud morphology. To simulate the radiances of both instruments we use data products from OCO-2 and MODIS, as well as reanalysis products from NASA's Global Modeling and Assimilation Office (GMAO) sampled at OCO-2 footprints and distributed along with OCO-2 data (Section 3.2.2.2).

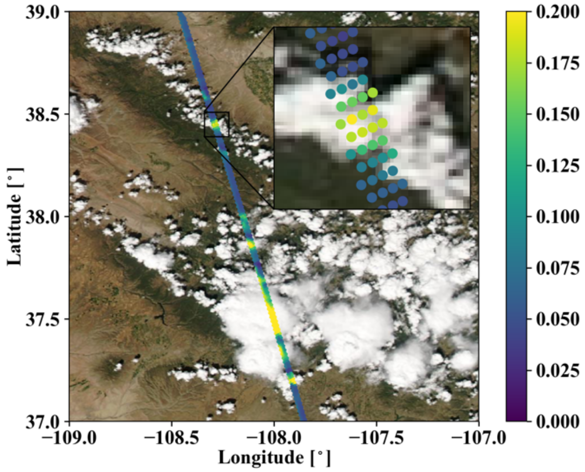

Figure 3.2. OCO-2 measured radiance (units: $Wm^{-2}nm^{-1}sr^{-1}$) at 768.52 nm, overlaid on MODIS Aqua RGB imagery over southwestern Colorado (USA) on 2 September, 2019. The inset shows an enlarged portion along the track, illustrating that OCO-2 radiances co-vary with MODIS-Aqua radiance observations.

For APP3 (irradiance simulations and 3D cloud bias quantification), we use geostationary imagery from the Japanese Space Agency's Advanced Himawari Imager to provide cloud information in the area of the flight path of the NASA CAMP^{2}Ex aircraft (Reid et al., 2022). The AHI data are used in conjunction with aircraft measurements of shortwave spectral radiation (Section 3.2.2.4). Subsequently (APP4: 3D cloud bias mitigation), we demonstrate the concept of radiance closure under partially cloudy conditions with airborne camera imagery (Section 3.2.2.5). The underlying cloud retrieval is based on a convolutional neural network (CNN), which is described in a related paper (Nataraja et al., 2022) in this special issue and relies on EaR^{3}T-generated synthetic radiance data based on Large Eddy Simulations (LES).

3.2.2.1 Moderate Resolution Imaging Spectroradiometer (MODIS)

MODIS is currently flying on NASA's Terra and Aqua satellites, launched in 1999 and 2002 respectively. They are multi-use multispectral radiometers conceived as central elements of the Earth Observing System (EOS, King and Platnick, 2018). For APP1 and APP2, EaR^{3}T ingests MODIS level 1B radiance products at the quarter kilometer scale (channels 1 and 2, MxD02QKM, where 'x' stands for 'O' in the case of MODIS on Terra, and 'Y' in the case of Aqua data), the geolocation product (MxD03), the level 2 cloud product (MxD06), and the surface reflectance product (MxD09A1). For this paper, we use only Aqua data (MYD), from data collection 6.1. All the data are publicly available, and are distributed at the LAADS (Level-1 and Atmosphere Archive & Distribution System) Distributed Active Archive Center (DAAC) by NASA's Goddard Space Flight Center.

For cloud properties in APP2, we use the MODIS cloud product (MxD06L2, collection 6.1). It provides cloud properties such as cloud optical thickness (COT), cloud effective radius (CER), cloud thermodynamic phase, cloud top height (CTH), etc. (Nakajima and King, 1990; Platnick et al., 2003). Since 3D cloud effects such as horizontal photon transport are most significant at small spatial scales (e.g., Song et al., 2016), we use the high-resolution red (650 nm) channel 1 (250 m), and derive COT directly from the reflectance in the Level-1B data (MYD02QKM) instead of using the coarser-scale operational product from MYD06. CER and CTH are sourced from MYD06 and re-gridded to 250 m. The EaR^{3}T strategy for MODIS data is similar, in principle, to the more advanced method by Deneke et al. (2021), which uses a high-resolution wide-band visible channel from geostationary imagery to up-sample narrow-band coarse-resolution channels. However, we simplified cloud detection and derivation of COT from reflectance data for the purpose of our paper by using a threshold method (Appendix 3.A) and the two-stream approximation (Appendix 3.B). In future versions of EaR^{3}T this will be upgraded to more sophisticated algorithms. A simple algorithm (Appendix 3.C) is used to correct for the parallax shift based on the sensor geometries and cloud heights. The cloud top height data is provided by the MODIS L2 cloud product and assuming cloud base is the same.

For the surface reflectance, we used MYD09A1, for which cloud-cleared observations are aggregated over an 8-day period (Vermote et al., 2015). This product is available on a sinusoidal grid with a spatial resolution of 500 m for MODIS band 2, and includes atmospheric correction for gas and aerosol scattering and absorption.

3.2.2.2 Orbiting Carbon Observatory 2 (OCO-2)

The OCO-2 satellite was inserted into NASA's A-Train constellation in 2014 and flies about 6 minutes ahead of Aqua. OCO-2 provides the column-averaged carbon dioxide (CO_2) dry-air mole fraction (XCO_2) through passive spectroscopy based on hyperspectral radiance observations in three narrow wavelength regions, the Oxygen A-Band (~0.76 micron), the weak CO_2 band (~1.60 micron), and the strong CO_2 band (~2.06 micron). As shown in the inset of Figure 3.2, it takes measurements in eight footprints across a narrow swath. Each of the footprints has a size around 1-2 km, and the spectra for the three bands are provided by separate, co-registered spectrometers (Crisp et al., 2015).

The OCO-2 data products of 1) Level 1B calibrated and geolocated science radiance spectra (L1bScND), 2) standard Level 2 geolocated XCO_2 retrievals results (L2StdND), 3) meteorological parameters interpolated from GMAO (L2MetND) at OCO-2 footprint location are downloaded from NASA GES DISC (Goddard Earth Science Data Archive and Information Services Center) data archive (https://oco2.gesdisc.eosdis.nasa.gov/data/OCO2_DATA). Since MODIS on Aqua overflies a scene 6 minutes after OCO-2, the clouds move with the wind over this time period. We therefore added a wind correction on top of the parallax-corrected cloud fields obtained from MODIS (Section 3.2.2.1). This was done with the 10 m wind speed data from L2MetND (see Appendix 3.D). For the same scene as shown in Figure 3.2, Figure 3.3 shows (a) COT, (b) CER, and (c) CTH, all corrected for both parallax and wind effect.

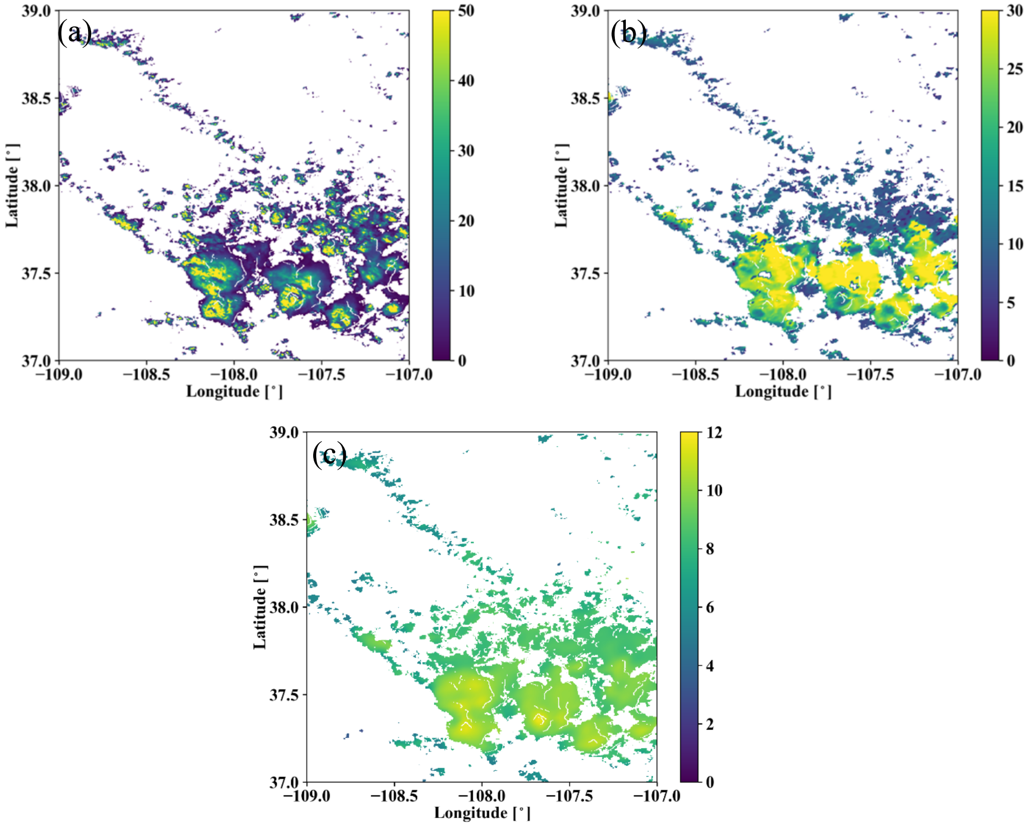

Figure 3.3. **(a)** Cloud optical thickness derived from MODIS L1B radiance at 650 nm by the two-stream approximation (Equation 3.A2), **(b)** cloud effective radius (units: μm), and **(c)** cloud top height (units: km) collocated from the MODIS L2 cloud product. The locations of the cloudy pixels were shifted to account for parallax and wind effects. The parallax correction ranged from near 0 for low clouds and 1 km for high clouds (10 km CTH). The wind correction was around 0.8 km, given the average wind speed of 2 m/s to the east.

The OCO-2 data (L2StdND) themselves only provide sparse surface reflectance for the footprints that are clear, while EaR^{3}T requires surface albedo for the whole domain. Therefore, we used MYD09A1 as a starting point. However, since MODIS does not have a channel in the Oxygen

A-Band, MODIS band 2 (860 nm) was used as a proxy for the 760 nm OCO-2 channel as follows: we collocated the OCO-2 retrieved 760 nm surface reflectance R_{OCO} within the corresponding 860 nm MODIS MYD09A1 data R_{MOD} as shown in Figure 3.4a (same domain as Figures 3.2 and 3.3) and calculated a scaling factor assuming a linear relationship between R_{OCO} and R_{MOD} ($R_{OCO} = a \cdot R_{MOD}$). Figure 3.4b shows R_{OCO} versus R_{MOD} for all cloud-free OCO-2 footprints. The red line shows a linear regression (derived scale factor $a=0.93$). Scaling is also applied for the weak and strong CO_2 channels, even though there are matching MODIS channels. Optionally, the OCO-2-scaled MODIS-derived surface reflectance fields can be replaced by the OCO-2 surface reflectance products for pixels where they are available.

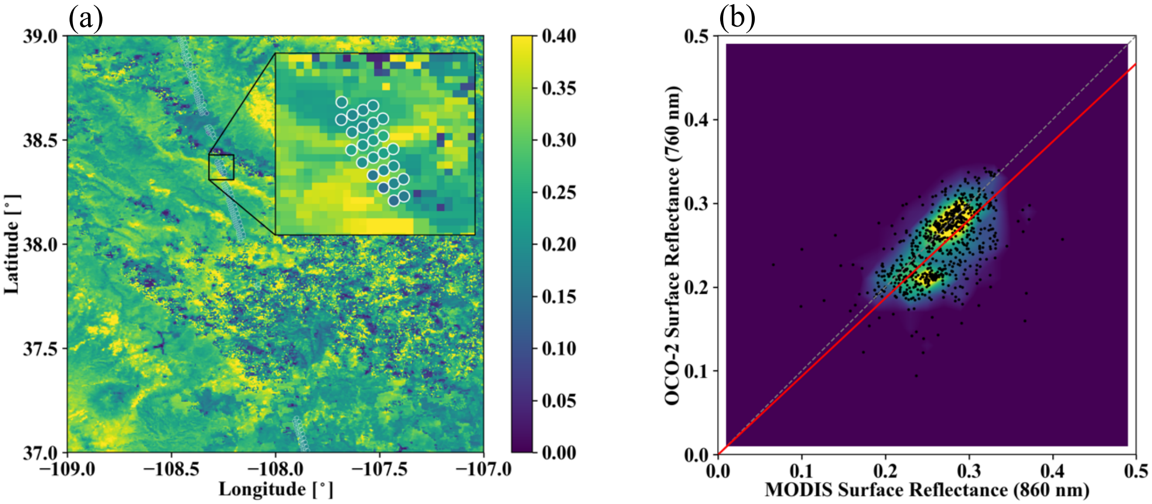

Figure 3.4. **(a)** Surface reflectance from the OCO-2 L2 product in the Oxygen A-band (near 760 nm), overlaid on the surface reflectance from the MODIS MYD09 product at 860 nm. **(b)** OCO-2 surface reflectance at 760 nm versus MODIS surface reflectance at 860 nm, along with linear regression ($y=ax$) as indicated by the red line (slope $a=0.9337$).

3.2.2.3 Advanced Himawari Imager (AHI)

The Advanced Himawari Imager (AHI, used for APP3) is a payload on Himawari-8, a geostationary satellite operated by the Meteorological Satellite Center (MSC) of the Japanese Meteorological Agency. The AHI provides 16 channels of spectral radiance measurements from the shortwave (0.47μm) to the infrared (13.3μm). During CAMP^{2}Ex, the NASA in-field operational team closely collaborated with the team from MSC to provide AHI satellite imagery at the highest resolution over the Philippine Sea. From the AHI imagery, the cloud product generation system – Clouds from AVHRR Extended System (CLAVR-x), was used to generate cloud products from the AHI imagery (Heidinger et al., 2014). The cloud products from CLAVR-x include cloud optical thickness, cloud effective radius, and cloud top height at 2 (at nadir) to 5 km spatial resolution. Since AHI provides continuous regional scans every 10 minutes the AHI cloud product has a temporal resolution of 10 minutes.

3.2.2.4 Spectral Sunshine Pyranometer (SPN-S)

The SPN-S is a prototype spectral version of the commercially available global-diffuse SPN1 pyranometer (Wood et al., 2017; Norgren et al., 2022). The radiometer uses a 7-detector design in combination with a fixed shadow mask that enables the simultaneous measurement of both diffuse and global irradiances, from which the direct component of the global irradiance is calculated via subtraction. The detector measures spectral irradiance from 350 to 1000 nm, and the spectrum is sampled at 1 nm resolution with 1 Hz timing.

During the CAMP^{2}Ex mission, the SPN-S was mounted to the top of the NASA P-3 aircraft where it sampled downwelling solar irradiance. To ensure accurate measurements, pre- and post-mission laboratory-based calibrations were completed using tungsten “FEL” lamps that are traceable to a National Institute of Standards and Technology standard. Additionally, the direct and global irradiances were corrected for deviations of the SPN-S sensor plane from horizontal that are the result of changes in the aircraft’s pitch or roll. This attitude correction applied to the irradiance data is a modified version of the method outlined in Long et al. (2010). However, whereas Long et al. (2010) employ a “box” flight pattern to characterize the sensor offset angles, in this study an aggregation of flight data containing aircraft heading changes under clear-sky conditions is used as a substitute. The estimated uncertainty of the SPN-S system is 6 to 8%, with 4 to 6% uncertainty stemming from the radiometric lamp calibration process, and up to another 2% resulting from insufficient knowledge of the sensor cosine response. The stability of the system under operating conditions is 0.5%. A thorough description of the SPN-S and its calibration and correction procedures is provided in Norgren et al. (2022). In this paper (APP3) only the global downwelling irradiance sampled by the 745 nm channel is used.

3.2.2.5 Airborne All-Sky Camera (ASC)

The All-Sky Camera (used for APP4) is a commercially available camera (ALCOR ALPHEA 6.0CW[3]) with fish-eye optics for hemispheric imaging. It has a Charge-Coupled Device (CCD) detector that measures radiances in red, green, and blue channels. Radiometric and geometric calibrations were performed at the Laboratory of Atmospheric and Space Physics at the University of Colorado Boulder. The three-color channels are centered at 493, 555, and 626 nm for blue, green, and red, respectively, with bandwidths of 50 – 100 nm. Only radiance data from the red channel were used in this paper. The spatial resolution of the ASC depends on the altitude of the aircraft and the viewing zenith angle. Across the hemispheric field of view of the camera, the resolution of the field angle is approximately constant, at about 0.09°. At a flight level of 5 km, this translates to a spatial resolution of 8 m at nadir. However, due to accuracy limitations of the geometric calibration and the navigational data from Inertial Navigation System (INS), the nadir geolocation accuracy could only be verified to within ±50 m. During the CAMP^{2}Ex flights, the

---

[3] https://www.alcor-system.com/common/allSky/docs/ALPHEA_Camera%20ALL%20SKY%20CAMERA_Doc.pdf last accessed on April 24, 2022.

camera exposure time was set manually to minimize saturation of the detector. The standard image frame rate is 1 Hz. The precision of the camera radiances is on the order of 1%, and the radiometric accuracy is 6 – 7%.

3.3. EaR^{3}T Procedures

In the previous Section, we described the general workflow of EaR^{3}T applications, along with relevant data. In this Section, we will focus on the specific implementation of the workflow through the EaR^{3}T software package. It is a toolbox for 3D-RT with modules for automatic input data download and processing, generation of radiative and optical properties of surface, atmospheric gases, clouds and aerosols, wrappers for 3D-RT solvers and output post-processing, with the end goal to simulate radiances and irradiances along entire satellite orbits or aircraft flight tracks. Unlike established radiative transfer packages such as libRadtran (Mayer and Kylling, 2005; Emde et al., 2016), which provide extensive libraries of optical properties along with a selection of solvers, EaR^{3}T focuses on automated radiative transfer for two- or three-dimensional cloud, aerosol, and surface input data, and therefore only comes with minimal options for optical properties, and solvers. The initial release is available at https://github.com/hong-chen/er3t.

We will now walk through the OCO-2 and MODIS simulator applications with the codes `examples/01_oco2_rad-sim.py` (APP1) and `examples/02_modis_rad-sim.py` (APP2). The data acquisition (first step in Figure 3.1) uses functions in `er3t/util`. APP1 and APP2 use the functions in `er3t/util/modis.py` and `er3t/util/oco.py` for downloading the MODIS and OCO-2 data files from the respective NASA data archives and for processing the data (e.g., geo-mapping, gridding etc.). The user supplies minimum input (date and time, as well as latitudes and longitudes of the region of interest), which need to be specified in `download_modis_https` and `download_oco2_https` (from `er3t/util`). For example, for APP1 and APP2, the only user inputs are the date and time and the region of interest – in this case September 2, 2019, with the westernmost, easternmost, southernmost, and northernmost longitudes and latitudes of 109°W, 107°W, 37°N, and 39°N. In order for EaR^{3}T to access any data archives such as NASA Earthdata, the user needs to create an account with them and store the credentials locally (detailed instructions are provided separately along with the EaR^{3}T distribution).

After the data acquisition step, the satellite data are fed into the pre-processing step for 1) atmospheric gases (`er3t/pre/atm`), 2) clouds (`er3t/pre/cld`), 3) surface (`er3t/pre/sfc`) as shown in Figure 3.1. In the default configuration of the APP1, the standard US atmosphere (Anderson et al., 1986; included in the EaR^{3}T repository) is used within `atm`. EaR3T supports the input of user-specified atmospheric profiles, e.g., atmospheric profiles from reanalysis data for APP2 as described in Schmidt et al. (2022), by making changes in `atm_atmmod` (from `er3t/pre/atm`). Subsequently, molecular scattering coefficients are calculated by `cal_mol_ext` (from `er3t/util`), and absorption coefficients for atmospheric gases are generated by (`er3t/pre/abs`). At the current development stage, two options are available:

1. Line-by-line (used by APP1): The repository includes a sample file of absorption coefficient profiles for a subset of wavelengths within OCO-2's Oxygen A-Band channel, corresponding to a range of atmospheric transmittance values from low (opaque) to high (so-called "continuum" wavelength). They were generated by an external code (Schmidt et al., 2022) based on OCO-2's line-by-line absorption coefficient database (ABSCO, Payne et al., 2020). For each wavelength, there are hundreds of individual absorption coefficient

profiles, spectrally spaced at the native resolution of ABSCO, and ranging across the instrument line shape (ILS, also known as the slit function) of the OCO-2 Oxygen A-Band spectrometer. The ILS, as well as the incident solar irradiance, are also included in the file. In subsequent steps, EaR^{3}T performs RT calculations at the native spectral resolution of ABSCO, but then combines the output by convolving with the ILS and outputs OCO-2 radiances or reflectances at the subset of wavelengths. For probabilistic (Monte Carlo) RT solvers such as MCARaTS, the number of photons can be kept relatively low (e.g., 10^6 photons), and can be adjusted according to the values of the ILS at a particular ABSCO wavelength. Any uncertainty at the ABSCO spectral resolution due to photon noise is greatly reduced by convolving with the ILS for the final output.

2. Correlated-k (used by APP2): This approach (Mlawer et al., 1997) is appropriate for instruments such as MODIS with much coarser spectral resolution than OCO-2, as well as for broadband calculations. In contrast to the line-by-line approach, RT calculations are not performed at the native resolution of the absorption database, but at Gaussian quadrature points (called “g’s”) that represent the full range of sorted absorption coefficients, and then combined using Gaussian quadrature weights. The repository includes an absorption database from Coddington et al. (2008), developed specifically for a radiometer with moderate spectral resolution on the basis of HITRAN (high-resolution transmission molecular absorption database) 2004 (Rothman et al., 2005). It was created for the ILS of the airborne Solar Spectral Flux Radiometer (SSFR, Pilewskie et al., 2003), but is applied to MODIS here, which has a moderate spectral resolution of 8-12 nm with 20-50 nm bandwidths. It uses 16 absorption coefficient bins (g’s) per target wavelength, which are calculated by EaR^{3}T with the Coddington et al. (2008) database using the mixing ratios of

atmospheric gases in the previously ingested profile. In future implementations, the code will be updated to enable flexible ILS and broadband calculations.

The `er3t/pre/cld` module calculates extinction, thermodynamic phase, and effective droplet radius of clouds from the input data. The `er3t/pre/pha` module creates the required single scattering albedo and scattering phase function. The default is a Henyey-Greenstein phase function with a fixed asymmetry parameter of 0.85. It is, however, recommended to also install libRadtran to enable the usage of Mie phase functions based on thermodynamic phase, effective droplet radius, and wavelength. In this study, APP1 and APP2 use Mie phase functions calculated from Legendre polynomial coefficients distributed along with libRadtran based on the wavelength cloud droplet effective radius. In the future, EaR^{3}T will include stand-alone phase functions, which can be chosen on the basis of droplet size distributions in addition to effective radius. It is also possible to include aerosols in a similar fashion as clouds. This is done with the `er3t/pre/aer` module. In the case of aerosols, spectral single scattering albedo and asymmetry parameter are required as inputs in addition to the extinction fields.

After the optical properties are calculated, they are passed into the 3D-RT step (`er3t/rtm/mca`). In addition to MCARaTS, planned solvers for the future include MYSTIC (Monte Carlo code for the physically correct tracing of photons in cloudy atmospheres, Mayer, 2009) and SHDOM (Spherical Harmonic Discrete Ordinate Method, Evans, 1998; Pincus and Evans, 2009). This step performs the setup of RT solver-specified input parameters and data files, distributing runs over multiple CPUs, and post-processing RT output files into a single, user-friendly HDF5 file. For example, when radiance is specified as output (default in APP1 and APP2), key information such as the radiance field and its standard deviation are stored in the final

HDF5 file (details see Table 1). The EaR^{3}T documentation only provides detailed instructions of installing the RT solvers (currently only MCARaTS) and libRadtran.

While the EaR^{3}T repository comes with various applications such as APP1 and APP2, described above, the functions used by these master or ‘wrapper’ programs can be organized in different ways, where the existing applications serve as templates for a quick start when developing new applications. The functions used by the master code pass information through the various steps as Python objects. For example, in `examples/01_oco2_rad-sim.py`, the downloaded and processed satellite data are stored into the `sat` object. Later, the `sat` object is passed into an EaR^{3}T function to create the `cld` object that contains cloud optical properties. Similarly, EaR^{3}T provides functions to create the `atm`, and `sfc` objects with optical properties for atmospheric gases and the surface. These objects (`atm`, `cld`, `sfc`) are in turn passed on to solver-specific modules for performing RT calculations. The user can choose to save the data of the intermediate objects into Python pickle files after the first run. In this way, multiple calls with identical input can re-use existing data, which accelerates the processing time of EaR^{3}T. Unless the user specifies the `overwrite` keyword argument in the object call to reject saving pickle files, these shortcuts save significant time. Moreover, EaR^{3}T is capable of distributing simulations over multiple CPUs to accelerate the calculations, which is useful for potential future application of later EaR^{3}T or EaR^{3}T-like codes in operational or large-scale data processing.

In the following sections, we discuss results obtained from EaR^{3}T, starting with those from `examples/01_oco2_rad-sim.py` and `examples/02_modis_rad-sim.py` (Section 3.4), `examples/03_spns_flux-sim.py` (Section 3.5), and concluding with `examples/04_cam_nadir_rad-sim.py` (Section 3.6). The detailed RT setup for the four applications is provided in Table 3.2.

	APP1 - Radiance for MODIS	APP2 - Radiance for OCO-2	APP3 - Irradiance for SPN-S	APP4 - Radiance for CNN/ASC
Wavelength	760 nm	650 nm	745 nm	600 nm
Atmospheric profile	US Standard Atmosphere	Reanalysis	AFGL - Tropical Summer	AFGL - Tropical Summer
Solar zenith and azimuth angles	Acquired from OCO-2 data	Acquired from MODIS data	Calculated from aircraft navigational data	Calculated from aircraft navigational data
Surface albedo	Scaled from MYD09A1	Acquired from MYD09A1	0.03	0.03
Sensor zenith and azimuth angles	Acquired from OCO-2 data	Acquired from MODIS data	Zenith	Nadir
Cloud Optical Thickness	Retrieved from MODIS reflectance through IPA method	Retrieved from MODIS reflectance through IPA method	Acquired from AHI L2 Cloud Product	Retrieved through 1) IPA method, 2) CNN model
Cloud effective radius	Acquired from MYD06L2	Acquired from MYD06L2	N/A	N/A
Phase function	Mie	Mie	Henyey-Greenstein (g=0.85)	Henyey-Greenstein (g=0.85)
Cloud location	CTH from MYD06L2 minus 1 km to CTH	CTH from MYD06L2 minus 1 km to CTH	2 km to 3 km	1 km to 2 km
Number of Photons	1×10^8	1×10^8	1×10^7	1×10^8

Table 3.2: RT parameters for APP1, APP2, APP3, and APP4.

3.4. EaR^{3}T as a 3D Satellite Radiance Simulator

This section demonstrates the automated 3D radiance simulation for satellite instruments by EaR^{3}T for OCO-2 and MODIS measured radiance based on publicly available MODIS retrieval products. The OCO-2 application is an example of radiance consistency between two distinct satellite instruments where the measurements of one (here, OCO-2) are compared with the simulations based on data products from the other (here, MODIS). The MODIS application, on the other hand, is an example of radiance self-consistency. We will show how inconsistencies can be used for detecting cloud and surface property retrieval biases.

3.4.1 OCO-2 (APP1)

The OCO-2 radiance measurements at 768.52 nm for our sample scene in the context of MODIS imagery were shown in Figure 3.2. For that track segment, Figure 3.5 shows the simulated radiance along with the measurements as a function of latitude. The radiance was averaged over every 0.01° latitude window from 37° N to 39° N (the standard deviation within the bin indicated by the shaded color). In clear-sky regions (e.g., around 38.2º N), the simulations (red) are systematically higher than the measurements (black), even though the footprint-level OCO-2 retrieval was used to scale the MYD09 field as described in Section 3.2.2.2 (Figure 3.4). This is because, unlike the MYD09 algorithm which relies on multiple overpasses and multiple-days for cloud-clearing, the OCO-2 retrieval is done for any clear footprint. Clouds in the vicinity lead to enhanced diffuse illumination that is erroneously attributed to the surface reflectance itself. The EaR^{3}T IPA calculations of the clear-sky pixels (blue) essentially reverse the 3D effect and therefore match the observations better. The 3D calculations enhance the reflectance through the very same 3D cloud effects that led to the enhanced surface illumination in the first place. It is possible to correct this effect by down-scaling the surface reflectance according to the ratio between clear-sky 3D and IPA calculations, but this process is currently not automated.

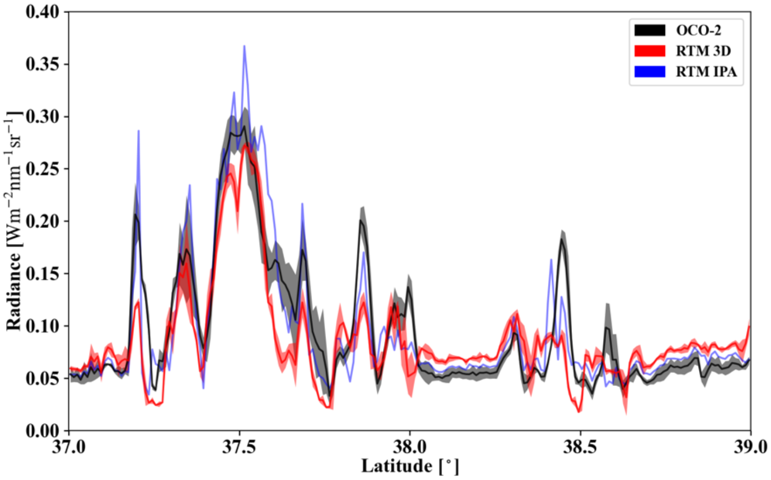

Figure 3.5. Latitudinally averaged (0.01° spacing) radiance calculations from EaR^{3}T (red: 3D, blue: IPA) and OCO-2 measured radiance at 768.52 nm (black). The solar zenith angle for the radiance simulation case is 33.75°.

In the cloudy locations, the IPA calculations match the OCO-2 observations on a footprint-by-footprint level, demonstrating that wind and parallax corrections were performed successfully. Of course, there is not always a perfect agreement because of morphological changes in the cloud field over the course of six minutes. It is, however, apparent that the 3D calculations agree to a much lesser extent with the observations than the IPA calculations. Just like the mismatch for the clear-sky pixels indicates a bias in the input surface reflectance, the bias here means that the input cloud properties (most importantly COT) are inaccurate. For most of the reflectance peaks, the 3D simulations are too low, which means that the input COT is biased low. This is due to 3D cloud effects on the MODIS-based cloud retrieval. Since they are done with IPA, any net horizontal photon transport is not considered, which leads to an apparent surface brightening as noted above, at the expense of the cloud brightness. As a result, the COT from darker clouds is significantly underestimated. This commonly known problem, with several aspects discussed in the subsequent EaR^{3}T applications, can be identified by radiance consistency checks such as the one shown in Figure 3.5, and mitigated by novel types of cloud retrievals that do take horizontal photon transport into account (Section 3.6).

3.4.2 MODIS (APP2)

To go beyond the OCO-2 track and understand the bias between simulated and observed radiances from a domain perspective, we now consider the radiance simulations for the MODIS 650 nm channel. The setup is exactly the same as for the OCO-2 simulations, except that 1) the viewing zenith angle is set to the average viewing zenith angle of MODIS within the shown domain (instead of OCO-2), and 2) the surface reflectances from MYD09 are used directly, this time from the 650 nm channel without rescaling. Figure 3.6a shows the MODIS measured radiance field, while Figure 3.6b shows the EaR^{3}T 3D simulations. Visually, the clouds from the EaR^{3}T simulation are generally darker than the observed clouds, which is in line with our aforementioned explanation of net horizontal photon transport. They are also blurrier because radiative smoothing (Marshak et al., 1995) propagates into the retrieved COT fields, which are subsequently used as input to EaR^{3}T. To look at darkening and smoothing effects more quantitatively, Figure 3.7 shows a heatmap plot of simulated radiance versus observed radiance. It shows that the radiance for cloud-covered pixels (labeled “cloudy”) from EaR^{3}T are mostly low-biased while good agreement between simulations and observations was achieved for clear-sky radiance (labeled “clear-sky”). The good agreement over clear-sky regions is expected. As mentioned above, we use MYD09 as surface reflectance input, which in contrast to the OCO-2 surface reflectance product is appropriately cloud-screened and therefore does not have a reflectance high bias. There is, of course, a reflectance enhancement in the vicinity of clouds, but that is captured by the EaR^{3}T calculations. The fact that the calculations agree with the observations even for clear-sky pixels in the vicinity of clouds, shows that the concept of radiance consistency works to ensure correct satellite retrievals even in presence of clouds. It also corroborates our observation from Section 3.4.1 that $\mathrm{COT}_{\mathrm{IPA}}$ is low biased. Since the MODIS reflectance is not self-consistent with respect to $\mathrm{COT}_{\mathrm{IPA}}$ as shown for the cloudy pixels in Figure 3.7, we can identify a bias in the cloud properties even without knowing the ground truth of COT. On the other hand, successful closure in radiance (self-consistency) would provide an indication that the input fields including COT are accurate, although it is certainly a weaker metric than direct verification of the retrievals through aircraft satellite retrieval validation with in-situ instruments.

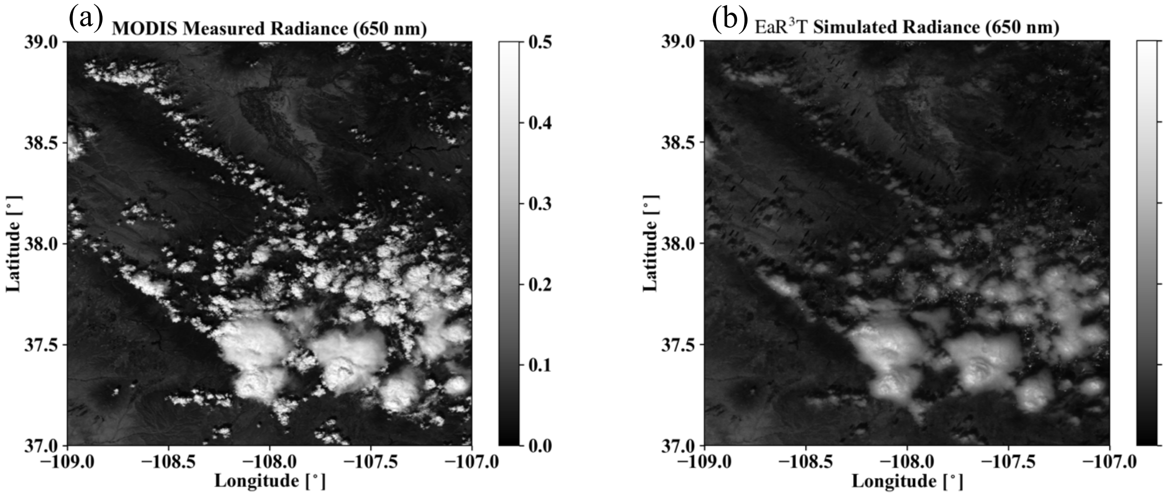

Figure 3.6. **(a)** MODIS measured radiance in channel 1 (650 nm). **(b)** Simulated 3D radiance at 650 nm from $\mathrm{EaR^3T}$. The solar zenith angle for the radiance simulation case is 34.42°.

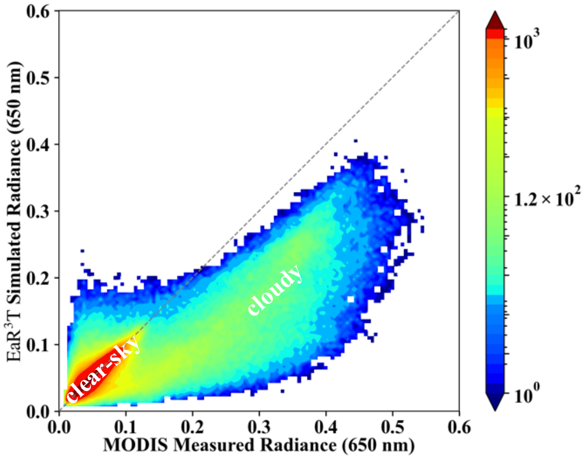

Figure 3.7. Heatmap plot of EaR^{3}T simulated 3D radiance vs. MODIS measured radiance at 650 nm.

Summarizing the two satellite radiance simulator applications, one can say that EaR^{3}T enables a radiance consistency check for inhomogeneous scenes. We demonstrated that a lack of simulation-observation consistency (MODIS versus OCO-2) and self-consistency (MODIS versus MODIS) can be traced back to biased surface reflectance or cloud fields in the simulator input. This can become a diagnostic tool for the quality of retrieval products from future or current missions, even when the ground truth is not known.

For technical reference: The MODIS simulation took about one hour on a Linux workstation with 12 CPUs for three 3D RT runs with 10^8 photons each. With a slightly modified setup and parallelization, the automation can be easily applied for entire satellite orbits, although more research is required to optimize the computation speed depending on the desired output accuracy.

3.5. EaR^{3}T as 3D Aircraft Irradiance Simulator (APP3)

In contrast to the previous applications that focused on satellite remote sensing, we will now be applying EaR^{3}T to quantify 3D cloud retrieval biases through direct, systematic validation of imagery-derived irradiances against aircraft measurements, instead of using the indirect path of radiance consistency in Section 3.4. Previous studies (e.g., Schmidt et al., 2007; Kindel et al., 2010) conducted radiative closure between remote sensing derived and measured irradiance using isolated flight legs as case studies. Here, with the efficiency afforded by the automated nature of EaR^{3}T, we are able to conduct radiative closure of irradiance through a statistical approach that employs campaign-scale amounts of measurement data. Specifically, we used EaR^{3}T to perform large-scale downwelling irradiance simulations at 745 nm based on geostationary cloud retrievals from AHI for the CAMP^{2}Ex campaign, and directly compare these simulations to the SPN-S measured irradiances onboard the P-3 aircraft. This is done for all below-cloud legs from the entire campaign with the aim to assess the degree to which satellite-derived near-surface irradiances reproduce the true conditions below clouds.

The irradiance simulation process is similar to the previously described radiance simulation in Section 3.4, with only a few modifications. First, we used cloud optical properties from the AHI cloud product (COT, CER and CTH) as direct inputs into EaR^{3}T. Secondly, we used a constant ocean surface reflectance value of 0.03. Such simplification in surface albedo is made under the assumption that 1) the ocean surface is calm with no whitecaps, and that 2) the Lambertian bidirectional reflectance distribution function (BRDF) is sufficient (instead of directionally dependent BRDF) to represent surface albedo for the irradiance calculation. Since the ocean surface albedo can greatly differ from 0.03 when the Sun is extremely low (Li et al., 2006), we excluded data under low-Sun conditions where the SZA is greater than 45°. Lastly, since EaR^{3}T can only perform 3D simulations for a domain at a single specified solar geometry, we divided each CAMP^{2}Ex research flight into small flight track segments where each segment contains 6 minutes of flight time. The size and shape of the flight track segments can vary significantly due to the aircraft maneuvers, aircraft direction, aircraft speed, etc. For each flight track segment, EaR^{3}T performs irradiance simulations for a domain that extends half a degree at an averaged solar zenith angle. In contrast to the radiance simulation output, which is two-dimensional at a specified altitude and sensor geometry, the irradiance simulation output is three dimensional. In addition to x (longitude) and y (latitude) vectors, it has a vertical dimension along z (altitude). From the simulated three-dimensional irradiance field, the irradiance for the flight track segment is interpolated to the x-y-z location (longitude, latitude, and altitude) of the aircraft. EaR^{3}T automatically sub-divides the flight track into tiles encompassing track segments, and extracts the necessary information from the aircraft navigational data. Based on the aircraft time and position, EaR^{3}T downloads the AHI cloud product that is closest in time and space to the domain containing the flight track segment.

Figure 3.8 shows simulated irradiance for a sample flight track below clouds on 20 September, 2019. Figure 3.8a shows the flight track overlaid on AHI imagery. Figure 3.8b shows 3D (in red) and IPA (in blue) downwelling irradiance simulations for the highlighted flight track in Figure 3.8a, as well as measurements by the SPN-S (in black). Since the 3D and IPA simulations are performed separately at discrete solar and sensor geometries for each flight track segment based on potentially changing cloud fields from one geostationary satellite image to the next, discontinuities in the calculations (indicated by gray dashed lines) are expected. The diffuse irradiance (downwelling and upwelling) can also be simulated and compared with radiometer measurements (not shown here). Since the irradiance was simulated/measured below clouds, high values of downwelling irradiance indicate thin-cloud or cloud-free regions while low values of downwelling irradiance indicate thick-cloud regions. The simulations successfully captured this general behavior – clouds thickened from west to east until around 121.25° E, and thinned eastwards. However, the fine-scale variabilities in irradiance were not captured by the simulations due to the coarse resolution of COT in the AHI cloud product (3-5 km). Additionally, the simulations also missed the clear-sky regions in the very east and west of the flight track as indicated by high downwelling irradiance values measured by SPN-S. This is probably also due to the coarse resolution of the AHI COT product where small cloud gaps are not represented. Large discrepancies between simulations and observations occur in the mid-section of the flight track where clouds are present (e.g., longitude range from 121.15° to 121.3°). Although the 3D calculations differ somewhat from the IPA results, they are both biased high, likely because the input COT (the IPA-retrieved AHI product) is biased low. This bias is caused by the same mechanism that was discussed earlier in the examples from MODIS (Section 3.4.2). This begs the question whether this is true for the entire field mission. To answer the question, we performed a *systematic* comparison of the cloud transmittance for *all* available below-cloud flight tracks from CAMP^{2}Ex, using EaR^{3}T's automated processing pipeline.

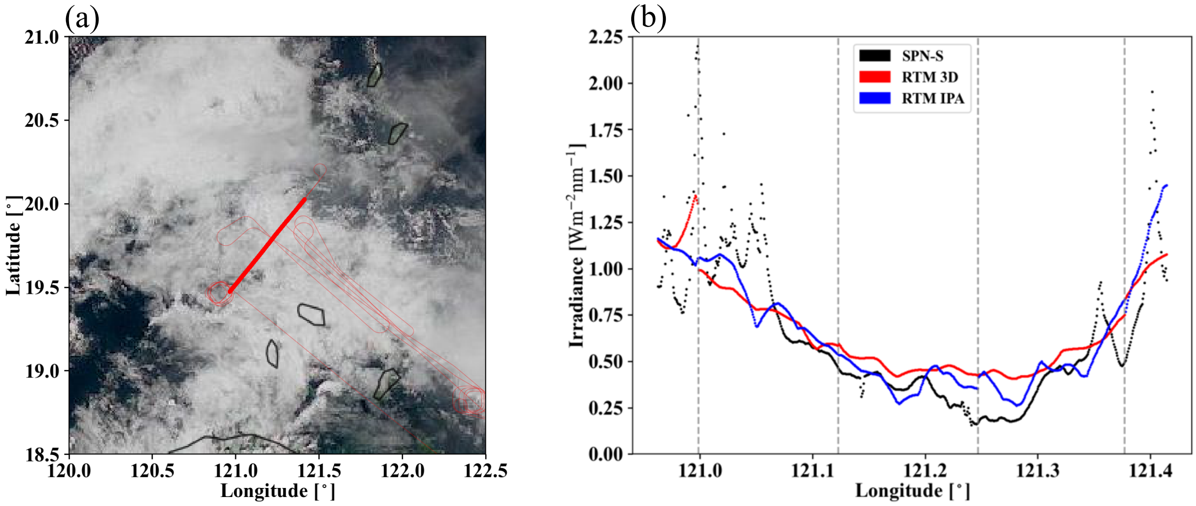

Figure 3.8. **(a)** Flight track overlay HIMAWARI AHI RGB imagery over the Philippine Sea on 20 September, 2019. **(b)** Measured downwelling irradiance from SPN-S at 745 nm and calculated 3D and IPA irradiance from EaR^{3}T for the highlighted flight track in (a).

For this comparison, we use transmittance instead of irradiance because it has less diurnal dependence. The transmittance is calculated by dividing the downwelling irradiance below clouds by the downwelling irradiance at the top of the atmosphere extracted from the Kurucz solar spectra (Kurucz, 1992). Figure 3.9 shows the histograms of the simulated and measured cloud transmittance from all below-cloud legs. The average values are indicated by dashed lines. Although the averaged values of IPA and 3D transmittance are close, their distributions are completely different. Only the 3D calculations and the measured transmittance reach values beyond 1. This occurs in clear-sky regions in the vicinity of clouds that receive photons scattered by the clouds as previously discussed for the OCO-2 application.

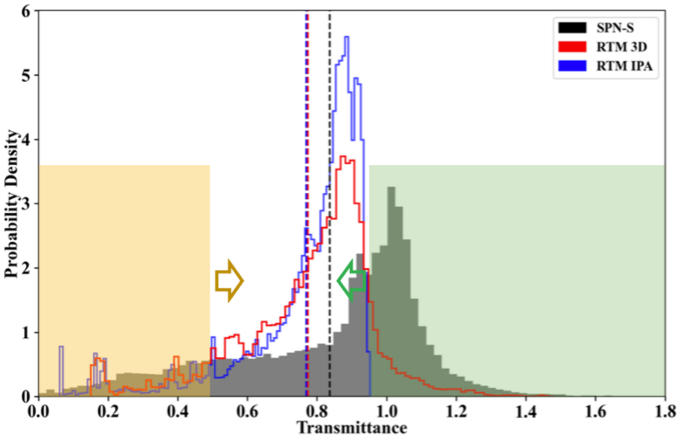

Figure 3.9. Histogram of measured transmittance from SPN-S at 745 nm (black) and calculated 3D (red) and IPA (blue) transmittance from EaR^{3}T for all the below-cloud flight tracks during CAMP^{2}Ex in 2019. The mean values are indicated by dashed lines. The yellow shaded area represents the relatively low transmittance region where the probability density of the observed transmittance (black) is greater than the calculations. Vice versa for the green shaded area.

Both the distribution and the mean value of the simulations are different from the observations – the simulation histogram peaks at around 0.9 while the observation histogram peaks at around 1. The histograms indicate that the RT simulations miss most of the clear-sky conditions because of the coarse resolution of the AHI cloud product. If clouds underfill a pixel, AHI interprets the pixel as cloudy in most cases. This leads to an underestimation of clear-sky regions since cumulus and high cirrus were ubiquitous during CAMP^{2}Ex. The area on the left (highlighted in yellow) has low cloud transmittance associated with thick clouds. In this range, the histograms of the calculations are generally below the observations, and the PDF of the calculations is offset to the right (indicated by the yellow arrow). This means that the transmittance is overestimated by both IPA and 3D RT, and thus that the COT of thick clouds is underestimated, consistent with what we found before (Figure 3.8b). The high-transmittance end (highlighted in green) is associated with clear-sky and thin clouds. Here, the peak of the PDF is shifted to the left (green arrow), and the calculations are biased low. This is caused by a combination of 1) the overestimation in COT of thin clouds due a 3D bias in the AHI IPA retrieval, 2) the aforementioned resolution effect that underestimates the occurrence of clear-sky regions, and 3) net horizontal photon transport from clouds into clear-sky pixels. Overall, the low bias dominates, as is apparent from mean values of the distributions. There is an overall low bias of 10%, and the combined imager resolution and 3D effects do not compensate each other.

Summarizing, this application demonstrates that EaR^{3}T's automation feature allows systematic simulation-to-observation comparisons. If aircraft observations are available, then closure between satellite-derived irradiance and suborbital measurements is a more powerful verification of satellite cloud retrieval products than the radiance consistency from the earlier stand-alone satellite applications. Even more powerful is the new approach to process the data from an entire field mission for assessing the quality of cloud products in a region of interest (in this case, the CAMP^{2}Ex area of operation). We found that the bias between observed and satellite-derived cloud transmittance is partially caused by the coarse imager resolution, and partially by 3D effects, although other retrieval artifacts could also play a role. Although important for future research, it is beyond the scope of this paper to disentangle these effects.

3.6. EaR^{3}T for Mitigating 3D Cloud Retrieval Biases (APP4)

In this section, we will use a high-resolution imagery from a radiometrically calibrated all-sky camera flown during the CAMP^{2}Ex to isolate the 3D bias (sometimes referred to as IPA bias) and explore its mitigation with a newly developed CNN cloud retrieval framework (Nataraja et al., 2022). The CNN, unlike IPA, takes pixel-to-pixel net horizontal photon transport into account. It exploits the spatial context of pixels in cloud radiance imagery, and extracts a higher-dimensional, multi-scale representation of the radiance to retrieve COT fields as the output. It does so by learning on "training data", which in this case was input radiance and COT pairs synthetically generated by EaR^{3}T using LES data from the Sulu Sea. The best CNN model, trained on different coarsened resolutions of the data pairs, is included within the EaR^{3}T repository. For APP4, this CNN is applied to real imagery data for the first time, which in our case are near-nadir observations by the all-sky camera (Section 3.2.2.5) that flew in CAMP^{2}Ex.

The CNN model was trained at a single (fixed) sun-sensor geometry (solar zenith angle, SZA=29.2°; solar azimuth angle, SAA=323.8°, viewing zenith angle, VZA=0º), at a spatial resolution of 100 m. We therefore chose a camera scene with a matching SZA (28.9°), and rotated the radiance imagery to match SAA=323.8°, and subsequently gridded the 8-12 m native resolution camera data to 100 m. Figure 3.10a shows the RGB imagery captured by the all-sky camera over the Philippine Sea at 02:10:06 UTC on 5 October 2019. The Sun is located at the southeast and can be easily identified from the sun glint. Note that this image has not yet been geolocated; it is depicted as acquired in the aircraft reference frame. Figure 3.10b shows the rotated scene of the red channel radiance for the region encircled in yellow in Figure 3.10a. The sun (as indicated by the yellow arrow) is now at SAA=323.8°. Inside a 6.4x6.4 km^2 core area, the 100 m gridded radiance field is shown instead of the native-resolution imagery.

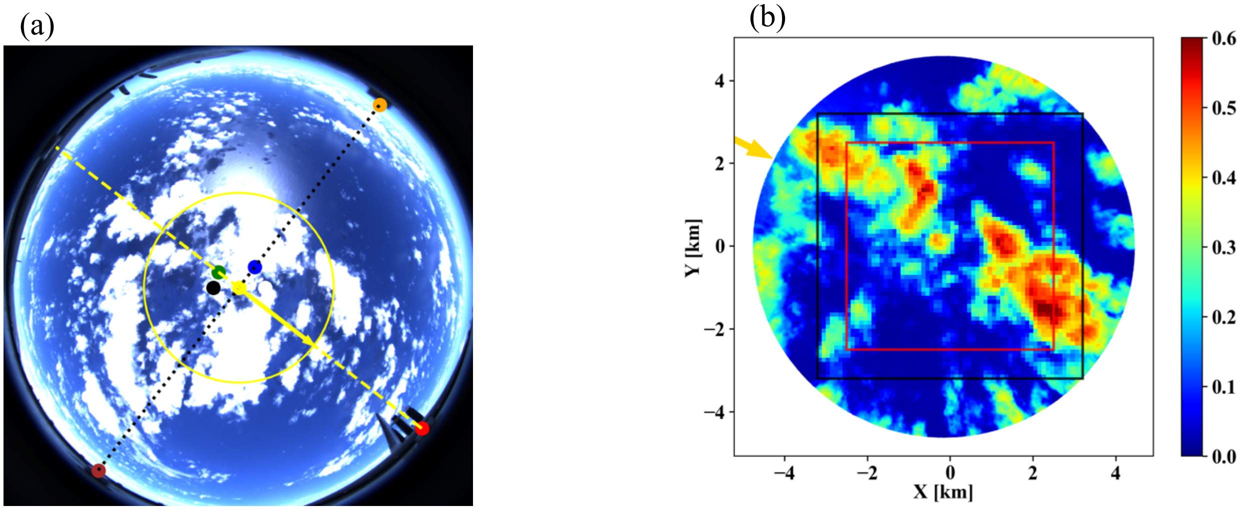

Figure 3.10. **(a)** RGB imagery of nadir-viewing all-sky camera deployed during CAMP^{2}Ex for a cloud scene centered at [123.392°E, 15.2744°N] over the Philippine Sea at 02:10:06 UTC on 5 October, 2019. The lines indicate the axis of the aircraft (yellow) and wing to wing (across, black). The yellow circle shows the approximate field of view that is geolocated for (b); the dots denote various directions from the nadir point. **(b)** Gridded radiance for the square area indicated by solid black lines in (a) with a pixel size of 64x64 and spatial resolution of 100 m. Later for the comparison of COT and RT calculations, only the data from the red square box (50x50) is used. The solar position (azimuth) is indicated by the yellow arrow.

From the radiance field, we used both the traditional IPA (based on the two-stream approximation) and the new CNN to retrieve COT fields. Figure 3.11 shows the $\mathrm{COT}_{\mathrm{IPA}}$ and $\mathrm{COT}_{\mathrm{CNN}}$ fields, which are visually quite different. For relatively thick clouds (e.g., at (x=2, y=22)), the CNN tends to retrieve larger COT values than $\mathrm{COT}_{\mathrm{IPA}}$. Also, it returns more spatial structure than the IPA (e.g., around {2,-1}). To assess how either retrieval performs, we now apply the radiance self-consistency approach introduced with MODIS data in Section 3.4.2. Using both the IPA and the CNN retrieval as input, we had EaR^{3}T calculate the (synthetic) radiance that the camera should have observed if the retrieval were accurate. The clouds are assumed to be located at 1-2 km. Such an assumption is inferred from low-level aircraft observations of clouds on the same day. These radiance fields are shown in Figure 3.12, and can be compared to the red box from Figure 3.10b, which marks a region where 12 edge pixels have been removed from the original domain. This was necessary because the CNN performs poorly at edge pixels, and because the 3D calculations use periodic boundary conditions.

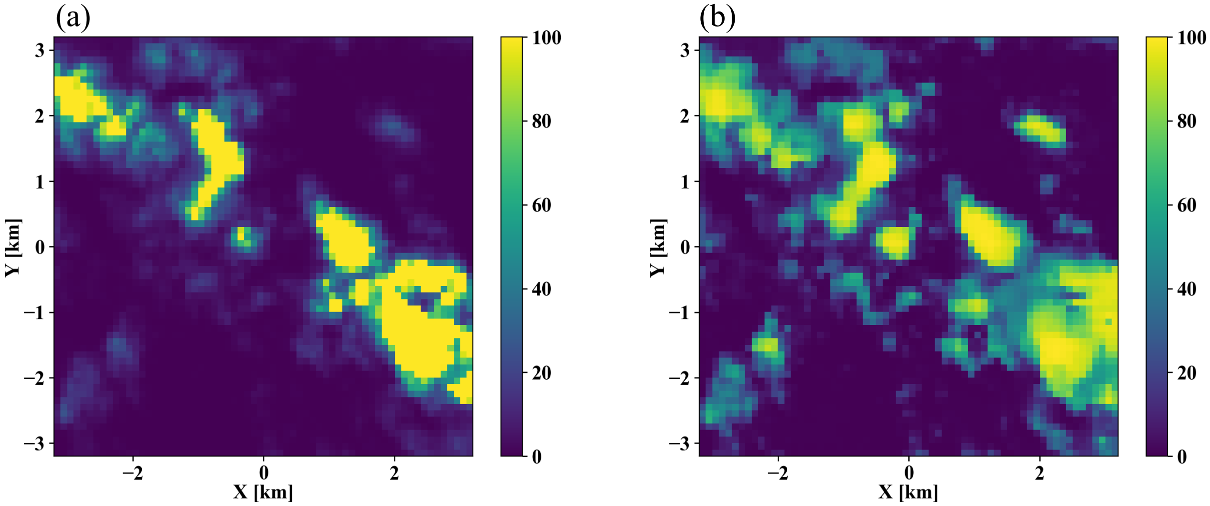

Figure 3.11. Cloud optical thickness for the gridded radiance in Figure 3.10b **(a)** estimated by IPA and **(b)** predicted by CNN.

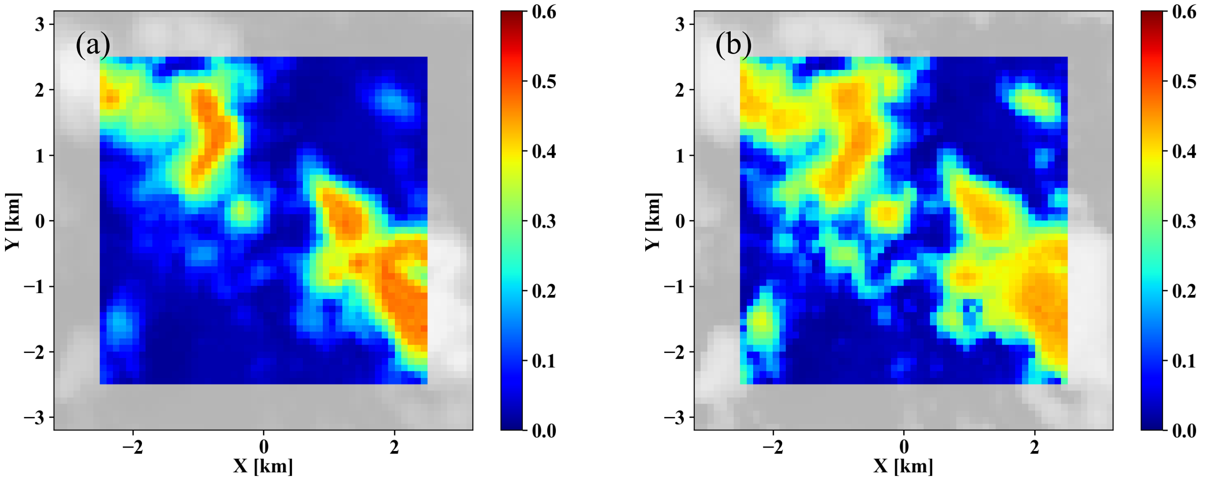

Figure 3.12. 3D radiance calculations from EaR^{3}T at 600 nm based on cloud optical thickness field **(a)** estimated by Two-Stream approximation and **(b)** predicted by the CNN. The calculations were originally performed for

the 64x64 domain. Then 7 pixels along each side of the domain (contoured in gray) were excluded, which resulted in a 50x50 domain.

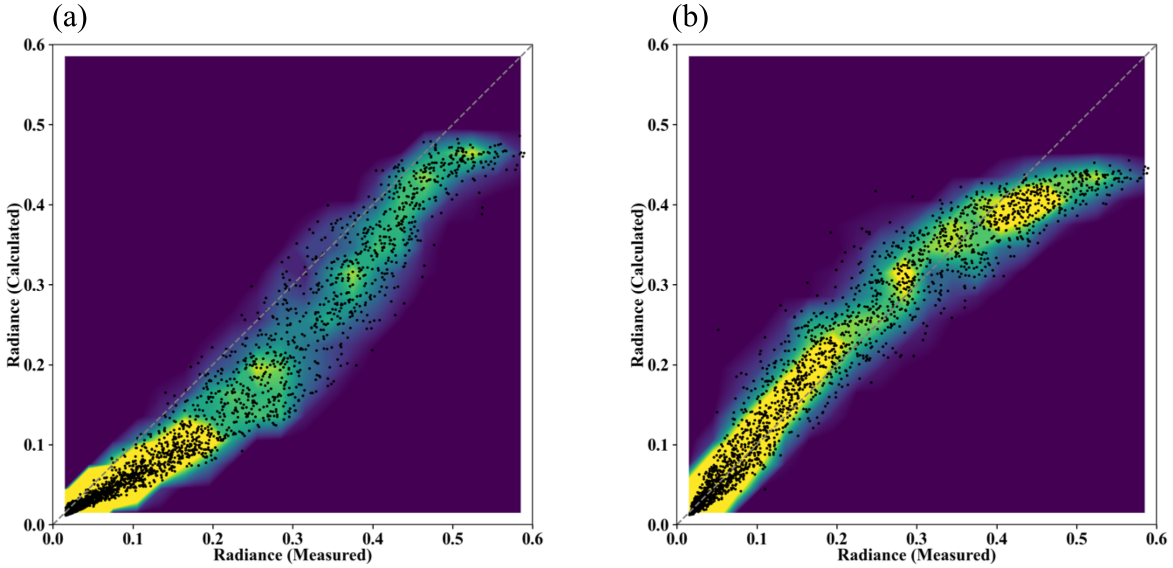

Figure 3.13. Scatter plot overlays 2D histogram of 3D radiance calculations at 600 nm based on cloud optical thickness **(a)** estimated by Two-Stream approximation and **(b)** predicted by the CNN vs. measured red channel radiance from all-sky camera.

As evident from the brightest pixels in Figures 3.12b and 3.10b, the radiances simulated on the basis of the CNN COT input are markedly lower than actually observed by the camera. This is because the CNN was trained on a LES dataset with limited COT range that excluded the largest COT that occurred in practice. This means that the observational data went beyond the original training envelope of the CNN, which highlights the importance of choosing the CNN training data carefully for a given region. In Figure 3.13, the simulations are directly compared with the original observations, confirming that indeed the CNN-generated data are below the observations on the high radiance end. Otherwise, the CNN-generated radiances agree with the observations. By contrast, the IPA-generated data are systematically lower than the observations, over the dynamic range of the COT, which is indicative of the 3D retrieval bias that we discussed earlier. Here again, the self-consistency approach proves useful despite the absence of ground truth data for the COT.

This is extremely helpful because in reality satellite remote sensing does not have the ground truth of COT, whereas radiance measurements are always available. For the CNN, the self-consistency of the radiance is remarkable for the thinner clouds (radiance smaller than 0.4), which encompass 83.5% of the total number of image pixels.

Finally, we use EaR^{3}T to propagate the 3D cloud retrieval bias into the associated bias in estimating the cloud radiative effect from passive imagery retrievals, which means that we are returning from a remote sensing to an energy perspective (irradiance) at the end of the paper. The calculated cloud radiative effects (CRE) of both below-clouds (at the surface) and above-clouds (at 3 km) are shown in Figures 3.14a and 3.14b. The most important histograms are those from 3D irradiance calculations based on the CNN retrievals (black solid line), as this combination would be used in a next-generation framework for deriving CRE from passive remote sensing, and the other would be IPA irradiance calculations based on the IPA retrieval (red solid line), as done in the traditional (heritage) approach. The dashed lines are the other combinations. The mean values (red vs. black) indicate that in our case the traditional approach would lead to a high bias of more than to 25% both at the surface and above clouds. Here again, 3D biases do not cancel each other out in the domain average. If the CNN had better fidelity even for optically thick clouds, the real bias in CRE would be even larger. A minor, but interesting finding is that regardless of which COT retrieval is used, the mean CRE is very similar for IPA and 3D irradiance calculations, even though the PDFs are very dissimilar. By far the largest impact on accuracy comes from the retrieval technique, not from the subsequent CRE calculations. Here again, the self-consistency check turns out as a powerful metric to assess retrieval accuracy. Of course, we only used a single case in this part of the paper. For future evaluation of the CNN versus the IPA, one would need to process larger quantities of data in an automated fashion as done in the first part of the paper. This is beyond the scope of this introductory paper, and will be included in future releases of EaR^{3}T and the CNN.

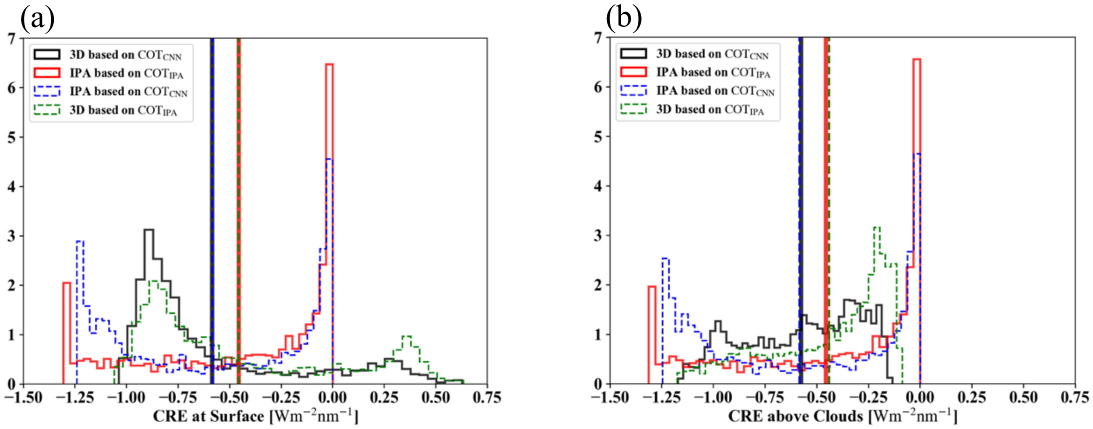

Figure 3.14. Histograms of cloud radiative effects derived from 1) 3D irradiance calculations based on COT_{CNN} (solid black), 2) IPA irradiance calculations based on COT_{IPA} (solid red), 3) IPA irradiance calculations based on COT_{CNN} (dashed blue), and 4) 3D irradiance calculations based on COT_{IPA} (dashed green) both **(a)** at the surface and **(b)** above the clouds. The mean values are indicated by vertical lines.

3.7 Summary and Conclusion

In this paper, we introduced EaR^{3}T, a toolbox that provides high-level interfaces to automate and facilitate 1D- and 3D-RT calculations. We presented applications that used EaR^{3}T to:

a) build a processing pipeline that can automatically simulate 3D radiance fields for satellite instruments (currently OCO-2 and MODIS) from publicly available satellite surface and cloud products at any given time over any specific region;

b) build a processing pipeline that can automatically simulate irradiance along all flight legs of aircraft missions, based on geostationary cloud products;

c) simulate radiance and irradiance for high-resolution COT fields retrieved from an airborne camera, using both a traditional 1D-RT (IPA) approach, and a newly developed 3D-RT (CNN) approach that considers the spatial context of a pixel.

Unlike other satellite simulators that employ 1D-RT, EaR^{3}T is capable of performing the radiance and irradiance calculations in 3D-RT mode. Optionally, it can be turned off to link back to traditional 1D-RT codes, and to calculate 3D perturbations by considering the changes of 3D-RT fields relative to the 1D-RT baseline.

With the processing pipeline under a) (APP1 and APP2, Section 3.4), we prototyped a 3D-RT powered radiance loop that is envisioned for upcoming satellite missions such as EarthCARE and AOS. Retrieved cloud fields (in our case, from MODIS and from an airborne camera) are fed back into a 3D-RT simulation engine to calculate at-sensor radiances, which are then compared with the original measurements. Beyond currently included sensors, others can be added easily, taking advantage of the modular design of EaR^{3}T. This radiance closure loop facilitates the evaluation of passive imagery products, especially under spatially inhomogeneous cloud conditions. The automation of EaR^{3}T permits calculations at any time and over any given region, and statistics can be built by looping over entire orbits as necessary. The concept of radiance consistency could be valuable even for existing imagery datasets because it allows the automated quantification of 3D-RT biases even without ground truth such as airborne irradiance from suborbital activities. In the future it should be possible to include a 3D-RT pipeline such as EaR^{3}T into operational processing of satellite derived data products.

Benefitting from the automation of EaR^{3}T in b) (APP3, Section 3.5), we performed 3D-RT irradiance calculations for the entire CAMP^{2}Ex field campaign, moving well beyond radiation closure case studies, and instead systematically evaluating satellite-derived radiation fields with aircraft data for an entire region. From the comparison based on all below-cloud flight tracks during the entire campaign, we found that the satellite-derived cloud transmittance was biased low by 10% compared to the observations when relying on the heritage satellite cloud product.

From the statistical results of the CAMP^{2}Ex irradiance closure in b), we concluded that the bias between satellite-derived irradiances and the ground truth from aircraft measurements was either due to the coarse spatial resolution of the geostationary imagery products, or caused by 3D-RT effects. To minimize the coarse-resolution part of the bias and thus to isolate the 3D-RT bias, we used high-resolution airborne camera imagery in c) (APP4, Section 3.6), and found that even with increased imager resolution, biases persisted. The at-sensor radiance derived from IPA COT retrievals was inconsistent with the original measurements. For cloudy pixels, the calculated radiance was well below the observations, confirming an overall low bias in IPA COT. This low bias could be largely mitigated with the context-aware CNN developed separately in Nataraja et al. (2022) and included in EaR^{3}T. Of course, this novel technique has limitations. For example, the camera reflectance data went beyond the CNN training envelope, which would need to be extended to larger COT in the future. In addition, the CNN only reproduces two-dimensional clouds fields and does not provide access to the vertical dimension, which will be the next frontier to tackle. Still, the greatly improved radiance consistency from COT_{IPA} to COT_{CNN} indicates that the EaR^{3}T-LES-CNN approach shows great promise for the mitigation of 3D-RT biases associated with heritage cloud retrievals. We also discovered that for this particular case, the CRE calculated from traditional 1D cloud products can introduce a warming bias of at least 25% at the surface and above clouds.

EaR^{3}T has proven to be capable of facilitating 3D-RT calculations for both remote sensing and radiative energy studies. Beyond the applications described in this paper, EaR^{3}T has already been extensively used by a series of on-going research projects such as producing massive 3D-RT calculations as training data for a new generation of CNN models (Nataraja et al., 2022), evaluating 3D cloud radiative effects associated with aerosols (Gristey et al., 2022), creating flight track and satellite track simulations for mission planning etc. More development effort will be invested into EaR^{3}T in the future, with the goals of minimizing the barriers to using 3D-RT calculations, and to promote 3D cloud studies. EaR^{3}T will continue to be an educational tool driven by graduate students. From a research perspective, we anticipate that it will enable the systematic quantification and mitigation of 3D-RT biases of imagery-derived cloud-aerosol radiative effects.

Chapter 4

Diurnal Direct Aerosol Radiative Effects above Clouds and Clear Sky from Aircraft Measurements during ORACLES 2016-2018

4.1 Background

The direct radiative effects of absorbing aerosols have remained a hot topic for decades because of their large uncertainty with respect to their climate forcing (IPCC, 2013). One of the difficulties in quantifying aerosol radiative effects arises when aerosols co-occur with clouds. Clouds act like a moderator of the direct aerosol radiative effects. Whether the absorbing aerosol layer cools or warms the top of the atmosphere (TOA) depends on the underlying scene albedo – a dark surface, e.g., clear-sky over ocean, will lead to a cooling effect while a bright surface, e.g., presence of clouds, may lead to a warming effect at the TOA. In other words, the albedo below an absorbing aerosol layer, can alter the sign of the direct aerosol radiative effects at the TOA (Twomey, 1977; Russell et al., 2002). Aerosols, in turn, can also affect the radiative properties of clouds. The cooling and warming effect of aerosol can induce changes in atmospheric circulation, which will either enhance or reduce cloudiness (Ackerman et al., 2000; Koch and Del Genio, 2010). Additionally, the aerosol particles are important as cloud condensation nuclei. The abundance of aerosol particles affects the cloud droplet size and distributions, resulting in a change in cloud radiative properties such as albedo (Twomey, 1974). The mutual interactions between clouds and aerosols bring large uncertainties in predicting anthropogenic climate forcing, which needs to be better quantified.

The southeast (SE) Atlantic Ocean contributes one third of the total global biomass burning (BB) aerosol (van der Werf et al., 2010), sourced from inland BB in Africa during the southern African burning season from August to October. Since the BB aerosol particles mainly consist of black carbon – the most absorbing atmospheric aerosol constituents, the BB aerosol belongs to one of the main sources of global absorbing aerosol (Bond et al., 2013). Another noteworthy fact about SE Atlantic is that a semi-permanent stratocumulus cloud deck usually underlies the BB aerosol, which makes the SE Atlantic a perfect place on the globe to study cloud and aerosol radiative effects and their interactions.

The need for a better understanding of cloud and aerosol radiative effects and their interactions and the ideal cloud-aerosol environment of SE Atlantic motivated the deployment of the ObseRvations of Aerosols above Clouds and their intEractionS (ORACLES) mission funded by the National Aeronautics and Space Administration (NASA). ORACLES was a 3-year aircraft field campaign during 2016 in Namibia, and 2017 and 2018 in São Tomé and Príncipe to study the aerosol and cloud radiative interactions over the western coast region of Africa. The NASA P-3 and ER-2 aircraft were deployed during ORACLES 2016, while only the P-3 was deployed during ORACLES 2017 and 2018, carrying various remote sensing and in-situ instruments for collecting various cloud and aerosol properties. The details of the instruments and cloud and aerosol retrieval products can be found in the overview of the ORACLES project (Redemann et al., 2021). Figure 4.1 shows various sample flight tracks overlaid on MODIS satellite imagery (one from each year of ORACLES). Various flight maneuvers and sampling techniques were employed during ORACLES. During 2016, the ER-2 and P-3 were aligned to collect measurements of aerosol and cloud properties simultaneously above and below the aerosol layer as shown in Figure 4.1a. For vertical profiling of the aerosol layer, the P-3 regularly performed so-called "square spirals" (red circles in Figure 4.1 – spirals with short straight-and-level segments for every 90º heading change) for measuring localized radiation and in-situ atmospheric profiles. These were used, among other applications, for aerosol optical property retrievals (Cochrane et al., 2019). Finally, extended horizontal legs as well as ramp ascents and descents were performed along so-called routine flight tracks to collect statistics for the climatological study of clouds and aerosols over the SE Atlantic. These routine flight tracks served to collect aircraft measurements for model-observation comparisons (Doherty et al., 2022).

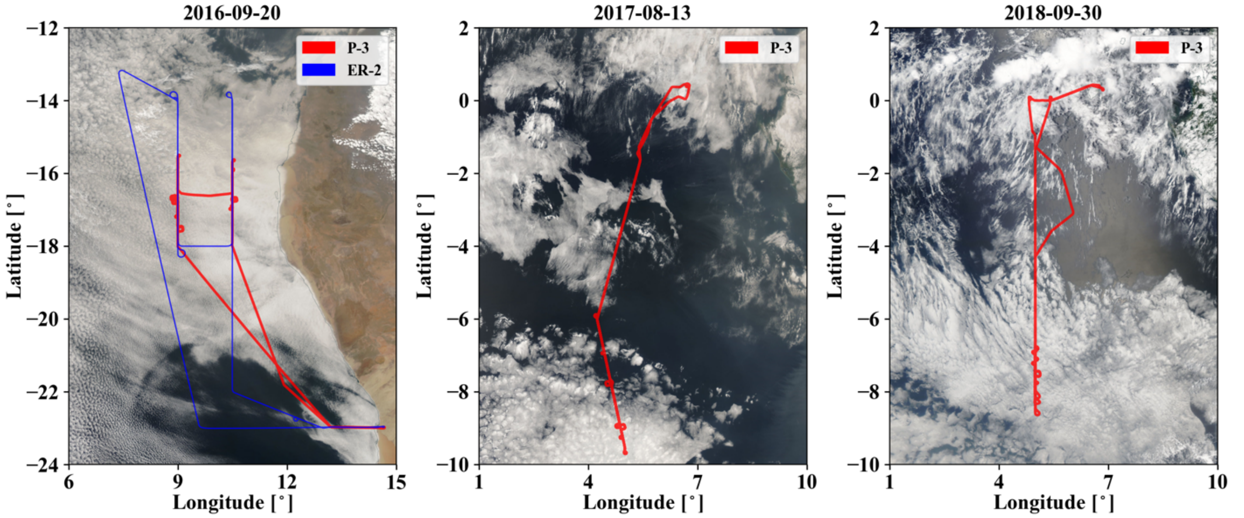

Figure 4.1. ORACLES flight tracks overlaid on MODIS RGB imagery obtained from NASA WorldView for 2016-09-20, 2017-08-13, and 2018-09-30. P-3 and ER-2 flight tracks are indicated in red and blue, respectively.

Four corridors that cover the study region of the horizontal flight tracks (or routine flight tracks) were created for evaluating model estimated direct aerosol radiative effects (DARE) as part of the climatological characterization of the region, as shown in Figure 4.2. They were strategically located to align with the approximate center of the aerosol plume (zonal, green), the transition into the plume, but more importantly the transition from clear sky in the south to stratocumulus in the north. The two meridional ones cut across the plume at different proximity to the land.

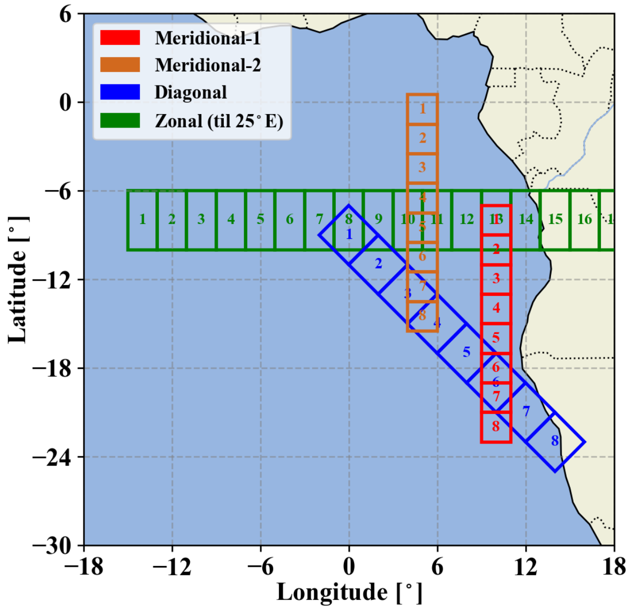

Figure 4.2. Transects used for model-observation comparison for ORACLES 2016 – 2018 region.

From the combined aircraft measurements, DARE can be derived. Cochrane et al. (2021) developed a parameterization (referred to as C21) that provides broadband instantaneous DARE estimates from aerosol optical depth at 550 nm (AOD_{550}), cloud-level albedo at 550 nm (α_{550}), solar zenith angle (SZA), and optionally aerosol single scattering albedo at 550 nm (SSA_{550}). This parameterization is based on the collection of the "square spirals" from the ORACLES campaigns, which provided vertical profiles of spectral net irradiance and AOD measurements, acquired by a spectral airborne radiometer and a spectral sunphotometer (Section 4.2). The parameterization is a generalization of the concept of aerosol radiative forcing efficiency (RFE, Meywerk and Ramanathan, 1999, referred to as radiative effect efficiency here) , which empirically relates the broadband DARE and the AOD_{550} as $DARE = RFE \cdot AOD_{550}$, and can be regarded as an intensive radiative property of the aerosol layer. This is beneficial for generalizing multiple measurements of an air mass where only the AOD varies, whereas other properties such as SSA, asymmetry parameter, or scene albedo remain constant. Equations (3) and (4) in C21 generalize this to:

$$DARE = P(AOD_{550}, \alpha_{550})$$

and

$$DARE = PX(AOD_{550}, \alpha_{550}, SSA_{550})$$

in order to capture the key parameters that explain the variability of DARE during ORACLES beyond the AOD itself. The first parameterization, P, includes the albedo of the underlying scene as an additional input parameter. By including SSA in the second, extended parameterization, PX, the case-specific DARE variability due to varying aerosol optical properties is captured, reducing the uncertainty of DARE in the region if SSA is known. By contrast, the more basic parameterization, P, captures the campaign-averaged dependence of DARE on the primary parameters only; SSA varies too little to drive the DARE variability in the regional average.

While the C21 parameterization provides the translation of simple scene parameters into DARE at any given location, it arrives at the *instantaneous* DARE that is specific to a fixed SZA. In order to make the measurements useable for constraining models statistically, the next steps are to 1) integrate DARE over the course of the day considering the diurnal variability of the scene parameters at a given location, and 2) to use all the measurements from ORACLES collectively to obtain the best estimate of diurnally-averaged DARE throughout the study region – the goal of this chapter. In this way, we will address one of the three main science questions of ORACLES (Redemann et al., 2021):

What is the direct radiative effect of the African biomass burning aerosol layer in clear- and cloudy-sky conditions over the SE Atlantic?

The main challenges are 1) the diurnal integration of the instantaneous DARE since the aircraft only samples a snapshot of the scene parameters that go into C21, and 2) insufficient spatial coverage of the flight tracks to provide us with representative statistics for the entire SE Atlantic. During the course of a day, both the AOD and the underlying clouds, and thus the scene albedo can change, and so does DARE. While the AOD is slowly varying (Chang et al., 2021), the most significant driver of DARE variability are variations of the clouds. The obvious, traditional approach for capturing this variability along with that of the AOD is to use geostationary imagery retrievals of cloud and aerosol properties and validate them with pinpoint aircraft observations where available (Peers et al., 2021). In this case, geostationary imagery is provided by the Spinning Enhanced Visible and InfraRed Imager (SEVIRI) operated by the European Organization for the Exploitation of Meteorological Satellites (EUMETSAT). It provides continuous radiance/reflectance measurements for the ORACLES region every 15 minutes throughout the day. Retrievals of cloud optical thickness (COT) and AOD of the layer above the clouds can be achieved by using multiple wavelengths in the shortwave (Meyer et al., 2015), but this is challenging even with data from polar-orbiting imagers such as the Moderate Resolution Imaging Spectroradiometer (MODIS) and requires a number of assumptions on the optical properties of the aerosol, which are usually fixed. The application of such techniques to geostationary data provides unprecedented temporal coverage as shown in Peers et al. (2021), but is more challenging because of SEVIRI's limited number of channels, coarse spatial resolution, and less rigorous radiometric calibration than available in polar-orbiting imagery.

Nevertheless, although the cloud reflectance measured by SEVIRI is contaminated by the aerosol layer sitting in between the clouds and SEVIRI itself (referred to here as "dimming effect"), the radiance/reflectance observations still contain useful signals associated with the varying cloud properties. Moreover, the magnitude of “dimming effect” as a function of aerosol optical properties, solar zenith angle etc., can be quantified using the aircraft observations. ORACLES, by design, provided a large number of horizontal legs just above the clouds and below the aerosol layer. Therefore, it is possible to link the cloud albedo (as measured by the airborne spectral radiometer) directly to the collocated reflectances from the high spatial resolution mid-visible SEVIRI channel (HRV, Section 4.2), as a function of AOD (also measured directly, by the airborne sunphotometer). This direct link enables a parameterization that maps mid-visible AOD and SEVIRI mid-visible reflectance directly to cloud albedo, bypassing the need for COT retrievals. In this direct pathway to cloud albedo, artifacts such as dimming and cloud variability effects as described in Chang et al. (2021) can be avoided.

In this chapter, we combine the DARE parameterization of C21 with a new parameterization, developed below, that maps SEVIRI reflectance to the scene albedo that the aerosol layer experiences. Furnished with the SEVIRI/aircraft-based cloud albedo parameterization, we can integrate the instantaneous, aircraft-derived DARE to arrive at the diurnally-integrated DARE, filling in cloud albedo information based on satellite data, beyond the time when the aircraft is present in the sample area. The new parameterization, i.e., the mapping of reflectance to albedo is based on the statistics from aircraft and geostationary satellite observations.

We then approach the science question from above by evaluating DARE at different scales – from the small scale of a single flight track segment on a single day to the large scale of select model-observation grid boxes acquired over multiple flight days. This allows us to arrive at observationally based DARE that is minimally affected by assumptions about aerosol optical properties, as opposed to approaches that rely on satellite retrievals of cloud and aerosol properties with subsequent calculations of DARE. By using the whole collection of our observations in the study area, we seek to gain an understanding of the natural variability of DARE, and attribute it to the associated variability of clouds and aerosols.

The aircraft and geostationary satellite instruments and data are described in Section 4.2. The methodology is provided in Section 4.3. The results are shown in Section 4.4 and conclusions are drawn in Section 4.5.

4.2 Instruments and Data

In this study, we use aircraft observations from three airborne instruments: 1) the Solar Spectral Flux Radiometer (SSFR), 2) the Spectrometer for Sky-Scanning, Sun-Tracking Atmospheric Research (4STAR), and 3) the High Spectral Resolution Lidar 2 (HSRL-2) in conjunction with geostationary satellite observations from the Spinning Enhanced Visible and Infrared Imager (SEVIRI). Specifically, SSFR provides directly measured scene albedo at 550 nm (referred to as α_{550}^{SSFR}), 4STAR and HSRL-2 provide measured aerosol optical depth (AOD) at 550 nm (referred to as AOD_{550}^{4STAR} and AOD_{550}^{HSRL}), and SEVIRI provides calibrated reflectance observations at its high-resolution visible (HRV) channel. Our goal is to make the best use of all the available aircraft and geostationary satellite observations to derive DARE that represents the natural variability of aerosols and clouds.

To do that, we manually selected all the aircraft data from the three-year ORACLES mission when the aircraft was flying steadily below the aerosol layer and above the clouds based on the following criteria:

1. Aircraft flies straight and level (pitch, roll<5º), and maintains a low altitude at 1-3 km;

2. Downwelling irradiance at 550 nm is steady at a high value to ensure no cirrus above, and that the aircraft is not inside a cloud.

The selected aircraft data are referred to as the bottom of aerosol layer (BOL) legs. The BOL legs provide key aircraft observations for the systematic TOA SEVIRI reflectance to BOL albedo mapping (Section 4.3). The advantage of BOL is that it provides scene albedo measurements that, unlike satellite observations of clouds with an intervening aerosol layer, have the aerosol effect eliminated. Meanwhile, the AOD measurements from 4STAR can characterize the aerosol layer above, which allows us to build the mapping from SEVIRI TOA reflectance to BOL albedo as a function of AOD loading. The BOL legs are then used to calculate the instantaneous DARE via the C21 parameterization, using SSFR albedo and 4STAR AOD as inputs, whereas the SEVIRI input is used to extend the albedo time series at a given location beyond the sampling time, as discussed above.

To gain more DARE statistics than from the BOL legs alone, we additionally select all the aircraft data when the aircraft was flying steadily *above* the aerosol layer by following the criteria 1-2 except that the aircraft maintains a relatively high altitude at 5-6 km. These high leg aircraft data will be referred to as the top of aerosol layer (TOL) legs and provide AOD measurements from HSRL-2. For these, direct albedo measurements by SSFR are unavailable, and they are therefore generated from SEVIRI. Details of each instrument and data will be described in the following subsections.

4.2.1 SSFR

The SSFR (Pilewskie et al., 2003; Schmidt and Pilewskie, 2012) system consists of a spectrometer box and two light collectors – nadir and zenith. The nadir light collector was fixed mounted at the bottom of the NASA P-3 aircraft. The zenith light collector was mounted on an active leveling platform at the front-top of the aircraft to counteract aircraft attitude in order to be horizontally aligned throughout the flight. The horizontal alignment of the zenith light collector ensures that 1) direct solar radiation can be accurately traced and corrected for the imperfect response of the instrument to the polar incidence angle (Kindel 2010), and 2) no radiance contamination occurs from the lower hemisphere. The two light collectors together provide simultaneous spectral upwelling and downwelling irradiance measurements ranging from 350 nm to 2100 nm, with a spectral resolution of 8 – 12 nm. The details of the instrumentation and data, e.g., calibration procedures, uncertainties of the measurements were described by Cochrane et al. (2019).

From the simultaneously measured upwelling ($F_{\uparrow}$) and downwelling irradiance ($F_{\downarrow}$), albedo (α) can be directly calculated through $\alpha = F_{\uparrow}/F_{\downarrow}$. In this study, only the irradiance measurements at 550 nm from SSFR are used to provide directly measured scene albedo (α_{550}^{SSFR}), the required input parameter for the C21 parameterization. Based on the reported uncertainties of SSFR irradiance measurements (Cochrane et al., 2019), the uncertainty of α_{550}^{SSFR} is estimated to be approximately 2%.

4.2.2 4STAR and HSRL-2

The 4STAR instrument was mounted at the mid-top fuselage of the P-3 aircraft and pointed upward to measure spectral direct solar radiation. The measured radiation covers continuous wavelengths ranging from 350 nm to 1750 nm with a spectral resolution of 2-3 nm below 1000 nm and 3-7 nm above (LeBlanc et al., 2020). The measurements can be used to retrieve column-integrated optical properties of clouds, aerosols, and trace gases above the aircraft (Dunagan et al., 2013). Spectral aerosol optical depth ranges from 350 to 1650 nm is one of the data products provided by the 4STAR team and is publicly available in the ORACLES data archive (Redemann et al., 2021). Several calibration and correction techniques such as a Langley technique (Schmid and Wehrli, 1995), azimuthal correction etc. were applied to achieve an average AOD uncertainty of 0.011 at 500 nm (LeBlanc et al., 2020). Only the AOD at 550 nm from 4STAR is used in this study (AOD_{550}^{4STAR}).

The HSRL-2 is a successor to HSRL-1 from NASA Langley (Hair et al., 2008). It is a lidar system pointing downwards to measure aerosol backscatter and extinction coefficient profile and aerosol depolarization at 355, 532, and 1064 nm (Burton et al., 2018). Originally, the HSRL-2 was designed to be flown on the ER-2 aircraft during ORACLES 2016. Due to the unavailability of ER-2 during ORACLES 2017 and 2018, it was redesigned and mounted on the P-3 aircraft. When the aircraft is flying above the aerosol layer, the column integrated extinction coefficients from HSRL-2 can be used to represent the aerosol layer optical depth. In this study, we used the HSRL-2 measured AOD at 532 nm and scaled to 550 nm (AOD_{550}^{HSRL}) through an assumed AOD versus wavelength relationship with an absorption Ångström exponent of 1.25 for the BB aerosols (Cazorla et al., 2013).

4.2.3 SEVIRI

SEVIRI is the main payload onboard four Meteosat Second Generation (MSG) satellites (Schmetz et al., 2002), which are geostationary weather satellites operated by the European Organization for the Exploitation of Meteorological Satellites (EUMETSAT). The MSG geostationary satellites provide full disc imagery over Europe and Africa every 15 minutes, and rapid scan imagery over Europe every five minutes. In this chapter, we used the calibrated reflectance of SEVIRI from Meteosat-10 (or MSG-3) for ORACLES 2016 and 2017 and from Meteosat-11 (or MSG-4) for ORACLES 2018.

SEVIRI has 3 shortwave and 8 infrared channels with nadir spatial resolution of 3x3 km. In addition, the high-resolution visible (HRV) channel offers an increased spatial resolution of 1x1 km (Cros et al., 2006). The HRV channel has a nominal center wavelength of 750 nm and a relatively broad spectral response compared to other visible bands (Deneke et al., 2021). We use the full disc imagery which has a temporal resolution of 15 minutes. Based on the time and geolocation of the aircraft, we perform collocation to obtain the SEVIRI HRV reflectance that is closest in time and location to the aircraft.

4.3 Methodology – Development of reflectance-to-albedo mapping

In this section, we will show a newly developed parameterization that can provide estimates of diurnally integrated DARE for the ORACLES study region. The key of our parameterization lies in the mapping of geostationary satellite measured reflectance (Ref_{HRV}^{SEVIRI}) onto BOL scene albedo at 550 nm (α_{550}) that is unaffected by the aerosols, which is then used as input for estimating DARE through C21. This mapping goes beyond a traditional atmospheric correction, where at-sensor radiances are corrected for the scattering and absorption effects of the intervening atmosphere, and converted into water-leaving radiances or in our case radiances at the top of the clouds below the aerosol layer. Instead, it also accounts for the angular anisotropy of the radiation that is important to consider when the final product is albedo, rather than reflectance. Previous work has shown that this is best done with empirical parameterizations such as the ones involved for generating the CERES angular distribution models (ADM). In contrast to the ADMs, which provide TOA upwelling broadband irradiances based on a unidirectional at-sensor broadband radiance measurement, our application provides a spectral albedo below the aerosol layer based on at-sensor nadir radiance measurements. Since the Ref_{HRV}^{SEVIRI} is continuously measured by SEVIRI throughout the day, diurnal scene albedo of α_{550}, thus diurnal DARE, can be obtained through the mapping.

Figure 4.3 shows Ref_{HRV}^{SEVIRI} versus α_{550}^{SSFR} for ORACLES 2016 (red), 2017 (blue), and 2018 (green) stratified to select AOD and SZA ranges indicated in each panel figure title. The AOD stems from 4STAR, and the SZA is calculated based on the time and geolocation of the aircraft. The observations indicate a clear relationship between SEVIRI HRV reflectance and scene albedo from SSFR measured below the aerosol layer. More importantly, the relationship can be stratified by AOD and SZA. It should also be pointed out that the data has a significant spread around the functional relationship between the SEVIRI reflectance and the BOL albedo. In part, that is due to the different spatial resolution of the SEVIRI HRV channel (1 km) versus the aircraft observations (hundreds of meters), as stated above. However, since aerosol and cloud properties vary from case to case and from campaign to campaign, some variability is expected even in the absence of this mismatch. In fact, it is remarkable that data points from different cases and years (different colors in Figure 4.3b, for example) are as consistent as they are. For other regions on the globe, the variability of aerosol and cloud properties might prohibit a similar approach.

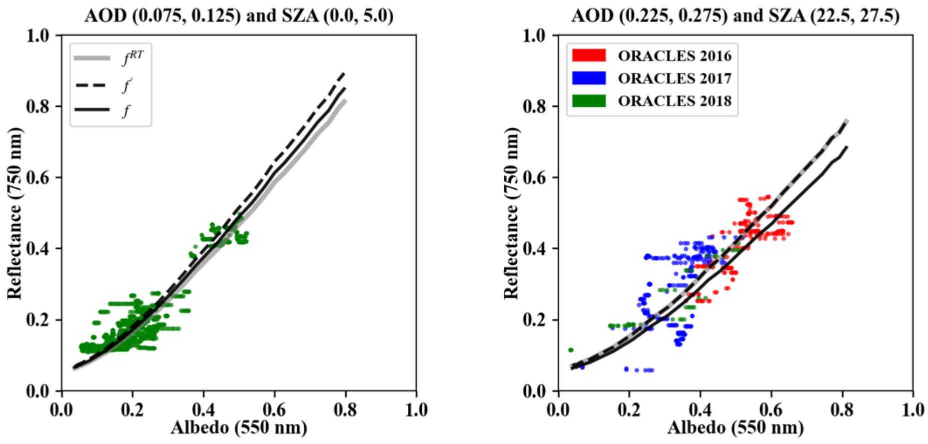

Figure 4.3. Illustration of the modeled albedo-to-reflectance relationship (gray line), the relationship after scaling by scale factor directly obtained from the observations (black dashed line), the relationship after scaling by linear-fitted scale factor (shown in Figure 4.2) for two selected AOD and SZA bins (indicated by each panel figure title). The colored dots are collocated SEVIRI HRV reflectance versus SSFR albedo at 550 nm during ORACLES 2016 (red), 2017 (blue), and 2018 (green).

The general idea behind the mapping is that α_{550} can be expressed as a function of Ref_{HRV}^{SEVIRI}

$$\alpha_{550} = f_{AOD,SZA}(Ref_{HRV}^{SEVIRI}) \tag{4.1}$$

and the function $f_{AOD,SZA}$ can be determined from collocated aircraft and satellite observations. To derive the mapping relationship based on the collocated aircraft and satellite observations, the data were fitted separately for each AOD and SZA bin. We first calculated physics-based fit functions $f_{AOD,SZA}^{RT}$ using RT calculations of nadir reflectance and albedo for a range of COT, indicated by gray curves in Figure 4.3. Those were then rescaled using the observations with a least-square fit. The resulting mapping functions ($f'_{AOD,SZA} = SF_{AOD,SZA} \cdot f_{AOD,SZA}^{RT}$, where $SF_{AOD,SZA}$ is a scale factor) are indicated by the black dashed curves. Finally, a systematic parameterization sf is developed for the scaling factors ($SF_{AOD,SZA}$) to cover the entire AOD and SZA spaces. The final mapping function of $f_{AOD,SZA}$ is shown as black curves in Figure 4.3 and can be expressed by the following equation:

$$f_{AOD,SZA} = sf \cdot f_{AOD,SZA}^{RT} \tag{4.2}$$

4.3.1 Radiative Transfer Calculations

We start by deriving f^{RT} from radiative transfer calculations. The radiance at 750 nm (nominal center wavelength for SEVIRI HRV channel) and the irradiance at 550 nm (wavelength of SSFR albedo) are calculated using EaR^{3}T (Chen et al., 2022) for

- Cloud optical thickness (COT): 0, 0.1, …, 1, 2, …, 10, 12, …, 20, 25, …, 50, 60, …, 100;
- Aerosol optical depth (AOD): 0, 0.05, …, 0.6;
- Solar zenith angle (SZA): 0°, 5°, …, 85°.

For the simulation in this study, we used the Monte Carlo Atmospheric Radiative Transfer Simulator (MCARaTS, Iwabuchi, 2006) as RT solver of EaR^{3}T and set the photon number to 10^8 for each simulation run. We chose a Monte Carlo (MC) RT solver over 1D-RT solver, e.g., DISORT, because the Mie scattering phase functions for the radiance calculations can be used more directly by the MC than is possible with a deterministic RT model such as DISORT (which expands the phase function through a Legendre polynomial expansion). On the other hand, the Mie phase function is fixed to a set a-priori droplet size. The RT details are the following:

1. The atmosphere is set to standard tropical atmosphere (Anderson et al., 1986);
2. The surface albedo is set to 0.03;
3. The cloud layer is located between 1-2 km;
4. Mie phase functions for cloud effective radius of 12μm;
5. The aerosol layer is set to 2-6 km with single scattering albedo of 0.85 and an asymmetry parameter of 0.6 (Dubovik et al., 2002);

The irradiance simulation is done for altitude levels from surface to 20 km (every 1 km). The radiance is simulated at a nadir view (sensor zenith angle of 0°) and at an altitude of 35786 km to simulate what SEVIRI HRV would measure. From the radiance calculations $Rad_{AOD,SZA}{}_{750}^{RT}(COT)$ and $Flux_{AOD,SZA}{}_{550}^{RT}(COT)$, we can obtain the reflectance $Ref_{AOD,SZA}{}_{750}^{RT}(COT)$ and $\alpha_{AOD,SZA}{}_{550}^{RT}(COT)$ (see Appendix 4.A), resulting in $\alpha_{AOD,SZA}{}_{550}^{RT}(COT) = f_{AOD,SZA}^{RT}(Ref_{AOD,SZA}{}_{750}^{RT}(COT))$ as base functions for the physics-based fit.

The RT assumptions are not always exact. For example, a surface albedo of 0.03 is not valid as ocean surface albedo becomes large under low-sun conditions (Li et al., 2006). The SEVIRI viewing angle is not necessarily strictly nadir, depending on the area of observation. However, the main purpose of $f_{AOD,SZA}^{RT}$was to represent the primary angular features (albeit for a fixed microphysical assumption) of the radiance distribution in order to facilitate the radiance to irradiance conversion, whereas the final scaling is accomplished by fitting the observations.

4.3.2 Parameterization

In this subsection, we demonstrate how the final reflectance-to-albedo mapping ($f_{AOD,SZA}$) is developed using $f_{AOD,SZA}^{RT}$ as fit functions, which we have derived in the previous subsection. The general concept has been described at the beginning of this section. To recap, the first step is to select the measurements of α_{550}^{SSFR} and Ref_{HRV}^{SEVIRI} from BOL flight tracks of all three ORACLES campaigns for each AOD and SZA range. Then $f_{AOD,SZA}^{RT}(Ref_{750})$ is scaled based on a least mean squares (LMS) method:

$$f'_{AOD,SZA}(Ref_{750}) = SF_{AOD,SZA} \cdot f_{AOD,SZA}^{RT}(Ref_{750}) \qquad (4.3)$$

Figure 4.4 shows the dependency of the scale factors on SZA. This dependency can be represented as a polynomial regression. The individual observations used for calculating the scale factors are stratified by AOD (colored dots). At a given SZA, there is no systematic dependence of the scale factor on the AOD. That is because the base function $f_{AOD,SZA}^{RT}(Ref_{750})$ already takes the AOD into account. Any variability of $SF_{AOD,SZA}$ is due to case specific variations of properties *other than* AOD and SZA. For example, they can stem from changes in the cloud droplet effective radius assumed in the RT calculations of $f_{AOD,SZA}^{RT}$, the degree of cloud inhomogeneity, or changes in the aerosol SSA.

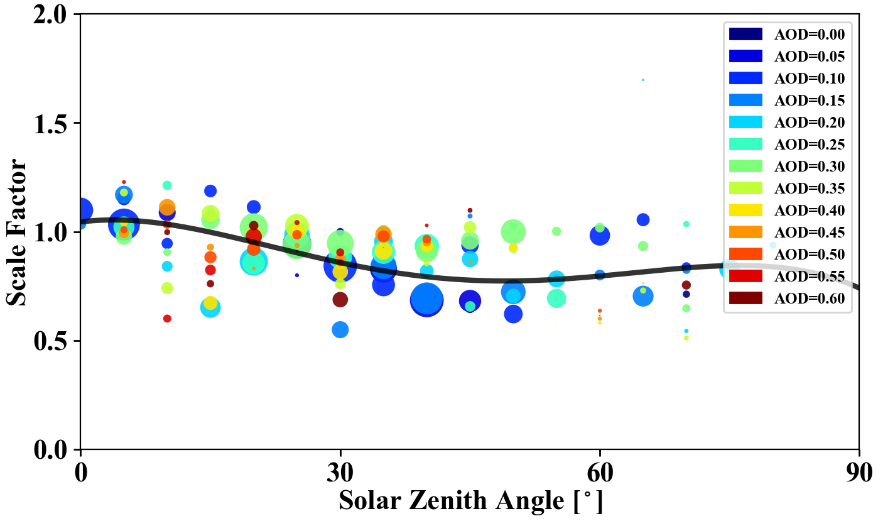

Figure 4.4. Scale factors (concept see previous figure) as a function of SZA. The black line is fitted from all the data through polynomial 4th order fit and represents the general relationship between scale factor and SZA for all different AOD settings. The size of the dots indicates relative abundance of available observations.

The ORACLES *average* conversion from Ref_{750} to α_{550}^{RT} is represented using the polynomial regression line $sf(SZA)$ from Figure 4.4, in conjunction with $f_{AOD,SZA}^{RT}(Ref_{750})$, rather than the individual cases (dots in the same figure), arriving at the final parameterization:

$$f_{AOD,SZA}(Ref_{750}) = sf(SZA) \cdot f_{AOD,SZA}^{RT}(Ref_{750}) \quad (4.4)$$

In the next section, this parameterization will be used to calculate the diurnal albedo from the SEVIRI HRV reflectance, which allows us to turn the instantaneous DARE from Cochrane et al. (2021) into a diurnally dependent DARE, integrate it throughout the day, and calculate it for the entire ORACLES region.

4.4 Results

In this section, we show the diurnal and diurnally integrated DARE obtained through previously described parameterization, which utilizes statistics from aircraft and satellite observations from all three ORACLES campaigns. First, we show how the diurnally dependent DARE is derived for a small BOL flight track segment. Next, we provide the diurnally integrated DARE for the grid boxes of the transects shown in Figure 4.2 that are aggregated to the appropriate scale level for observation-model comparisons. The evaluation of DARE moving from the fine scale of a flight track segment to the large scale of a modeling grid box requires the consideration of natural variability of clouds and aerosols radiative effects at these different scales. As we discuss the results, these considerations will be central.

4.4.1 Diurnal DARE for a Select Flight Track Segment

We use a BOL flight track segment – 08:29:27 to 08:37:32 UTC on October 5, 2018 to illustrate our DARE approach. Figure 4.5a shows the SSFR measured scene albedo (blue dots), SEVIRI HRV reflectance (black), SEVIRI-derived scene albedo (red), and estimated DARE (green) throughout the day. Note that the diurnal dependence of the SEVIRI reflectance is primarily due to changes in the cloud fraction. In the morning and evening, there are fewer clouds than throughout the day. Imagery snapshots of the sample area with the flight track overlaid are shown for three times. The actual SSFR albedo observations are shown together with the albedo obtained from the SEVIRI HRV through our parameterization, at that specific time (first snapshot). The pixel groups at other times correspond to all available HRV observations at the original measurement location. The original measurements occurred relatively early in the day when clouds had not fully developed. The cloud fraction and hence the cloud albedo were still low at this point. In the middle of the day, the albedo increased to around 0.8. The aircraft location within the imagery is shown every 30 seconds (dots in Figure 4.5 1-3 and i-iii). For the first snapshot, the actual albedo measurements are compared with those that are obtained from HRV through the parameterization (Figure 4.6). The comparison indicates that the SEVIRI-derived scene albedo agrees well with SSFR-measured scene albedo, for both clouds and cloud gaps.

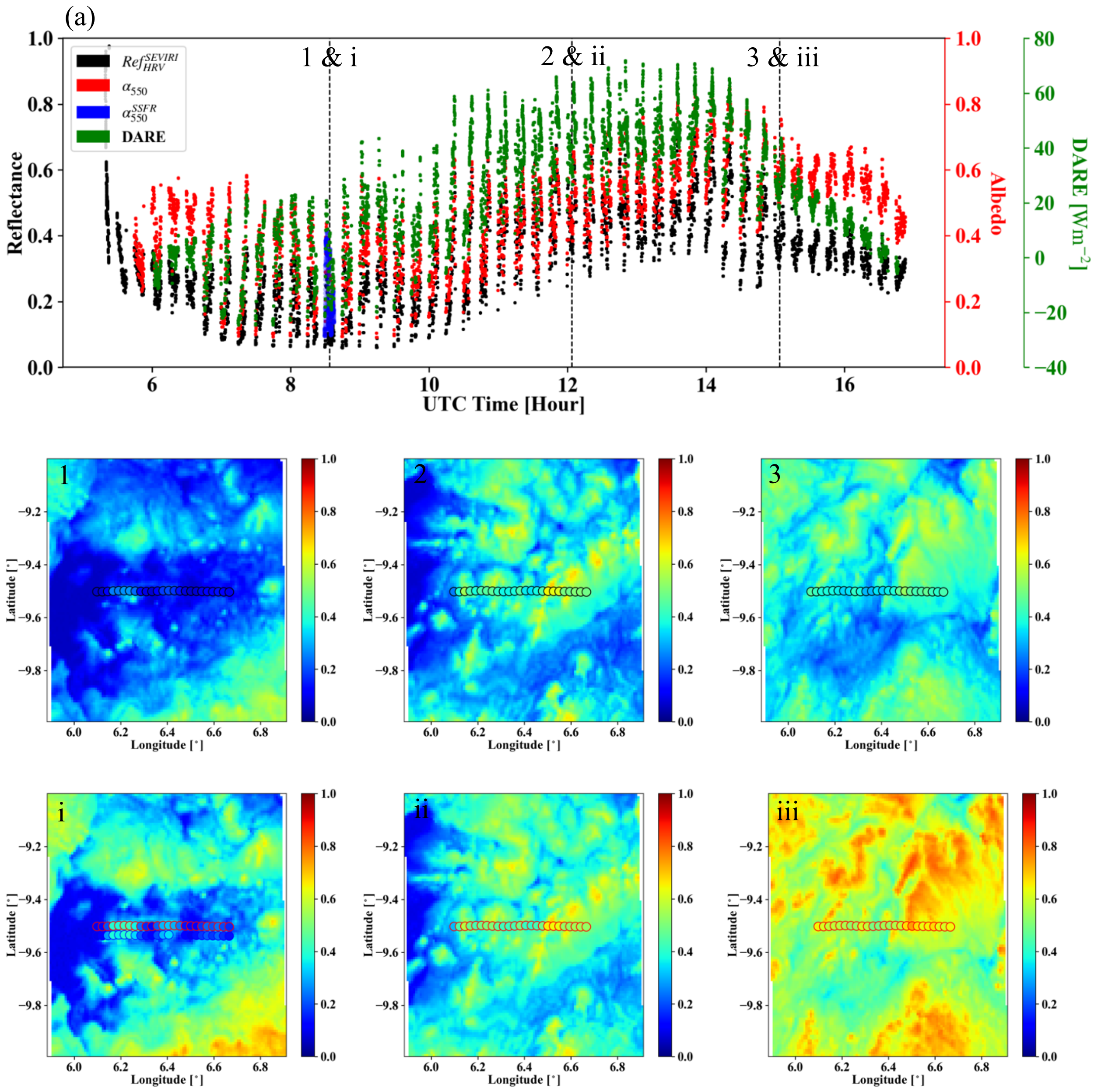

Figure 4.5. **a)** Diurnal reflectance from SEVIRI HRV reflectance (black) sampled at a P-3 below-cloud flight track from 08:29:27 to 08:37:32 UTC on October 5, 2018. The cloud albedo at 550 nm derived from the parameterization is in red, and the DARE derived from C21 is indicated in green. The cloud albedo measured by SSFR is shown in blue. Subplots **1-3** show the SEVRI HRV reflectance domain as well as the collocated SEVIRI HRV reflectance along the flight track (only flight track data of every 30 seconds are shown) at three

times (09:30, 12:00, and 15:00) as indicated by vertical dashed lines in **(a)**. **i-iii** show the associated derived cloud albedo fields. For comparison, **i** also shows the measured albedo from SSFR for the time when the P-3 flew there (offset by –0.035°, blue circles).

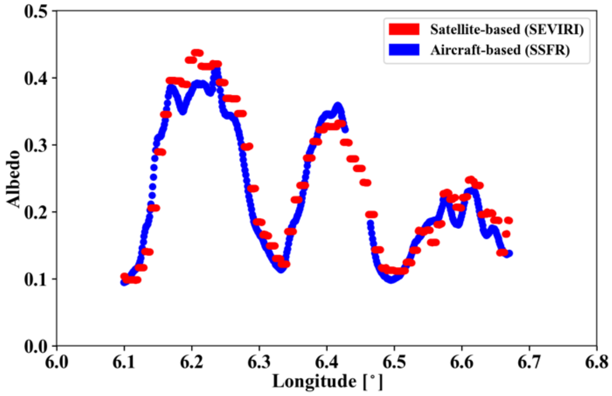

Figure 4.6. Albedo (at 550 nm) derived from SEVIRI HRV reflectance (red) and albedo (at 550 nm) measured by SSFR (blue) at the location of P-3 flight track as indicated in Figure 4.4-i.

There is a slight discrepancy between the HRV reflectance row (1-3) and the derived albedo field row (i-iii) in that the overall reflectance around noon is higher than that around 15 UTC, where the magnitude of albedo does not change much. This is due to the changing SZA, which alters the mapping from reflectance to albedo as shown in Figure 4.4. This illustrates that the satellite reflectance cannot be used blindly as a proxy for the scene albedo. Instead, the SZA and AOD dependent conversion needs to be done in a measurement-supported manner as implemented here. In the time series from (a), the changing relationship between reflectance (black) and albedo (red) is also apparent.

The instantaneous DARE, in turn (green) can now be derived at any given time (even outside of the time of the original observations) from the C21 parameterization. The AOD, obtained from 4STAR, is kept constant over the course of the day, whereas the albedo varies as shown in the figure. This reflects the underlying assumption that the main driver of DARE variability throughout the day is cloud albedo, rather than AOD. Interestingly, there are some times of the day when the cloud albedo is so low that the DARE takes on a negative value.

The cloud imagery in Figure 4.5 1-3 suggests that the variability of the DARE in Figure 4.5a is caused by the inhomogeneities of the cloud fields beneath the flight track. Throughout the day, the albedo ranges from 0.1 to 0.8, whereas the AOD along the sampled flight track varies from 0.22 to 0.25 only, with a mean of 0.24. The true variability of the AOD throughout the day at this specific location is likely somewhat larger than this range, but the cloud variability dominates the DARE variability by far, justifying our approach of pegging AOD throughout the day to the original measurements.

After demonstrating how to obtain the diurnal instantaneous DARE for a specific flight track (referred to as diurnal extension), we will now analyze diurnally-integrated DARE for the ORACLES observation-model grid boxes, in the following subsection. The diurnally-integrated DARE is obtained from the time series of instantaneous DARE by averaging the sum of instantaneous DARE throughout the day (24 hours). For example, the diurnally integrated DARE for the time series in Figure 4.5a ranges from 3.9 to 13.2 W/m^2, with an average of 9.5 W/m^2, whereas the instantaneous DARE from aircraft observations at around 09:30 AM UTC ranges from -21.4 to 20.8 W/m^2, with an average of -2.4 W/m^2. From hereon down, DARE refers to the diurnally integrated quantity. In addition, we will use the diurnally integrated DARE normalized by aerosol loading (mid-visible AOD), which is similar to the REE mentioned above, and will be referred to as radiative effect efficiency (REE).

4.4.2 Statistics for Single Grid Box

We now focus on an entire grid box with multiple samples collected over the course of the ORACLES campaigns. Figure 4.7 shows all flight tracks for grid box 5 in the second meridional stripe from Figure 4.2. In Figure 4.7a, the available BOL samples (circles) and TOL samples (stars) are labeled by flight date in the legend, collected on 14 different days. For the BOL flight tracks, AOD at 550 nm comes from 4STAR. For the TOL flight tracks, it comes from HSRL-2 as explained in Section 4.2.2. Figure 4.7b shows the observations for all the BOL legs, where both AOD and albedo were available from 4STAR and SSFR. Figure 4.7c shows the albedo histogram for those same cases (BOL), whereas Figure 4.7d shows the AOD for both BOL (4STAR) and TOL (HSRL-2) legs. The albedo variability is high, ranging from 0.1 (clear sky) to 0.9 (overcast). By contrast, the AOD does not vary as much; typical values range from 0.1-0.2, although high aerosol loading cases can attain up to 0.6.

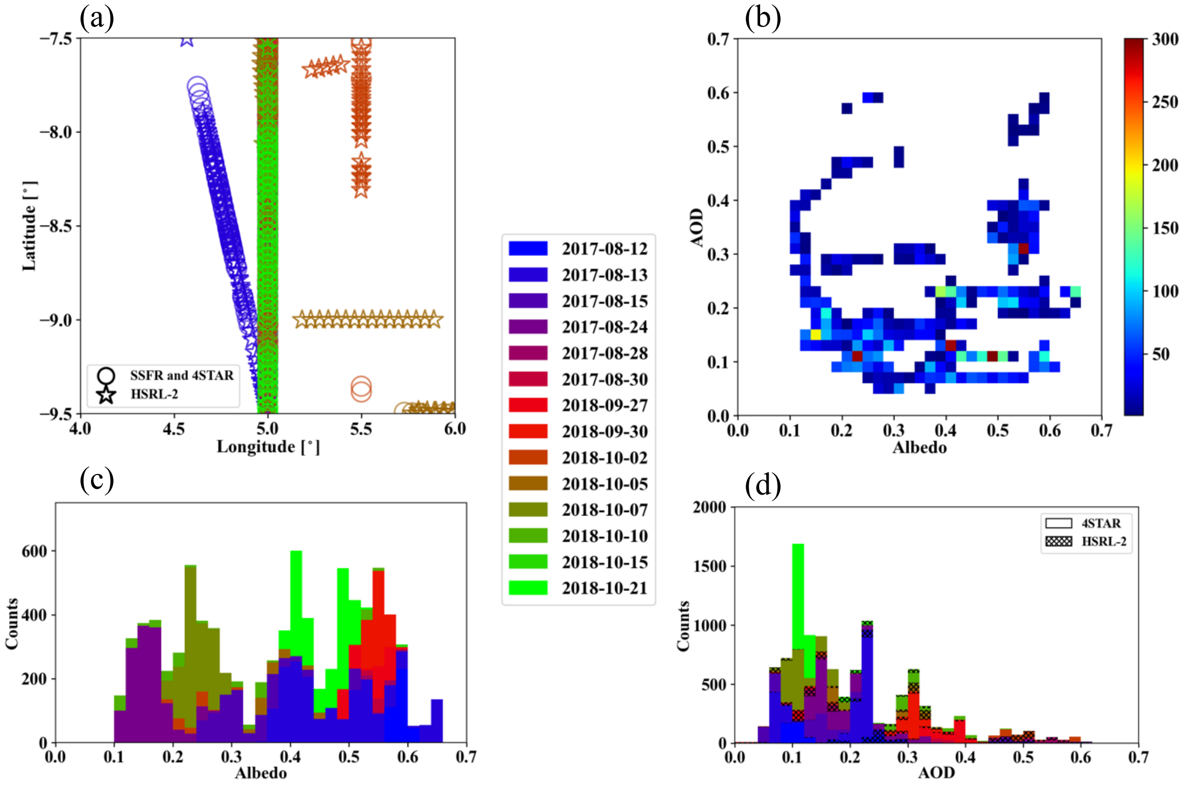

Figure 4.7. **(a)** BOL P-3 locations (dots) and TOL locations (stars) for Meridional-2 grid box 5. **(b)** Heatmap of AOD at 550 nm measured by 4STAR vs. albedo at 550 nm measured by SSFR. **(c)** and **(d)** are histograms for albedo and AOD, respectively. The dates of the flight tracks are indicated by colors shown in the mid-panel legend for (a), (c), and (d).

4.4.3 Diurnally integrated DARE for Single Grid Box

To extrapolate from the instantaneous measurements for grid box 5 of meridional transect 2 from the previous subsection, the albedo for the entire day is obtained from SEVIRI as explained above, whereas AOD is assumed constant. The diurnally integrated DARE for this grid box is then obtained through C21. Figure 4.8 shows the statistics of the DARE and REE as a function of the diurnally averaged albedo. The critical albedo (the point at which the DARE switches from cooling to warming) is 0.3, which is very similar to Cochrane et al. (2021), although their study relates to instantaneous rather than diurnal DARE and albedo. After normalizing the DARE by AOD (radiative forcing efficiency, REE, as introduced above, Figure 4.8b), an almost linear dependence of the instantaneous REE on the scene albedo emerges. It is remarkable that such simple relationships apply even after accounting for the diurnal variability in the cloud conditions, and therefore scene albedo and DARE. Figure 4.8c and d show the histograms of the DARE and REE. Similar to the distribution of scene albedo and AOD, the histograms feature several distinct modes. The variability of the REE (Figure 4.8d) stems primarily from the scene albedo. The mode around -25 W/m^2 is for clear sky, the mode around 50 W/m^2 is for overcast clouds, and the mode around 25 W/m^2 is for partially cloud covered conditions. The DARE histogram itself (Figure 4.8c) is a bit harder to interpret since the aerosol loading affects the location of the peaks as well as the clouds.

Figure 4.8 only shows the DARE corresponding to the BOL samples (4-STAR AOD) from the previous section. However, the plots equivalent to Figure 4.8 from TOL (HSRL-2 AOD) look very similar to BOL, even though the measurements were taken on different days. This corroborates our previous statement that the DARE variability is driven by cloud variability to a much greater extent than by the AOD.

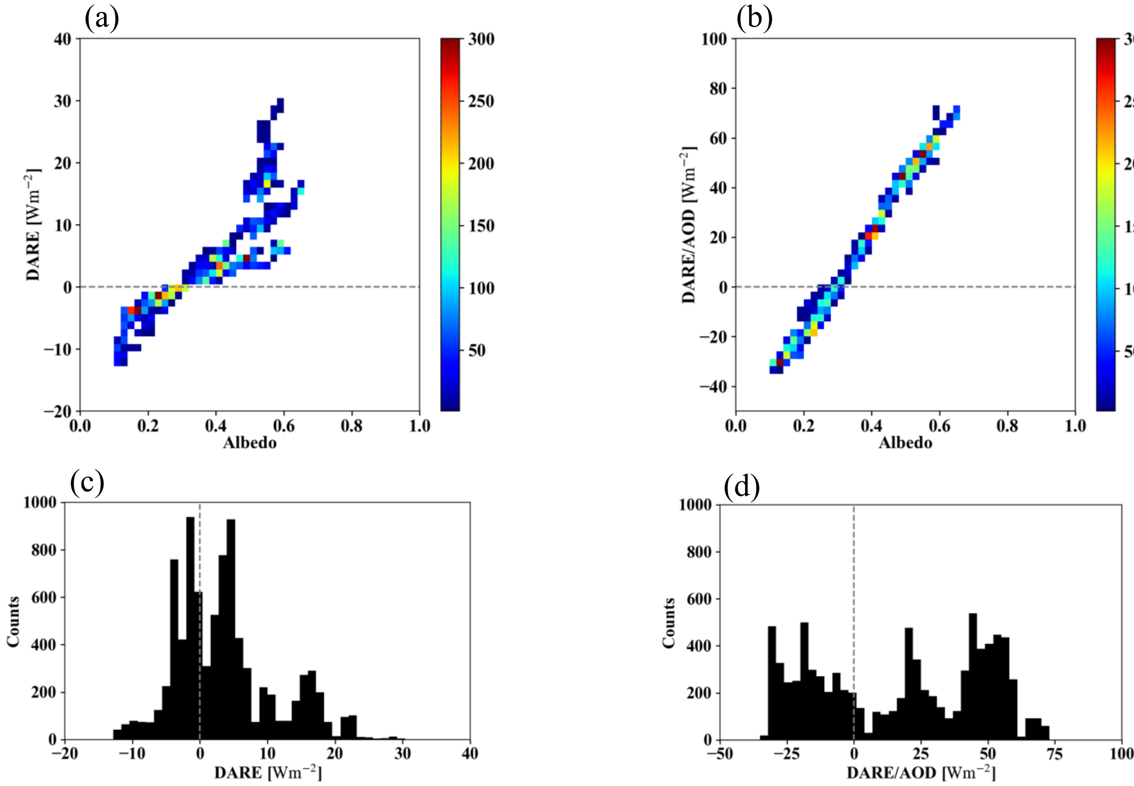

Figure 4.8. **(a)** Heatmap of diurnally integrated DARE vs. diurnally averaged albedo at 550 nm from SEVIRI for the Meridional-2 grid box 5. **(b)** The same as (a) except for diurnally integrated DARE normalized by AOD (REE). **(c)** and **(d)** are histograms for DARE in (a), and DARE normalized by AOD in (b), respectively.

4.4.4 Filled-in Single Grid Box

The specific grid box we focused on earlier was sampled on many days, and therefore the resulting DARE and REE distributions from Figure 4.8 can be regarded as statistically meaningful, even when using only the BOL legs. So far, satellite and aircraft data were combined by using AOD from 4-STAR or HSRL-2 at the specific sampling locations as shown in Figure 4.7a, along with the albedo time series from SEVIRI at those same locations. For less frequently sampled grid boxes, this is too sparse to provide statistically meaningful statistics. Therefore, we developed a second way to combine aircraft and satellite data, based on the joint BOL/TOL (4-STAR/HSRL-2)

AOD observations, and the albedo time series not only at the specific sampling locations, but for *all available* SEVIRI pixels within it. Specifically, this is done by considering all SEVIRI pixels with the associated albedo times series and the AOD measurements from all aircraft samples as independent data pools, which are combined by calculating DARE for each SEVIRI pixel, while randomly assigning AOD from the pool of available data, a kind of Monte Carlo approach. This is computationally more efficient than calculating DARE for each satellite pixel for each AOD sample. To summarize, the SEVIRI data are not only used to temporally extend the albedo time series at a single sampling location, but also spatially beyond the aircraft track into the entire grid box. Filling in the grid box in this manner has the advantage that not only the AOD aircraft observations are used to the fullest extent possible, but also the albedo, which is much more variable than AOD, as noted above.

Figure 4.9 shows the histogram of the DARE and REE of all the flight days for the same grid box as used before. In addition to the spatially filled-in data (labeled satellite-based), the previously shown statistics based solely on aircraft sampling locations (labeled aircraft-based) is also shown for reference. The shape of the aircraft-only and filled-in DARE and REE distributions is similar because the number of sample points was fairly high even before filling in the other grid points. Still, the total number of data points, as indicated by the total count scale, is much higher when including all available satellite data. In terms of mean values (solid lines), the DARE and REE estimates are higher for the filled in method, which is due to a larger occurrence of high albedo in the extended sample.

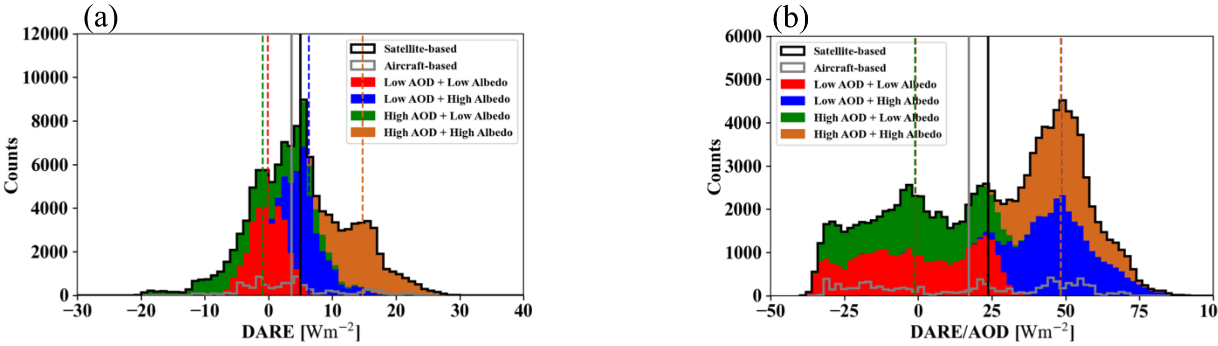

Figure 4.9. **(a)** Histograms of diurnally integrated DARE derived for the whole satellite domain (black) and aircraft flight tracks only (gray) for the Meridional-2 grid box 5. **(b)** The same as (a) except for diurnally integrated DARE normalized by AOD. The DARE derived for the satellite domain are color-coded for four different combinations of high/low AOD and high/low cloud albedo, where the "high" and "low" are above/below the median value. The mean values are indicated by the dashed vertical lines.

To further interpret the results, we divided the DARE and REE into four quadrants of small and large AOD and albedo, as delineated by their median values – indicated by different colors. In Figure 4.9b, high- and low-AOD data lead to the same REE, isolating the impact of cloud albedo on the location of the four modes. For Figure 4.9a, on the other hand, the low- and high-AOD data show very different signatures for the high-albedo segment of the data set, with mean values of 5 and 15 W/m^2, respectively. This illustrates that although cloud albedo is the primary driver of the DARE, the variability of AOD is also significant.

4.4.5 Statistics from a Full Transect

Having demonstrated the two modes of combining aircraft and satellite data for a single grid box, we now apply the analysis to all grid boxes from the meridional transect 2. In addition to the histograms of DARE and REE, Figure 4.10 also includes the distribution of AOD and albedo. For different grid boxes, the number of available flight days differ significantly. That is why the area under the histogram of grid boxes 1, 2, 7, and 8 is smaller than that for grid boxes 3-6. The distribution of DARE and REE are closely related to the distribution of AOD and cloud albedo. For example, grid boxes 2-4 have similar coverage in AOD and albedo, and their REE histograms show a similar location of their peaks. Similarly, grid boxes 7-8 have AOD and albedo centered around 0.35 and 0.5, respectively. Therefore, positive REE and DARE dominate in these boxes. For some grid boxes, the number of flight days was too limited to sample all the modes, leading to a statistically incomplete representation of this area. For example, grid box 8 only contains high aerosol loading and high cloud albedo, and the histograms for the DARE and REE are therefore dominated by a single mode.

In many cases, the green/red and blue/brown dashed lines coincide for the REE because the DARE is normalized by the AOD, and the distinct aerosol loading should therefore not matter. However, this is only the case if aerosol loading and albedo are uncorrelated. In reality, they often are not, as shown in the AOD/albedo heatmaps with the four quadrants of high/low AOD and albedo defined by the dotted lines. Therefore, dividing up AOD/albedo parameter space in this fashion is not necessarily unique, and the different modes need to be interpreted carefully when attributing DARE and REE variability to the underlying causes.

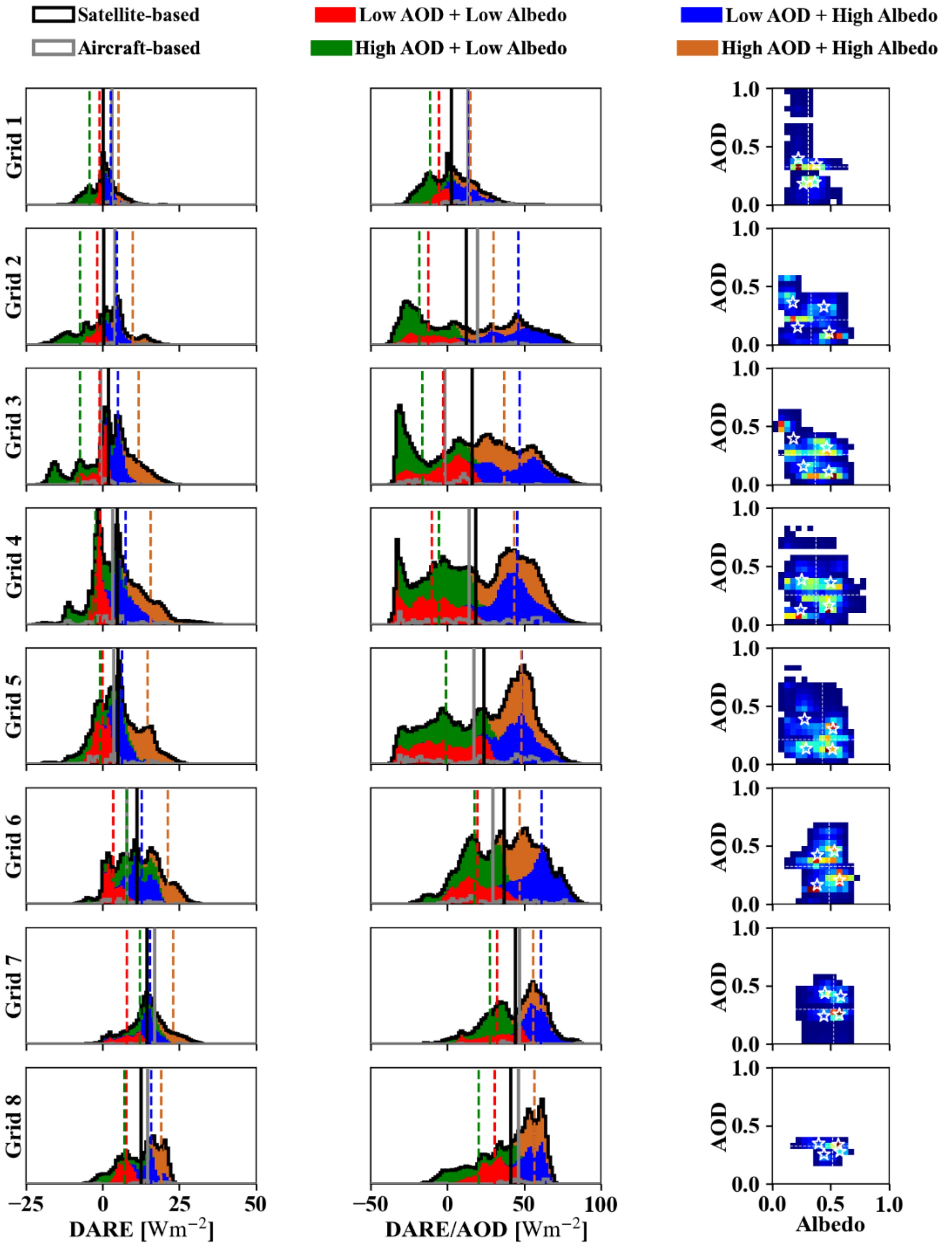

Figure 4.10. The left panel and the mid panel are the same as Figure 4.9 for all the grid boxes of Meridional-2. Additionally, a heatmap of AOD vs. albedo is shown in the right panel for each grid box. The AOD vs. albedo plots are divided into four quadrants. The mean value of AOD vs. albedo of each quadrant is indicated by star marker.

Going further, Figure 4.11 shows the mean values of DARE and REE (location of the black and gray lines from the previous plot), as well as the low- and high-aerosol/albedo subsets (colored lines) as a function of latitude for the whole transect. The horizontal bars are the standard deviations representing the variability.

The aircraft-only results (gray) are only shown for context; the filled-in results (black) can be considered as more statistically significant. Overall, the aerosol has a TOA warming effect for the selected meridional transect as both the aircraft- and satellite-based DARE and REE are greater than 0. To attribute DARE to the most important scene parameters, the latitudinal dependence of averaged AOD and albedo is provided in Figure 4.11c. The scene albedo starts at 0.3 near the equator in the north, which is close to the critical albedo as we discovered in Figure 4.8. Thus, the DARE and REE are close to zero regardless of the aerosol loading. As the scene albedo increases southward, the DARE and REE become more positive. When thin clouds are present (low-albedo), the DARE and REE (red and green) show a closer correlation to the aerosol loading than when it becomes more cloudy (high-albedo, blue and brown). This suggests that the clouds are the main contributor for the variability of DARE and REE. Although aerosol is important as a modulator, its radiative effects are outweighed by the cloud properties. Another interesting finding is that the aircraft-based DARE and REE pick up the latitudinal dependence of aerosol more distinctively than the satellite-based DARE and REE. This indicates that the regional variability of clouds is as important as their diurnal variability. In some regions (for example, at latitudes north of -5º), the variability of the DARE (typically ±10 Wm^{-2} as indicated by horizontal error bars) of the aggregated data set outweighs the DARE itself, and thus suggests that on average, the aerosol has no appreciable radiative effect in the region. By contrast, when stratifying the high aerosol loading data by cloud conditions (via scene albedo), the DARE is distinctly positive (negative) for high (low) albedo, respectively. To a lesser extent, a separation of low/high albedo DARE can also be observed for low aerosol loadings, although it is not statistically significant given the variability as visualized through the horizontal error bars. In any case, the contrast between high- and low-albedo conditions ranges from ±5-10 Wm^{-2}. For reference, the maximum model discrepancy on diurnally averaged DARE from Haywood et al. (2021) is about ±5 Wm^{-2}. A significant share of the model spread is due to the representation of clouds and their diurnal development in various models. Validating and constraining models using the results from our study need to be done both for the aggregated data (black in Fig. 4.11) as well as the stratified data (colored lines). In this way, the discrepancies can be attributed to the underlying causes such as cloud properties, aerosol loading or optical properties. Contrasting DARE, such as warming and cooling in the same location as seen in models, is also seen in our measurements, and is primarily due to clouds.

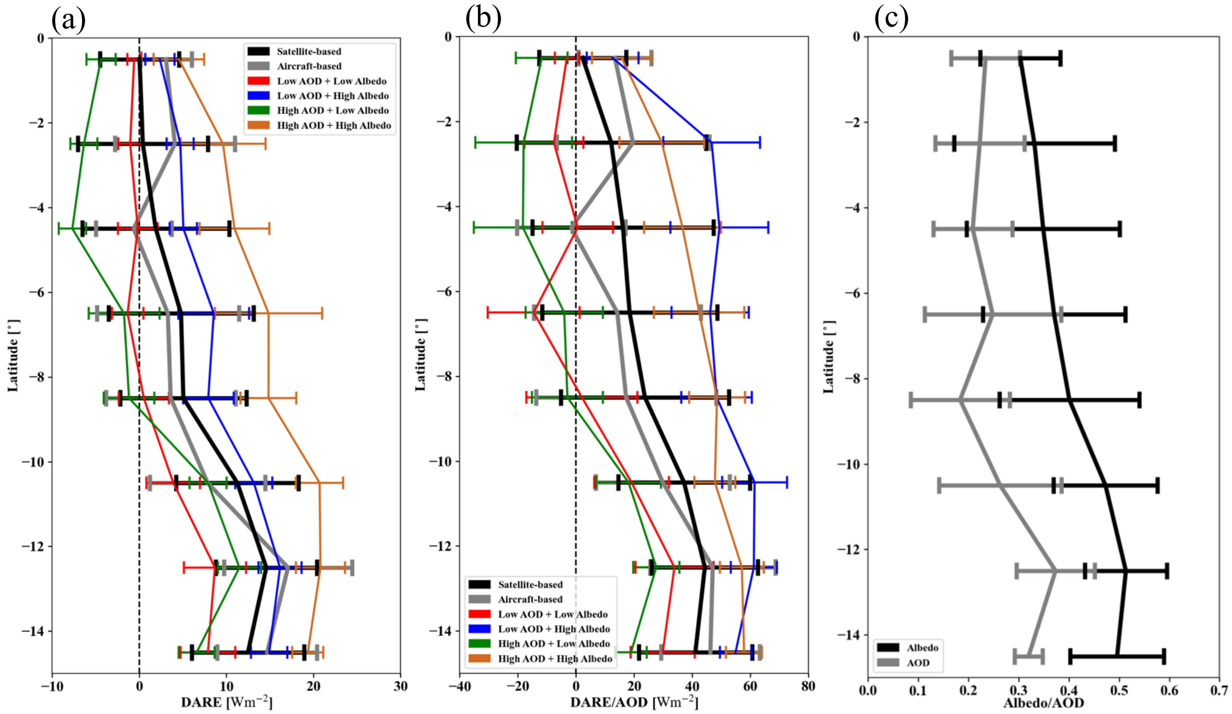

Figure 4.11. Latitudinal trends of averaged **(a)** diurnally integrated DARE, **(b)** diurnally integrated DARE normalized by AOD, and **(c)** averaged scene albedo and AOD for Meridional-2 grid boxes shown in Figure 4.8. The standard deviations are indicated by the vertical error bars.

4.5. Conclusions

In this chapter, we developed a method that can provide diurnal DARE estimates directly from aircraft and satellite observations. This is achieved through a reflectance-to-albedo mapping that translates SEVIRI HRV reflectance, which is continuously measured every 15 minutes throughout the day, into scene albedo at 550 nm below the aerosol layer. The SEVIRI-based diurnal scene albedo obtained from the mapping together with AOD measurements from the aircraft are then input into C21 to get broadband DARE estimates at a given location throughout the day, and those are integrated to provide diurnal DARE. Compared to the traditional DARE approach that performs RT calculations based on satellite and cloud retrievals, our approach is mostly observationally based and provides the DARE estimates closest to the aircraft measurements, with minimal assumptions that are usually entailed in satellite retrieval algorithms. In this way, the errors coming from various assumptions made in the traditional approach can be bypassed, with the caveat that the direct method, developed here, comes with its own uncertainties that lie mainly in the variability of the cloud-aerosol system.

Through the method, we explored the DARE at different temporal and spatial scales – from instantaneous DARE to diurnally integrated DARE, from a single BOL flight track to a collection of BOL flight tracks and to the entire model-observation grid box domain. We demonstrated the reflectance-to-albedo mapping is valid as SEVIRI-derived scene albedo show remarkable agreement with SSFR-measured scene albedo when we perform diurnal extension for a BOL flight track. When aggregating the DARE to a larger spatial scale than provided by the individual aircraft observations, the natural variability of DARE associated with clouds (and to a lesser degree aerosols) became obvious. At the largest aggregation scale, we presented the DARE for a meridional transect consisting of modeling-to-observation comparison grid boxes defined for ORACLES. The results showed a strong latitudinal dependence – from an almost neutral DARE for a region with a scene albedo close to the critical albedo, to a strongly warming effect for a region with higher cloud cover and albedo. By separating the DARE into distinct modes – combinations of high/low scene albedo from clouds and high/low aerosol loading, we found the DARE to be mostly correlated with the scene albedo. Correlations between DARE and AOD are only significant for thin clouds (low scene albedo).

The most significant advantages of our method are 1) it provides diurnally integrated DARE by incorporating the geostationary satellite observations from SEVIRI, thus generalizing instantaneous DARE from aircraft observations only, 2) it can provide DARE for a much more complete study region than aircraft observations alone, 3) it offers direct access to aerosol and cloud properties along with the DARE. Mutually consistent cloud-aerosol properties and CRE/DARE are of key importance for model evaluation since any discrepancies between observed and simulated conditions need to be attributed to specific model processes. Advantage (1) is important as the drastic change of the clouds throughout the day, as shown in Section 4.4.1, can lead to large discrepancies between instantaneous DARE and diurnally integrated DARE, suggesting that instantaneous DARE is not sufficient to represent the DARE. For a solid model-observation intercomparison of DARE, diurnal integration to account for the diurnal cloud variability is required. Advantage (2) allows us to obtain a better understanding of natural variability of DARE at different spatial scales. By integrating the diurnal variation of clouds and extending study region from limited aircraft locations to the entire 2°x2° modeling grid boxes, we clearly see a mitigation of under-sampling bias (aliasing) along with increased natural variability of DARE associated with clouds and aerosols (mostly clouds). Balancing the under-sampling bias and natural variability is important because if natural variability of DARE is large and outweighs the DARE itself, we might lose "resolution" of processes or patterns that are relevant for validating model output. In our case, model-observation comparisons at the 2°x2° scale will fail due to large natural variability, and one needs to fall back on shorter periods of observations or smaller areas of model evaluation. Thus model-observations comparison needs to be performed at certain scales that take the natural variability of the DARE and underlying parameters into account. Advantage (3) allows attribution, e.g., separating DARE into distinct modes, and quantification, e.g., variance analysis, for the natural variability.

In the future, elements of the new, direct approach for obtaining DARE could be combined with the more traditional approach of using satellite observations, and thus get to an optimal DARE characterization in a given region. No matter which approach is used, the issue of optimal data aggregation scale for making modeling-to-observation exercises useful and viable for model development needs to be addressed in detail, in light of natural variability of the system.

Chapter 5

Conclusions

This thesis was motivated by the goal to advance airborne radiation science beyond the selective use of aircraft observations for deriving cloud-aerosol radiative effects. This was done by analyzing large quantities of campaign data to systematically validate satellite-derived cloud and aerosol properties and the associated irradiances and radiative effects, especially for challenging conditions such as thin clouds over bright surfaces, inhomogeneous clouds, and aerosols co-occurring with clouds. The Education and Research 3D Radiative Transfer Toolbox, developed in this thesis, made the transition to this frontier possible. It automatically acquires input data from a variety of user-selectable sources and computes irradiance and radiance fields for entire aircraft flight patterns, satellite orbits, or simulated cloud databases, using a 3D-RT engine to emulate nature, as well as 1D-RT to connect to traditional retrieval algorithms. The initial applications to real-world complex scenes, showcased in the three core chapters (corresponding to three publications), demonstrate that embracing complexity in atmospheric scenes by inclusive data use reveals significant shortcomings of the observational system.

The common thread in all three papers (chapters) of this thesis is the goal to extend the reach of airborne radiation science beyond case studies that are often selected subjectively, and instead use large amounts of field data systematically. In the case of chapter 2, two specific flight patterns were used for answering the science question at hand; in chapter 3, below-cloud observations from an entire mission served to validate satellite-derived cloud transmittance, and in chapter 4 all available aircraft data were combined with satellite imagery to arrive at above-cloud DARE without using imagery retrieval algorithms, thus bypassing the associated assumptions. One general finding was that it is not appropriate to use statistics blindly, which means that the level of data aggregation needs to be tailored to the science question or goals. The level of data aggregation and generalization increase from a few flight legs (chapter 2) to observations and simulations from an entire field campaign (chapter 3) to three field campaigns (chapter 4). Below, we will discuss how this is done given the science question at hand.

The first science question was aimed at evaluating passive satellite imagery cloud retrievals in the Arctic, where the lack of contrast between bright and heterogeneous snow- and ice-covered surfaces and clouds makes the derivation of CRE challenging:

1. *What is the accuracy of satellite imagery-derived cloud radiative effects of thin clouds over ice as sampled during a NASA aircraft campaign in the Arctic?* (Chapter 2)

I addressed this question by validating irradiance calculations based on the best-available passive satellite imagery cloud product for the Arctic with aircraft measurements. This validation was performed satellite pixel by pixel along the flight track for only two flight patterns during the NASA ARISE campaign – one above, and one below a cloud field. Despite the limited amount of data, the collocated observations and simulations showed that even with the best available cloud product, the CRE derived from satellite passive imagery is biased significantly since about a third of the optically thin clouds (cloud optical thickness below 0.5) were not detected. This confirmed findings by Wendisch et al. (2019) from other Arctic field campaigns, which revealed similar underestimation of cloud fraction in satellite imagery products for a larger number of cases. Going beyond cloud detection as the primary error source, the spectral signature in the aircraft measurements also allowed a ranking of the relative importance of secondary errors such as inaccurate surface albedo (largest secondary error contribution in terms of broadband shortwave

CRE), cloud optical properties, and water vapor (smallest error contribution). Interestingly, insufficient or inaccurate knowledge of the surface albedo had a larger impact on the CRE than the cloud optical properties themselves. It should be pointed out that although our study focused on the shortwave CRE, thin clouds can affect the longwave CRE even more strongly as cloud emissivity increases rapidly with liquid water path (Bennartz et al., 2013). This led to the hypothesis that thin clouds may have a net warming effect on the surface that is larger than currently observable by satellites. Along with a number of science questions related to the seasonal Arctic sea ice melt, this motivated the Arctic Radiation-Cloud-Aerosol-Surface-Interaction Experiment (ARCSIX), a planned aircraft field campaign by NASA. One of the key objectives from a remote sensing standpoint will be the development of a spatially variable surface reflectance product. Another will be more robust cloud detection and characterization, which is predicated on improved surface reflectance products.

The second part of the thesis also validated satellite-derived CRE with aircraft observations, but this time in the Tropics, an environment where lack of contrast between clouds and the underlying surface is not the issue. Instead, the most significant challenges are the rapid evolution and spatial complexity of clouds, motivating the second science question:

2. *What is the accuracy of satellite imagery-derived cloud radiative effects of heterogeneous clouds as sampled during a NASA aircraft campaign in the Philippine tropics?* (Chapter 3)

Traditional satellite imagery-derived cloud retrieval algorithms neglect horizontal photon transport, which induces 3D retrieval biases, especially for heterogeneous clouds. 3D biases are difficult to quantify because 1) 3D RT calculations, which are computationally expensive, are required, and 2) they are hard to isolate observationally since clouds often change quickly within an observational time period. To quantify 3D biases, a higher level of statistical aggregation was needed than used for the Arctic, relying on not just selected legs from the flight campaign (CAMP^{2}Ex), but from the collection of all legs. Capitalizing on the automation capability of EaR^{3}T, 3D irradiance calculations were performed for all the below-cloud flight tracks, using heritage cloud retrievals from a geostationary satellite in the region (AHI). The satellite-derived irradiance (and by extension, CRE) were then compared with the measured truth, obtained from aircraft observations. This showed that in the campaign average of the region, the cloud transmittance calculated from satellite imagery was low-biased by 10% due to a combination of 3D biases and coarse imagery resolution effects. This result is statistically robust, unlike in previous studies with a limited data pool. We found that retrieval biases due to cloud spatial inhomogeneity cannot be fully mitigated by averaging, nor can the resulting 10% low bias in cloud transmittance. This finding, valid for a specific region in the Tropics, evokes the question of whether similar biases occur throughout the Tropics, or even globally. If this were the case, global surface radiation budget assessments would need to be revised, with downstream repercussions on the water cycle. The work started in this thesis is only the beginning to explore this question.

While the high level of data aggregation allowed us to quantify the overall bias, it did not allow us to disentangle two potential error sources – the coarse imager resolution and 3D effects. To do this, we used high-resolution airborne imagery, which minimizes resolution biases, leaving 3D retrieval biases as the only source of error. We then applied two different types of retrievals: the heritage 1D retrieval where pixels are treated independently in the radiative transfer (independent pixel approximation, IPA), and a novel machine learning technique that is context-aware and accounts for net horizontal photon transport from pixel to pixel – the newly developed Convolutional Neural Network (CNN) retrieval framework (Nataraja et al., 2022).

The challenge in using machine learning in practice, that is, for operational retrievals, is the perception that any machine learning algorithm is “only as good as the training data”. This concern was addressed in this thesis by developing a metric, the so-called radiance self-consistency, that objectively quantifies the performance of any algorithm with respect to 3D effects. In this way, even our machine learning algorithm could be placed on a physical foundation. The concept treats the radiance measurements, rather than the cloud retrievals, as the “ground truth”. The cloud retrievals (from any algorithm) are hereby taken at face value, and the radiances that the imager *should* observe if they were accurate are calculated. Closure between these calculations and the original radiance measurements can then be regarded as a proxy for the accuracy of the cloud retrieval. Key is that the calculations emulate nature, and are therefore performed with 3D-RT. If the calculated radiances are consistent with the original measurements, then they are called self-consistent with respect to the retrieval that was generated from them. Any inconsistencies, on the other hand, serve as a metric for the infidelity of the cloud retrieval algorithm. It should be noted that while radiance self-consistency is a necessary condition for the retrieval to be accurate, it is not necessarily a sufficient condition. In-situ observations of clouds will always be the most stringent evaluation of remote sensing products. However, radiance self-consistency can be regarded as the first step when in-situ validation is unavailable.

Summarizing, chapter 3 went further than answering the science question that initially motivated it. Instead of merely quantifying imagery retrieval biases due to cloud spatial inhomogeneity, it explored avenues for the mitigation of these biases. For the first time, CNN were applied to real-word imagery. The 3D retrieval biases were significantly decreased by the CNN, as evidenced in better radiance self-consistency than for the traditional IPA retrievals throughout almost the entire dynamic range of optical thickness. However, radiance inconsistencies at the high end of the dynamic range also showed that the CNN performed poorly on clouds with large optical thicknesses. This was because this particular CNN was trained on synthetic data with low optical thickness, which never attained the high values that were encountered in reality, emphasizing the importance of remaining within the original training envelope of a given machine learning algorithm, and calling for the kinds of consistency checks that were developed in the thesis to automatically identify unrealistic retrievals.

In chapters 2 and 3, the accuracy of radiative effects derived from satellite observations was quantified by validating them with aircraft observations, using varying degrees of statistical aggregation. Fundamentally, this type of work aims at improving our knowledge of climate system parameters by using satellite and aircraft observations jointly. Indeed, it triggered the development of mitigation strategies for persistent imagery retrieval biases. In chapter 4, however, the goal was to combine satellite and aircraft observations more directly, with minimal reliance on satellite cloud or aerosol retrievals:

3. *How can detailed, accurate aircraft observations be combined with spatially and temporally extended satellite imagery to obtain the best estimate of the direct aerosol radiative effect for the study region of a set of NASA campaigns in the southeast Atlantic?* (Chapter 4)

The background for this question was the wide range of top-of-atmosphere DARE estimates from a variety of models for the southeast Atlantic, as documented by, e.g., Zuidema et al. (2016) and Haywood et al. (2021, Figure 2). For some locations, certain models predicted a warming effect where others predicted cooling by the aerosol. Since satellite observations alone could not sufficiently constrain models, they needed to be augmented by aircraft observations such as the ones from the NASA ORACLES campaigns described in chapter 4.

For this data set, Cochrane et al. (2021) previously developed a DARE parameterization (referred to as C21) that can provide DARE estimates at a given location with minimal assumptions. C21 requires scene albedo and aerosol properties as inputs. With aircraft observations at a given location, only the instantaneous DARE can be obtained through C21, whereas modeling studies need to be constrained with diurnally integrated DARE for an entire study region. To extrapolate from the spatially and temporally limited aircraft observations to the full day, and well as to a larger region, radiance observations from geostationary imagery were incorporated as described in chapter 4. Specifically, a reflectance-to-albedo mapping was developed based on the statistical relationship between satellite measured reflectance and collocated aircraft albedo measurements during all ORACLES campaigns. This mapping provides the scene albedo input for the C21 parameterization directly from the geostationary satellite reflectance throughout the day. The resulting instantaneous DARE is subsequently diurnally integrated. Summarizing, the aircraft observations provide (1) the relationship between scene albedo, aerosol properties and instantaneous DARE (C21 parameterization) and (2) the mapping from satellite reflectance to scene albedo at a range of specific times and aerosol loadings, whereas the satellite observations provide the scene albedo at any time (from the measured reflectance via the empirical mapping to albedo).

Assuming that the aerosol loading varied negligibly compared to scene albedo (i.e., cloud properties) throughout the day and within a 2°×2° grid box, the aircraft and satellite observations were combined to estimate the local DARE, with a smaller range of variability than the model spread of the DARE for most locations. This means that the observations do indeed provide new constraints to the models. However, in some locations the natural variability of cloud and aerosol properties was so large that the available aircraft samples may have been insufficient to capture it, leading to aliasing. This shows the limitations of aircraft-based observations. Direct validation of model estimates with merged aircraft-satellite observations is therefore only possible for regions with moderate natural variability. In the future, sampling strategies could be developed that take the periodicity of natural patterns explicitly into account.

In conclusion: by exploring three science questions with joint aircraft-satellite observations, it was possible to gain a differentiated understanding of "statistics" for quantifying cloud and aerosol radiative effects under challenging conditions. The tool developed in the process – EaR^{3}T in Chapter 3 – filled a gap in understanding atmospheric radiation in the real world, which is three-, and not one-dimensional. Beyond this thesis, EaR^{3}T has been used to study cloud-aerosol radiative effects (Gristey et al., 2010a, 2010b, 2022), and to produce extensive synthetic data for training machine learning cloud retrievals (Nataraja et al. 2022).

Satellite-derived CRE was validated against aircraft observations in two different climate regions, the Arctic and the Tropics. In both cases, significant biases were uncovered – for different reasons: undetected clouds and cloud spatial inhomogeneity, respectively. On the one hand, this led to the question whether the discovered bias patterns occur more widely than in the specific regions studied here. On the other, avenues for bias mitigation were proposed and tested.

The science questions addressed in this thesis, along with other studies enabled by the development of EaR^{3}T, are only the beginning of a transition towards fully embracing the complexity of atmospheric radiation in the real world. The various examples for approaching complex aircraft data in radiation science discussed here can guide the development of solutions for resolving some of the biases associated with assumptions and oversimplifications in traditional retrieval algorithms, and thus facilitate the transition from bias quantification to bias mitigation.

Bibliography

Anderson, G. P., Clough, S. A., Kneizys, F. X., Chetwynd, J. H., and Shettle, E. P.: AFGL atmospheric constituent profiles (0–120 km), Tech. Rep. AFGL-TR-86–0110, Air Force Geophys. Lab., Hanscom Air Force Base, Bedford, Massachusetts, U.S.A., 1986.

Ackerman, A. S., Toon, O. B., Stevens, D. E., Heymsfield, A. J., Ramanathan, V., and Welton, E. J.: Reduction of tropical cloudiness by soot, Science, 288, 1042–1047, 2000.

Badosa, J., Wood, J., Blanc, P., Long, C. N., Vuilleumier, L., Demengel, D., and Haeffelin, M.: Solar irradiances measured using SPN1 radiometers: Uncertainties and clues for development, Atmos. Meas. Tech., 7(12), 4267–4283, doi:10.5194/amt-7-4267-2014, 2014.

Bannehr, L., and Schwiesow, R.: A technique to account for the misalignment of pyranometers installed on aircraft, J. Atmos. Ocean. Tech., 10, 774–777, 1993.

Barker, H. and Liu, D.: Inferring optical depth of broken clouds from Landsat data, J. Climate, 8, 2620–2630, 1995.

Barker, H. W., Jerg, M. P., Wehr, T., Kato, S., Donovan, D. P., and Hogan, R. J.: A 3D cloud construction algorithm for the EarthCARE satellite mission, Q. J. Roy. Meteor. Soc., 137, 1042– 1058, https://doi.org/10.1002/qj.824, 2011.

Barker, H. W., Kato, S., and Wehr, T.: Computation of solar radiative fluxes by 1-D and 3-D methods using cloudy atmospheres inferred from A-train satellite data, Surv. Geophys., 33, 657–676, 2012.

Bennartz, R., Shupe, M. D., Turner, D. D., Walden, V. P., Steffen, K., Cox, C. J., Kulie, . S., Miller, N.B., and Pettersen, C.: July 2012 Greenland melt extent enhanced by low-level liquid clouds. Nature, 496, 83–86, 2013.

Boggs, P. T. and Rogers J. E.: Orthogonal distance regression. Contemporary Mathematics, 112, 183-94, 1990.

Bond, T. C., Doherty, S. J., Fahey, D. W., Forster, P. M. Berntsen, T., DeAngelo, B. J., Flanner, M. G., Ghan, S., Kärcher, B., Koch, D., Kinne, S., Kondo, Y., Quinn, P. K., Sarofim, M. C., Schultz, M. G., Schulz, M., Venkataraman, C., Zhang, H., Zhang S., Bellouin, N., Guttikunda, S. K., Hopke, P. K., Jacobson, M. Z., Kaiser, J. W., Klimont, Z., Lohmann, U., Schwarz, J. P., Shindell, D., Storelvmo, T., Warren, S. G., and Zender, C. S.: Bounding the role of black carbon in the climate system: A scientific assessment, J. Geophys. Res.-Atmos., 118, 5380–5552, https://doi.org/10.1002/jgrd.50171, 2013.

Bosilovich, M., Akella, S., Coy, L., Cullather, R., Draper, C., Gelaro, R., Kovach, R., Liu, Q., Molod, A., Norris, P., Wargan, K., Chao, W., Reichle, R., Takacs, L., Vikhliaev, Y., Bloom, S., Collow, A., Firth, S., Labow, G., Partyka, G., Pawson, S., Reale, O., Schubert, S. D., and

Suarez, M: MERRA-2: Initial evaluation of the climate. NASA Tech. Rep. Series on Global Modeling and Data Assimilation NASA/TM-2015-104606, 2015.

Brandt, R. E., Warren, S. G., Worby, A. P., and Grenfell, T. C.: Surface albedo of the Antarctic sea ice zone, J. Climate, 18, 3606–3622, 2005.

Bucholtz, A., Bluth, R. T., Kelly, B., Taylor, S., Batson, K., Sarto, A. W., Tooman, T P., and McCoy, Jr., R. F.: The Stabilized Radiometer Platform (STRAP) – An actively stabilized horizontally level platform for improved aircraft irradiance measurements, J. Atmos. Ocean. Tech, 25, 2161–2175, 2008.

Bucholtz, A., Hlavka, D. L., McGill, M. J., Schmidt, K. S., Pilewskie, P., Davis, S. M., Reid, E. A., and Walker, A. L.: Directly Measured Heating Rates of a Tropical Subvisible Cirrus Cloud, J. of Geophys. Res., 115, 1-11, 2010.

Burton, S. P., Hostetler, C. A., Cook, A. L., Hair, J. W., Seaman, S. T., Scola, S., Harper, D. B., Smith, J. A., Fenn, M. A., Ferrare, R. A., Saide, P. E., Chemyakin, E. V., and Müller, D.: Calibration of a high spectral resolution lidar using a Michelson interferometer, with data examples from ORACLES, Appl. Optics, 57, 6061–6075, https://doi.org/10.1364/AO.57.006061, 2018.

Cazorla, A., Bahadur, R., Suski, K. J., Cahill, J. F., Chand, D., Schmid, B., Ramanathan, V., and Prather, K. A.: Relating aerosol absorption due to soot, organic carbon, and dust to emission sources determined from in-situ chemical measurements, Atmos. Chem. Phys., 13, 9337–9350, https://doi.org/10.5194/acp-13-9337-2013, 2013.

Chang, I., Gao, L., Burton, S. P., Chen, H., Diamond, M., Ferrare, R. A., Flynn, C. J., Kacenelenbogen, M., LeBlanc, S. E., Meyer, K. G., Pistone, K., Schmidt, S., Segal-Rozenhaimer, M., Shinozuka, Y., Wood, R., Zuidema, P., Redemann, J., and Christopher, S. A.: Spatiotemporal heterogeneity of aerosol and cloud properties over the southeast Atlantic: An observational analysis, Geophys. Res. Lett., 48, e2020GL091469, https://doi.org/10.1029/2020GL091469, 2021.

Chen, H., Schmidt, S., King, M. D., Wind, G., Bucholtz, A., Reid, E. A., Segal-Rozenhaimer, M., Smith, W. L., Taylor, P. C., Kato, S., and Pilewskie, P.: The Effect of Low-Level Thin Arctic Clouds on Shortwave Irradiance: Evaluation of Estimates from Spaceborne Passive Imagery with Aircraft Observations, Atmos. Meas. Tech., 14, 2673–2697, https://doi.org/10.5194/amt-14-2673-2021, 2021.

Chen, H., Schmidt, S., Massie, S. T., Nataraja, V., Norgren, M. S., Gristey, J. J., Feingold, G., Holz, R. E., and Iwabuchi, H.: The Education and Research 3D Radiative Transfer Toolbox (EaR3T) – Towards the Mitigation of 3D Bias in Airborne and Spaceborne Passive Imagery Cloud Retrievals, Atmos. Meas. Tech. Discuss. [preprint], https://doi.org/10.5194/amt-2022-143, in review, 2022.

Cochrane, S. P., Schmidt, K. S., Chen, H., Pilewskie, P., Kittelman, S., Redemann, J., LeBlanc, S., Pistone, K., Kacenelenbogen, M., Segal Rozenhaimer, M., Shinozuka, Y., Flynn, C., Platnick, S., Meyer, K., Ferrare, R., Burton, S., Hostetler, C., Howell, S., Freitag, S., Dobracki, A., and Doherty, S.: Above-cloud aerosol radiative effects based on ORACLES 2016 and ORACLES 2017 aircraft experiments, Atmos. Meas. Tech., 12, 6505–6528, https://doi.org/10.5194/amt-12-6505-2019, 2019.

Cochrane, S. P., Schmidt, K. S., Chen, H., Pilewskie, P., Kittelman, S., Redemann, J., LeBlanc, S., Pistone, K., Kacenelenbogen, M., Segal Rozenhaimer, M., Shinozuka, Y., Flynn, C., Dobracki, A., Zuidema, P., Howell, S., Freitag, S., and Doherty, S.: Empirically derived parameterizations of the direct aerosol radiative effect based on ORACLES aircraft observations, Atmos. Meas. Tech., 14, 567–593, https://doi.org/10.5194/amt-14-567-2021, 2021.

Coddington, O., Schmidt, K. S., Pilewskie, P., Gore, W. J., Bergstrom, R., Roman, M., Redemann, J., Russell, P. B., Liu, J., and Schaaf, C. C.: Aircraft measurements of spectral surface albedo and its consistency with ground-based and space-borne observations, J. Geophys. Res., 113, D17209, doi:10.1029/2008JD010089, 2008.

Coddington, O. M., Pilewskie, P., Redemann, J., Platnick, S., Russell, P. B., Schmidt, K. S., and Vukicevic, T.: Examining the impact of overlying aerosols on the retrieval of cloud optical properties from passive remote sensing, J. Geophys. Res.-Atmos., 115, D10211, https://doi.org/10.1029/2009JD012829, 2010.

Crisp, D.: Measuring Atmospheric Carbon Dioxide from Space with the Orbiting Carbon Observatory-2 (OCO-2), P. Soc. Photo.-Opt. Ins., 9607, 960702, https://doi.org/10.1117/12.2187291, 2015.

Cros, S., Albuisson, M., and Wald, L.: Simulating Meteosat-7 broadband radiances using two visible channels of Meteosat-8, Sol. Energy, 80, 361–367, https://doi.org/10.1016/j.solener.2005.01.012, 2006.

Curry, J. A., Schramm, J. L., Serreze, M. C., and Ebert, E. E.: Water vapor feedback over the Arctic Ocean, J. Geophys. Res., 100, 14223–14229, 1995.

Curry, J. A., Rossow, W. B., Randall, D., and Schramm, J. L.: Overview of arctic cloud and radiation characteristics, J. Climate, 9, 1731–1764, 1996.

Davies, E. R.: Machine Vision: Theory, Algorithms, Practicalities, 3rd Edition, Elsevier, Inc., 934 pp., 2005.

Deneke, H., Barrientos-Velasco, C., Bley, S., Hünerbein, A., Lenk, S., Macke, A., Meirink, J. F., Schroedter-Homscheidt, M., Senf, F., Wang, P., Werner, F., and Witthuhn, J.: Increasing the spatial resolution of cloud property retrievals from Meteosat SEVIRI by use of its high-resolution visible channel: implementation and examples, Atmos. Meas. Tech., 14, 5107–5126, https://doi.org/10.5194/amt-14-5107-2021, 2021.

Doherty, S. J., Saide, P. E., Zuidema, P., Shinozuka, Y., Ferrada, G. A., Gordon, H., Mallet, M., Meyer, K., Painemal, D., Howell, S. G., Freitag, S., Dobracki, A., Podolske, J. R., Burton, S. P., Ferrare, R. A., Howes, C., Nabat, P., Carmichael, G. R., da Silva, A., Pistone, K., Chang, I., Gao, L., Wood, R., and Redemann, J.: Modeled and observed properties related to the direct aerosol radiative effect of biomass burning aerosol over the southeastern Atlantic, Atmos. Chem. Phys., 22, 1–46, https://doi.org/10.5194/acp-22-1-2022, 2022.

Dubovik, O., Holben, B.,Eck, T. F., Smirnov, A., Kaufman, Y. J., King, M. D., Tanré, D., and Slutsker, I.: Variability of absorption and optical properties of key aerosol types observed in worldwide locations. J. Atmos. Sci., 59, 590–608 , 2002.

Dubovik, O., Li, Z., Mishchenko, M. I., Tanré, D., Karol, Y., Bojkov, B., Cairns, B., Diner, D. J., Espinosa, W. R., Goloub, P., Gu, X., Hasekamp, O., Hong, J., Hou, W., Knobelspiesse, K. D., Landgraf, J., Li, L., Litvinov, P., Liu, Y., Lopatin, A., Marbach, T., Maring, H., Martins, V., Meijer, Y., Milinevsky, G., Mukai, S., Parol, F., Qiao, Y., Remer, L., Rietjens, J., Sano, I., Stammes, P., Stamnes, S., Sun, X., Tabary, P., Travis, L. D., Waquet, F., Xu, F., Yan, C., and Yin, D.: Polarimetric remote sensing of atmospheric aerosols: Instruments, methodologies, results, and perspectives, J. Quant. Spectrosc. Radiat. Transf., 224, 474–511, https://doi.org/10.1016/j.jqsrt.2018.11.024, 2019.

Dunagan, S., Johnson, R., Zavaleta, J., Russell, P., Schmid, B., Flynn, C., Redemann, J., Shinozuka, Y., Livingston, J., and Segal Rozenhaimer, M.: Spectrometer for Sky-Scanning Sun-Tracking Atmospheric Research (4STAR): Instrument Technology, Remote Sensing, 5, 3872–3895, https://doi.org/10.3390/rs5083872, 2013.

Ehrlich, A., Bierwirth, E., Istomina, L., and Wendisch, M.: Combined retrieval of Arctic liquid water cloud and surface snow properties using airborne spectral solar remote sensing, Atmos. Meas. Tech., 10, 3215–3230, https://doi.org/10.5194/amt-10-3215-2017, 2017.

Emde, C., Buras-Schnell, R., Kylling, A., Mayer, B., Gasteiger, J., Hamann, U., Kylling, J., Richter, B., Pause, C., Dowling, T., and Bugliaro, L.: The libRadtran software package for radiative transfer calculations (version 2.0.1), Geosci. Model Dev., 9, 1647–1672, https://doi.org/10.5194/gmd-9-1647-2016, 2016.

Evans, K. F.: The spherical harmonics discrete ordinate method for three-dimensional atmospheric radiative transfer, J. Atmos. Sci., 55, 429–446, 1998.

Gardner, A. S., and Sharp, M. J.: A review of snow and ice albedo and the development of a new physically based broadband albedo parameterization. J. Geophys. Res., 115, F01009, doi:10.1029/2009JF001444, 2010.

Gonzalez, R. C., Woods, R. E., and Eddins, S. L.: Image Segmentation. Digital Image Processing, 600–603, 2002.

Gristey, J. J., Feingold, G., Glenn, I. B., Schmidt, K. S., and Chen, H.: Surface Solar Irradiance in

Continental Shallow Cumulus Fields: Observations and Large-Eddy Simulation, J. Atmos. Sci., 77, 1065–1080, https://doi.org/10.1175/JAS-D-19-0261.1, 2020a.

Gristey, J. J., Feingold, G., Glenn, I. B., Schmidt, K. S., and Chen, H.: On the Relationship Between Shallow Cumulus Cloud Field Properties and Surface Solar Irradiance, Geophysical Research Letters, 47, e2020GL090152, https://doi.org/10.1029/2020GL090152, 2020b.

Gristey, J. J., Feingold, G., Glenn, I. B., Schmidt, K. S., and Chen, H.: Influence of Aerosol Embedded in Shallow Cumulus Cloud Fields on the Surface Solar Irradiance, Journal of Geophysical Research: Atmospheres, 127, e2022JD036822, https://doi.org/10.1029/2022JD036822, 2022.

Haeberli, P., and Voorhies, D.: Image processing by linear interpolation and extrapolation, IRIS Universe Magazine, 28, 8–9, 1994.

Hair, J. W., Hostetler, C. A., Cook, A. L., Harper, D. B., Ferrare, R. A., Mack, T. L., Welch, W., Isquierdo, L. R., and Hovis, F. E.: Airborne high spectral resolution lidar for profiling aerosol optical properties, Appl. Optics, 47, 6734–6752, 2008.

Hartmann, D. L., and Ceppi, P.: Trends in the CERES dataset, 2000-13: The effects of sea ice and jet shifts and comparison to climate models, J. Climate, 27, 2444–2456, 2014.

Haywood, J. M., Abel, S. J., Barrett, P. A., Bellouin, N., Blyth, A., Bower, K. N., Brooks, M., Carslaw, K., Che, H., Coe, H., Cotterell, M. I., Crawford, I., Cui, Z., Davies, N., Dingley, B., Field, P., Formenti, P., Gordon, H., de Graaf, M., Herbert, R., Johnson, B., Jones, A. C., Langridge, J. M., Malavelle, F., Partridge, D. G., Peers, F., Redemann, J., Stier, P., Szpek, K., Taylor, J. W., Watson-Parris, D., Wood, R., Wu, H., and Zuidema, P.: The CLoud–Aerosol–Radiation Interaction and Forcing: Year 2017 (CLARIFY-2017) measurement campaign, Atmos. Chem. Phys., 21, 1049–1084, https://doi.org/10.5194/acp-21-1049-2021, 2021.

Heidinger, A. K., Foster, M. J., Walther, A., and Zhao, X.: The Pathfinder Atmospheres-Extended AVHRR climate dataset, B. Am. Meteorol. Soc., 95, 909–922, https://doi.org/10.1175/BAMS-D-12-00246.1, 2014.

Henderson, D. S., L'Ecuyer, T., Stephens, G., Partain, P., and Sekiguchi, M.: A multisensor perspective on the radiative impacts of clouds and aerosols, J. Appl. Meteorol. Clim., 52, 853–871, 2013.

Illingworth, A. J., Barker, H. W., Beljaars, A., Chepfer, H., Delanoe, J., Domenech, C., Donovan, D. P., Fukuda, S., Hirakata, M., Hogan, R. J., Huenerbein, A., Kollias, P., Kubota, T., Nakajima, T., Nakajima, T. Y., Nishizawa, T., Ohno, Y., Okamoto, H., Oki, R., Sato, K., Satoh, M., Wandinger, U., Wehr, T., and van Zadelhoff, G.: The EarthCARE Satellite: the next step forward in global measurements of clouds, aerosols, precipitation and radiation, B. Am. Meteorol. Soc, 96, 1311–1332, https://doi.org/10.1175/BAMS-D-12-00227.1, 2015.

IPCC: Climate Change 2013: The Physical Science Basis. Contribution of Working Group I to the Fifth Assessment Report of the Intergovernmental Panel on Climate Change, edited by: Stocker, T. F., Qin, D., Plattner, G.-K., Tignor, M., Allen, S. K., Boschung, J., Nauels, A., Xia, Y., Bex, V. and Midgley, P. M., Cambridge University Press, Cambridge, UK and New York, USA, 2013.

Iwabuchi, H.: Efficient Monte Carlo methods for radiative transfer modeling, J. Atmos. Sci., 63, 2324–2339, 2006.

Kay, J. E., and L'Ecuyer, T.: Observational constraints on Arctic Ocean clouds and radiative fluxes during the early 21st century, J. Geophys. Res., 118, 7219–7236, 2013.

Kindel, B. C.: Cloud shortwave spectral radiative properties: Airborne hyperspectral measurements and modeling of irradiance, Ph.D. Dissertation, University of Colorado Boulder, United States, 130 pp., 2010.

Kindel, B. C., Schmidt, K. S., Pilewskie, P., Baum, B. A., Yang, P., and Platnick, S.: Observations and modeling of ice cloud shortwave spectral albedo during the Tropical Composition, Cloud and Climate Coupling Experiment (TC^4), J. Geophys. Res., 115, D00J18, doi:10.1029/2009JD013127, 2010.

King, M.D., Kaufman, Y.J., Menzel, W.P., and Tanre, D.: Remote sensing of cloud, aerosol, and water vapor properties from the moderate resolution imaging spectrometer (MODIS), IEEE Trans. Geosci. Remote Sens., 30, 2-27, 1992.

King, M. D., Tsay, S.-C., Platnick, S. E., Wang, M., and Liou, K. N.: Cloud retrieval algorithms for MODIS: Optical thickness, effective particle radius, and thermodynamic phase, Tech. rep., MODIS Science Team, MODIS Algorithm Theoretical Basis Document No. ATBD-MOD-05, NASA Goddard Space Flight Center, Greenbelt, MD USA, 1997.

King, M. D., Platnick, S., Yang, P., Arnold, G. T., Gray, M. A., Riedi, J. C., Ackerman, S. A., and Liou, K. N.: Remote sensing of liquid water and ice cloud optical thickness and effective radius in the Arctic: Application of airborne multispectral MAS data, J. Atmos. Ocean. Tech, 21, 857–875, 2004.

King, M., and Platnick, S.: The Earth Observing System (EOS), Comprehensive Remote Sensing, 7, 26, doi:10.1016/b978-0-12-409548-9.10312-4, 2018.

Koch, D. and Del Genio, A. D.: Black carbon semi-direct effects on cloud cover: review and synthesis, Atmos. Chem. Phys., 10, 7685–7696, https://doi.org/10.5194/acp-10-7685-2010, 2010.

Kurucz, R. L.: Synthetic infrared spectra, In Infrared Solar Physics, Rabin, D. M., Jefferies, J. T., and Lindsey, C. (Eds.), Springer-Science+Business Media, B. V., 523–531, 1992.

LeBlanc, S. E., Schmidt, K. S., Pilewskie, P., Redemann, J., Hostetler, C., Ferrare, R., Hair, J., Langridge, J. M., and Lack, D. A.: Spectral aerosol direct radiative forcing from airborne radiative measurements during CalNex and ARCTAS, J. Geophys. Res., 117, D00V20, https://doi.org/10.1029/2012JD018106, 2012.

LeBlanc, S. E., Redemann, J., Flynn, C., Pistone, K., Kacenelenbogen, M., Segal-Rosenheimer, M., Shinozuka, Y., Dunagan, S., Dahlgren, R. P., Meyer, K., Podolske, J., Howell, S. G., Freitag, S., Small-Griswold, J., Holben, B., Diamond, M., Wood, R., Formenti, P., Piketh, S., Maggs-Kölling, G., Gerber, M., and Namwoonde, A.: Above-cloud aerosol optical depth from airborne observations in the southeast Atlantic, Atmos. Chem. Phys., 20, 1565–1590, https://doi.org/10.5194/acp-20-1565-2020, 2020.

Levis, A., Schechner, Y. Y., Davis, A. B., and Loveridge, J.: Multi-View Polarimetric Scattering Cloud Tomography and Retrieval of Droplet Size, Remote Sens., 12, 2831, https://doi.org/10.3390/rs12172831, 2020.

Li, J., Scinocca, J., Lazare, M., McFarlane, N., von Salzen, K., and Solheim, L.: Ocean Surface Albedo and Its Impact on Radiation Balance in Climate Models, J. Climate, 19, 6314–6333, 2006.

Liu, Y., Ackerman, S. A., Maddux, B. C., Key, J. R., and Frey, R. A.: Errors in cloud detection over the arctic using a satellite imager and implications for observing feedback mechanisms, J. Climate, 23, 1894–1907, 2010.

Loeb, N. G., and Manalo-Smith, N.: Top-of-atmosphere direct radiative effect of aerosols over global oceans from merged CERES and MODIS observations, J. Climate, 18, 3506–3526, 2005.

Loeb, N. G., Kato, S., Su, W., Wong, T., Rose, F. G., Doelling, D. R., Norris, J. R., and Huang, X.: Advances in understanding top-of-atmosphere radiation variability from satellite observations, Surv. Geophys., 33, 359–385, 2012.

Long, C. N., Bucholtz, A., Jonsson, H., Schmid, B., Vogelmann, A., and Wood, J.: A Method of Correcting for Tilt from Horizontal in Downwelling Shortwave Irradiance Measurements on Moving Platforms, The Open Atmospheric Science Journal, 4, 78–87, 2010.

Lyapustin, A., Gatebe, C. K., Kahn, R., Brandt, R., Redemann, J., Russell, P., King, M. D., Pedersen, C. A., Gerland, S., Poudyal, R., Marshak, A., Wang, Y., Schaaf, C., Hall, D., and Kokhanovsky, A.: Analysis of snow bidirectional reflectance from ARCTAS Spring-2008 campaign, Atmos. Chem. Phys., 10, 4359–4375, 2010.

Malinka, A., Zege, E., Heygster, G., and Istomina, L.: Reflective properties of white sea ice and snow, The Cryosphere, 10, 2541–2557, https://doi.org/10.5194/tc-10-2541-2016, 2016.

Malinka, A., Zege, E., Istomina, L., Heygster, G., Spreen, G., Perovich, D., and Polashenski, C.: Reflective properties of melt ponds on sea ice, The Cryosphere, 12, 1921–1937, https://doi.org/10.5194/tc-12-1921-2018, 2018.

Masuda, R., Iwabuchi, H., Schmidt, K. S., Damiani, A. and Kudo, R.: Retrieval of Cloud Optical Thickness from Sky-View Camera Images using a Deep Convolutional Neural Network based on Three-Dimensional Radiative Transfer, Remote Sensing, 11(17), 1962, doi:10.3390/rs11171962, 2019.

Marshak, A., Davis, A., Wiscombe, W., and Cahalan, R.: Radiative smoothing in fractal clouds, J. Geophys. Res., 100, 26247–26261, https://doi.org/10.1029/95JD02895, 1995.

Marshak, A., Wen, G., Coakley, J., Remer, L., Loeb, N. G., and Cahalan, R. F.: A simple model for the cloud adjacency effect and the apparent bluing of aerosols near clouds, J. Geophys. Res., 113, D14S17, https://doi.org/10.1029/2007JD009196, 2008.

Massie, S. T., Schmidt, K. S., Eldering, A., and Crisp, D.: Observational evidence of 3-D cloud effects in OCO-2 CO2 retrievals, J. Geophys. Res. Atmos., 122, 7064–7085, https://doi.org/10.1002/2016JD026111, 2017.

Mayer, B. and Kylling, A.: Technical note: The libRadtran software package for radiative transfer calculations – description and examples of use, Atmos. Chem. Phys., 5, 1855–1877, https://doi.org/10.5194/acp-5-1855-2005, 2005.

Mayer, B.: Radiative transfer in the cloudy atmosphere, EPJ Web of Conferences, 1, 75–99, doi:10.1140/epjconf/e2009-00912-1, 2009.

Meyer, K., Platnick, S., and Zhang, Z.: Simultaneously inferring above-cloud absorbing aerosol optical thickness and underlying liquid phase cloud optical and microphysical properties using MODIS, J. Geophys. Res.-Atmos., 120, 5524–5547, https://doi.org/10.1002/2015JD023128, 2015.

Meywerk, J. and Ramanathan, V.: Observations of the spectral clear-sky aerosol forcing over the tropical Indian Ocean, J. Geophys. Res., 104, 24359–24370, 1999.

Mlawer, E. J., Taubman, S. J., Brown, P. D., Iacono, M. J., and Clough, S. A.: Radiative transfer for inhomogeneous atmospheres: RRTM, a validated correlated-k model for the longwave, J. Geophys. Res., 102, 16663–16682, 1997.

Moody, E. G., King, M. D., Schaaf, C. B., Hall, D. K., and Platnick, S.: Northern Hemisphere five-year average (2000-2004) spectral albedos of surfaces in the presence of snow: Statistics computed from Terra MODIS land products, Remote Sens. Environ., 111, 337–345, 2007.

Nakajima, T., and King, M. D.: Determination of the optical thickness and effective particle radius of clouds from reflected solar radiation measurements. Part I: Theory, J. Atmos. Sci., 47, 1878–1893, 1990.

Nataraja, V., Schmidt, S., Chen, H., Yamaguchi, T., Kazil, J., Feingold, G., Wolf, K., and Iwabuchi, H.: Segmentation-Based Multi-Pixel Cloud Optical Thickness Retrieval Using a Convolutional Neural Network, Atmos. Meas. Tech. Discuss. [preprint], https://doi.org/10.5194/amt-2022-45, in review, 2022.

Norgren, M. S., Wood, J., Schmidt, K. S., van Diedenhoven, B., Stamnes, S. A., Ziemba, L. D., Crosbie, E. C., Shook, M. A., Kittelman, A. S., LeBlanc, S. E., Broccardo, S., Freitag, S., and Reid, J. S.: Above-aircraft cirrus cloud and aerosol optical depth from hyperspectral irradiances measured by a total-diffuse radiometer, Atmos. Meas. Tech., 15, 1373–1394, https://doi.org/10.5194/amt-15-1373-2022, 2022.

Oreopoulos, L., Cho, N., Lee, D., and Kato, S.: Radiative effects of global MODIS cloud regimes, J. Geophys. Res., 121, 2299–2317, 2016.

Payne, V. H., Drouin, B. J., Oyafuso, F., Kuai, L., Fisher, B. M., Sung, K., Nemchicka, D., Crawford, T. J., Smyth, M., Crisp, D., Adkins, E., Hodges, J. T., Long, D. A., Mlawer, E. J., Merrelli, A., Lunny, E., and O'Dell, C. W.: Absorption coefficient (ABSCO) tables for the Orbiting Carbon Observatories: version 5.1, J. Quant. Spectrosc. Ra., 255, 1–16, https://doi.org/10.1016/j.jqsrt.2020.107217, 2020.

Peers, F., Francis, P., Abel, S. J., Barrett, P. A., Bower, K. N., Cotterell, M. I., Crawford, I., Davies, N. W., Fox, C., Fox, S., Langridge, J. M., Meyer, K. G., Platnick, S. E., Szpek, K., and Haywood, J. M.: Observation of absorbing aerosols above clouds over the south-east Atlantic Ocean from the geostationary satellite SEVIRI – Part 2: Comparison with MODIS and aircraft measurements from the CLARIFY-2017 field campaign, Atmos. Chem. Phys., 21, 3235–3254, https://doi.org/10.5194/acp-21-3235-2021, 2021.

Perovich, D. K., Tucker, W. B., and Ligett, K. A.: Aerial observations of the evolution of ice surface conditions during summer, J. Geophys. Res., 107, SHE24-1–SHE24-14, https://doi.org/10.1029/2000JC000449, 2002.

Perovich, D. K.: Seasonal evolution of the albedo of multiyear Arctic sea ice, J. Geophys. Res., 107(C10), 8044, doi: 10.1029/2000JC000438, 2002.

Pierluissi, J. H., and Peng, G. : New molecular transmission band models for LOWTRAN, Optical Engineering, 24, 541–547, doi: 10.1117/12.7973523, 1985.

Pilewskie, P., Pommier, J., Bergstrom, R., Gore, W., Howard, S., Rabbette, M., Schmid, B., Hobbs, P. V., and Tsay, S. C.: Solar spectral radiative forcing during the Southern African Regional Science Initiative, J. Geophys. Res., 108, 8486, https://doi.org/10.1029/2002JD002411, 2003.

Pincus, R. and Evans, K. F.: Computational cost and accuracy in calculating three-dimensional radiative transfer: Results for new implementations of Monte Carlo and SHDOM, J. Atmos. Sci., 66, 3131–3146, 2009.

Platnick, S., Li, J. Y., King, M. D., Gerber, H., and Hobbs, P. V.: A solar reflectance method for retrieving the optical thickness and droplet size of liquid water clouds over snow and ice surfaces, J. Geophys. Res., 106, 15185–15199, 2001.

Platnick, S., King, M. D., Ackerman, S. A., Menzel, W. P., Baum, B. A., Riédi, J. C., and Frey, R. A.: The MODIS cloud products: Algorithms and examples from Terra, IEEE T. Geosci. Remote, 41, 459–473, 2003.

Platnick, S., Ackerman, S. A., King, M. D., Wind, G., Meyer, K., Menzel, W. P., Frey, R. A., Holz, R. E., Baum, B. A., and Yang, P.: MODIS Atmosphere L2 Cloud Product (06_L2). NASA MODIS Adaptive Processing System, Goddard Space Flight Center, USA, http://dx.doi.org/10.5067/MODIS/MOD06_L2.006, 2017.

Platnick, S., Meyer, K. G., King, M. D., Wind, G., Amarasinghe, N., Marchant, B., Arnold, G. T., Zhang, Z., Hubanks, P. A., Holz, R. E., and Yang, P.: The MODIS cloud optical and microphysical products: Collection 6 updates and examples from Terra and Aqua, IEEE Trans. Geosci. Remote Sens., 55, 502-525, 2017.

Platnick, S., Meyer, K. G., King, M. D., Wind, G., Amarasinghe, N., Marchant, B., Arnold, G. T., Zhang, Z., Hubanks, P. A., Ridgway, B., and Riedi, J.: MODIS Cloud Optical Properties: User Guide for the Collection 6/6.1 Level-2 MOD06/MYD06 Product and Associated Level-3 Datasets version 1.1, https://atmosphere-imager.gsfc.nasa.gov/sites/default/files/ModAtmo/MODISCloudOpticalPropertyUserGuideFinal_v1.1.pdf, 2018.

Redemann, J., Wood, R., Zuidema, P., Doherty, S. J., Luna, B., LeBlanc, S. E., Diamond, M. S., Shinozuka, Y., Chang, I. Y., Ueyama, R., Pfister, L., Ryoo, J.-M., Dobracki, A. N., da Silva, A. M., Longo, K. M., Kacenelenbogen, M. S., Flynn, C. J., Pistone, K., Knox, N. M., Piketh, S. J., Haywood, J. M., Formenti, P., Mallet, M., Stier, P., Ackerman, A. S., Bauer, S. E., Fridlind, A. M., Carmichael, G. R., Saide, P. E., Ferrada, G. A., Howell, S. G., Freitag, S., Cairns, B., Holben, B. N., Knobelspiesse, K. D., Tanelli, S., L'Ecuyer, T. S., Dzambo, A. M., Sy, O. O., McFarquhar, G. M., Poellot, M. R., Gupta, S., O'Brien, J. R., Nenes, A., Kacarab, M., Wong, J. P. S., Small-Griswold, J. D., Thornhill, K. L., Noone, D., Podolske, J. R., Schmidt, K. S., Pilewskie, P., Chen, H., Cochrane, S. P., Sedlacek, A. J., Lang, T. J., Stith, E., Segal-Rozenhaimer, M., Ferrare, R. A., Burton, S. P., Hostetler, C. A., Diner, D. J., Seidel, F. C., Platnick, S. E., Myers, J. S., Meyer, K. G., Spangenberg, D. A., Maring, H., and Gao, L.: An overview of the ORACLES (ObseRvations of Aerosols above CLouds and their intEractionS) project: aerosol–cloud–radiation interactions in the southeast Atlantic basin, Atmos. Chem. Phys., 21, 1507–1563, https://doi.org/10.5194/acp-21-1507-2021, 2021.

Reid, J. S., Maring, H. B., Narisma, G., van den Heever, S., DiGirolamo, L., Ferrare, R., Lawson, P., Mace, G. G., Simpas, J., Tanelli, S., Ziemba, L., van Diedenhoven, B., Bruintjes, R., Bucholtz, A., Cairns, B., Cambaliza, M. O., Chen, G., Diskin, G. S., Flynn, J. H., Hostetler, C. A., Holz, R. E., Lang, T. J., Schmidt, K. S., Smith, G., Sorooshian, A., Thompson, E. J., Thornhill, K. L., Trepte, C., Wang, J., Woods, S., Yoon, S., Alexandrov, M., Alverez, S., Amiot, C., Bennett, J. R., Brooks, M., Burton, S. P., Cayanan, E., Chen, H., Collow, A., Crosbie, E., DaSilva, A., DiGangi, J. P., Flagg, D. D., Freeman, S. W., Fu, D., Fukada, E., Hilario, M. R. A., Hong, Y., Hristova-Veleva, S. M., Kuehn, R., Kowch, R. S., Leung, G. R., Loveridge, J., Meyer, K., Miller, R., Montes, M. J., Moum, J. N., Nenes, T., Nesbit, S. W., Norgen, M., Novak, E., Rauber, R. M., Reid, E. A., Rutledge, S., Schlosser, J. S., Sekiyama,

T. T., Shook, M. A., Sokolowsky, G. A., Stamnes, S. A., Sy, O. O., Tanaka, T. Y., Wasilewski, A., Xian, P., Xiao, Q., and Zavaleta, J.: The coupling between tropical meteorology, aerosol lifecycle, convection, and radiation, during the Clouds, Aerosol and Monsoon Processes Philippines Experiment (CAMP^{2}Ex), B. Am. Meteorol. Soc., in review, 2022.

Remer, L. A., Kaurman, Y. J., Tanré, D., Mattoo, S., Chu, D. A., Martins, J. V., Li, R.-R., Ichoku, C., Levy, R. C., Kleidman, R. G., Eck, T. F., Vermote, E., and Holben, B.N.: The MODIS aerosol algorithm, products, and validation, J. Atmos. Sci., 62, 947–973, 2005.

Rothman, L., Jacquemart, D., Barbe, A., Chris Benner, D., Birk, M., Brown, L., Carleer, M., Chackerian, C., Chance, K., Coudert, L., Dana, V., Devi, V., Flaud, J.-M., Gamache, R., Goldman, A., Hartmann, J.-M., Jucks, K., Maki, A., Mandin, J.-Y., Massie, S., Orphal, J., Perrin, A., Rinsland, C., Smith, M., Tennyson, J., Tolchenov, R., Toth, R., Vander Auwera, J., Varanasi, P., and Wagner, G.: The HITRAN 2004 molecular spectroscopic database, J. Quant. Spectrosc. Ra., 96, 139–204, https://doi.org/10.1016/j.jqsrt.2004.10.008, 2005.

Rozenhaimer, M., Barton, N., Redemann, J., Schmidt, S., LeBlanc, S., Anderson, B., Winstead, E., Corr, C. A., Moore, R., Thornhill, K. L., and Cullather, R. I.: Bias and sensitivity of boundary layer clouds and surface radiative fluxes in MERRA-2 and airborne observations over the Beaufort Sea during the ARISE campaign, J. Geophs. Res. Atmos., 123, doi: 10.1029/2018JD028349, 2018.

Russell, P. B., Redemann, J., Schmid, B., Bergstrom, R. W., Livingston, J. M., Mcintosh, D. M., Ramirez, S. A., Hartley, S., Hobbs, P. V., Quinn, P. K., Carrico, C. M., Rood, M. J., Ostrom, E., Noone, K. J., Von Hoyningen-Huene, W., and Remer, L.: Comparison of Aerosol Single Scattering Albedos Derived by Diverse Techniques in Two North Atlantic Experiments, J. Atmos. Sci., 59.3, 609–19, 2002.

Schmetz, J., Pili, P., Tjemkes, S., Just, D., Kerkmann, J., Rota, S., and Ratier, A.: Supplement to An Introduction to Meteosat Second Generation (MSG), B. Am. Meteorol. Soc., 83, 992–992, https://doi.org/10.1175/bams-83-7-schmetz-2, 2002.

Schmid, B. and Wehrli, C.: Comparison of sun photometer calibration by Langley technique and standard lamp, Appl. Optics, 34, 4500–4512, 1995.

Schmidt, K. S., Pilewskie, P., Platnick, S., Wind, G., Yang, P., and Wendisch, M.: Comparing irradiance fields derived from Moderate Resolution Imaging Spectroradiometer airborne simulator cirrus cloud retrievals with solar spectral flux radiometer measurements, J. Geophys. Res., 112, D24206, doi:10.1029/2007JD008711, 2007.

Schmidt, S., Pilewskie, P., Mayer, B., Wendisch, M., Kindel, B., Platnick, S., King, M. D., Wind, G., Arnold, G. T., Tian, L., Heymsfield, G., and Kalesse, H.: Apparent absorption of solar spectral irradiance in heterogeneous ice clouds, J. Geophys. Res., 115, D00J22, https://doi.org/10.1029/2009JD013124, 2010a.

Schmidt, K. S., Pilewskie, P., Bergstrom, R., Coddington, O., Redemann, J., Livingston, J., Russell, P., Bierwirth, E., Wendisch, M., Gore, W., Dubey, M. K., and Mazzoleni, C.: A new method for deriving aerosol solar radiative forcing and its first application within MILAGRO/INTEX-B, Atmos. Chem. Phys., 10, 7829– 7843, https://doi.org/10.5194/acp-10-7829-2010, 2010b.

Schmidt, S., and Pilewskie, P.: Airborne measurements of spectral shortwave radiation in cloud and aerosol remote sensing and energy budget studies, In A. A. Kokhanovsky (Ed.), Light Scattering Reviews, Vol. 6: Light Scattering and Remote Sensing of Atmosphere and Surface, Berlin, Heidelberg: Springer Berlin Heidelberg, 239–288, doi:10.1007/978-3-642-15531-4_6, 2012.

Schmidt, S., Massie, S., Chen, H., Crisp, D., Kulawik, S., Chen, Y.-W., Merrelli, A., McDuffie, J., Iwabuchi, H.: Uncovering the Mechanism for Trace Gas Spectroscopy Biases in the Vicinity of Clouds With the OCO-2 3D Radiative Transfer Satellite Radiance Simulator, *to be submitted*, 2022.

Shupe, M. D., Walden, V. P., Eloranta, E., Uttal, T., Campbell, J. R., Starkweather, S. M., and Shiobara, M.: Clouds at Arctic atmospheric observatories. Part I: Occurrence and macrophysical properties, J. Appl. Meteorol. Clim., 50, 626–644, 2011.

Shupe, M. D., and Intrieri, J. M.: Cloud radiative forcing of the Arctic surface: The influence of cloud properties, surface albedo, and solar zenith angle, J. Climate, 17, 616–628, 2004.

Smith, W. L., Hansen, C., Bucholtz, A., Anderson, B. E., Beckley, M., Corbett, J. G., Cullather, R. I., Hines, K.M., Hofton, M., Kato, S., Lubin, D., Moore, R. H., Segal Rosenhaimer, M., Redemann, J., Schmidt, S., Scott, R., Song, S., Barrick, J. D., Blair, J.B., Bromwich, D. H., Brooks, C., Chen, G., Cornejo, H., Corr, C. A., Ham, S., Kittelman, A. S., Knappmiller, S., LeBlanc, S., Loeb, N. G., Miller, C., Nguyen, L., Palikonda, R., Rabine, D., Reid, E. A., Richter-Menge, J. A., Pilewskie, P., Shinozuka, Y., Spangenberg, D., Stackhouse, P., Taylor, P., Thornhill, K. L., van Gilst, D., and Winstead, E.: Arctic Radiation-IceBridge Sea and Ice Experiment: The Arctic radiant energy system during the critical seasonal ice transition. Bull. Amer. Meteor. Soc., 98, 1399–1426, https://doi.org/10.1175/BAMS-D-14-00277.1, 2017.

Song, S., Schmidt, K. S., Pilewskie, P., King, M. D., Heidinger, A. K., Walther, A., Iwabuchi, H., Wind, G., and Coddington, O. M.: The Spectral Signature of Cloud Spatial Structure in Shortwave Irradiance, Atmos. Chem. Phys., 16, 13791–13806, https://doi.org/10.5194/acp-16-13791-2016, 2016.

Stamnes, K., Tsay, S.-C., Wiscombe, W., and Jayaweera, K.: Numerically stable algorithm for discrete-ordinate-method radiative transfer in multiple scattering and emitting layered media, Appl. Opt., 27, 2502–2509, 1988.

Strahler, A. H., Lucht, W., Schaaf, C. B., Tsang, T., Gao, F., Li, X., Muller, J., Lewis, P., and Barnsley, M. J.: MODIS BRDF/albedo product: algorithm theoretical basis document version 5.0, https://lpdaac.usgs.gov/documents/97/MCD43_ATBD.pdf, 1999.

Twomey, S.: Pollution and the planetary albedo, Atmos. Environ., 8, 1251–1256, 1974.

Twomey, S.: Atmospheric Aerosols, Section 12.3, Elsevier Scientific Publishing Co., UK, 278–290, 1977.

van der Werf, G. R., Randerson, J. T., Giglio, L., Collatz, G. J., Mu, M., Kasibhatla, P. S., Morton, D. C., DeFries, R. S., Jin, Y., and van Leeuwen, T. T.: Global fire emissions and the contribution of deforestation, savanna, forest, agricultural, and peat fires (1997–2009), Atmos. Chem. Phys., 10, 11707–11735, https://doi.org/10.5194/acp-10-11707-2010, 2010.

Vermote, E. F., Roger, J. C., and Ray J. P.: MODIS Surface Reflectance User's Guide, MODIS Land Surface Reflectance Science Computing Facility, Version 1.4, 1-35, 2015.

Warren, S. G., Roesler, C. S., and Brandt, R. E.: Solar radiation processes in the east Antarctic sea-ice zone. Antarctic J. United States, 32, 185–186, 1997.

Wendisch, M., Müller, D., Schell, D., and Heintzenberg, J.: An airborne spectral albedo meter with active horizontal stabilization, J. Atmos. Ocean. Tech, 18, 1856–1866, 2001.

Wendisch, M., Macke, A., Ehrlich, A., Lüpkes, C., Mech, M., Chechin, D., Dethloff, K., Barrientos Velasco, C., Bozem, H., Brückner, M., Clemen, H., Crewell, S., Donth, T., Dupuy, R., Ebell, K., Egerer, U., Engelmann, R., Engler, C., Eppers, O., Gehrmann, M., Gong, X., Gottschalk, M., Gourbeyre, C., Griesche, H., Hartmann, J., Hartmann, M., Heinold, B., Herber, A., Herrmann, H., Heygster, G., Hoor, P., Jafariserajehlou, S., Jäkel, E., Järvinen, E., Jourdan, O., Kästner, U., Kecorius, S., Knudsen, E. M., Köllner, F., Kretzschmar, J., Lelli, L., Leroy, D., Maturilli, M., Mei, L., Mertes, S., Mioche, G., Neuber, R., Nicolaus, M., Nomokonova, T., Notholt, J., Palm, M., van Pinxteren, M., Quaas, J., Richter, P., Ruiz-Donoso, E., Schäfer, M., Schmieder, K., Schnaiter, M., Schneider, J., Schwarzenböck, A., Seifert, P., Shupe, M. D., Siebert, H., Spreen, G., Stapf, J., Stratmann, F., Vogl, T., Welti, A., Wex, H., Wiedensohler, A., Zanatta, M., and Zeppenfeld, S.: The Arctic Cloud Puzzle: Using ACLOUD/PASCAL Multiplatform Observations to Unravel the Role of Clouds and Aerosol Particles in Arctic Amplification, B.. Am. Meteorol. Soc., 100, 841–871, https://doi.org/10.1175/BAMS-D-18-0072.1, 2019.

Wielicki, B. A., Barkstrom, B. R., Harrison, E. F., Lee III, R. B., Smith, G. L., and Cooper, J. E.: Clouds and the Earth's Radiant Energy System (CERES): An Earth Observing System Experiment. Bull. Amer. Meteor. Soc., 77, 853–868, 1996.

Wiscombe, W. J., and Warren, S. G.: A model for the spectral albedo of snow. I: Pure snow, J. Atmos. Sci., 37, 2712–2733, 1981.

Wood, J., Smyth, T. J., and Estellés, V.: Autonomous marine hyperspectral radiometers for determining solar irradiances and aerosol optical properties, Atmos. Meas. Tech., 10, 1723–1737, https://doi.org/10.5194/amt-10-1723-2017, 2017.

Zuidema, P., Redemann, J., Haywood, J. M., Wood, R., Piketh, S., Hipondoka, M., and Formenti, P.: Smoke and Clouds above the Southeast Atlantic: Upcoming Field Campaigns Probe Absorbing Aerosol's Impact on Climate, B. Am. Meteorol. Soc., 97, 1131–1135, https://doi.org/10.1175/BAMS-D-15-00082.1, 2016.

Appendix

2.A Diffuse/direct correction for the polar angle response

The polar angle response (“cosine response”) needs to be done separately for the direct and the diffuse downwelling radiation. Therefore, these two components first need to be separated, assuming

$$DR(\lambda) = DR_{clear}(\lambda) \cdot f + DR_{cloud}(\lambda)(1 - f)$$

where DR is the diffuse (to total, or global) ratio, *f* is the clear-sky fraction, and *(1–f)* is the fraction of a diffuser (clouds).

We can make the simplification $DR_{cloud}(\lambda) = 1.0$, (i.e., the radiation under clouds does not have a direct component), leading to

$$DR(\lambda) = 1 - f \cdot \left(1 - DR_{clear}(\lambda)\right) \tag{2.A1}$$

The SPN1 measures the broadband diffuse radio, which we denote as DR_{SPN1}:

$$DR_{SPN1} = \frac{\int_{\lambda_1}^{\lambda_2} DR(\lambda) \cdot F^{\downarrow}(\lambda) d\lambda}{\int_{\lambda_1}^{\lambda_2} F^{\downarrow}(\lambda) d\lambda} \tag{2.A2}$$

where λ_1 and λ_2 indicate the wavelength range of SPN1, and $F^{\downarrow}(\lambda)$ is the calculated downwelling (global) spectral irradiance from a RTM (we did not use the SSFR measurements because they only encompass a sub-range of SPN-1). Substituting Equation (2.A1) into (2.A2), we get

$$DR_{SPN1} = 1 - f \cdot \frac{\int_{\lambda_1}^{\lambda_2} F^{\downarrow}(\lambda) \cdot \left(1 - DR_{clear}(\lambda)\right) d\lambda}{\int_{\lambda_1}^{\lambda_2} F^{\downarrow}(\lambda) d\lambda} \tag{2.A3}$$

We can then determine *f* from

$$f = \frac{(1 - DR_{SPN1}) \cdot \int_{\lambda_1}^{\lambda_2} F_{clear}^{\downarrow}(\lambda) d\lambda}{\int_{\lambda_1}^{\lambda_2} F_{clear}^{\downarrow}(\lambda) \cdot \left(1 - DR_{clear}(\lambda)\right) d\lambda} \tag{2.A4}$$

and the diffuse/direct ratio can be calculated by using this value of *f* in Equation (2.A1).

2.B Azimuth response

The azimuth response of the SSFR zenith light collector was obtained using the data collected during the so-called calibration flight (2014-10-02), where the aircraft flew a circles to collect radiation measurements at different solar azimuth angles. This was done by referencing the SSFR irradiance measurements to the simultaneous BBR data, building on the fact that unlike SSFR, BBR had no discernable azimuthal dependence. The data used to determine the azimuth response had a solar zenith range of [68.24 º, 71.49 º] with an average of 70.20 º, whereas the solar zenith angle range for the above-cloud case (2014-09-11, where the azimuth correction was applied) was [68.46º to 71.89º] with the mean of 68.91º.

Since SSFR only covers part of BBR's bandwidth from 200 to 3600 nm, RTM calculations were used to fill in SSFR spectra beyond its nominal wavelength range of 350 – 2050 nm. Subsequently, the RTM-extended SSFR irradiance was spectrally integrated (referred to as F_{SSFR}). A second-order Fourier series was then applied to fit the azimuthal dependence captured by the ratio $F_{\mathrm{SSFR}}/F_{\mathrm{BBR}}$, shown in Figure 2.A1. It shows this ratio as a function of reference azimuth angle, defined as the azimuth angle of the sun with respect to the light collector, for which 0 degrees is defined as the aircraft flying due North. A second-order Fourier series was applied to fit the azimuthal dependence of $\mathrm{F_{SSFR}}/\mathrm{F_{BBR}}$. It constitutes SSFR's azimuthal response at this solar zenith angle, which was then used to correct SSFR's downwelling irradiance for the conditions encountered for the SSFR data collected during other research flights. The azimuth response obtained in Figure 2.A1 can be expressed as (with coefficients)

$$\frac{F_{SSFR}}{F_{BBR}} = 0.9460 + 0.0647 \cdot \cos\left(\frac{\phi}{180} \cdot \pi\right) + 0.0160 \cdot \sin\left(\frac{\phi}{180} \cdot \pi\right) - 0.0045 \cdot \cos\left(\frac{\phi}{180} \cdot 2\pi\right) - 0.0015 \cdot \sin\left(\frac{\phi}{180} \cdot 2\pi\right) \qquad \text{(A5)}$$

where ϕ is the reference azimuth angle.

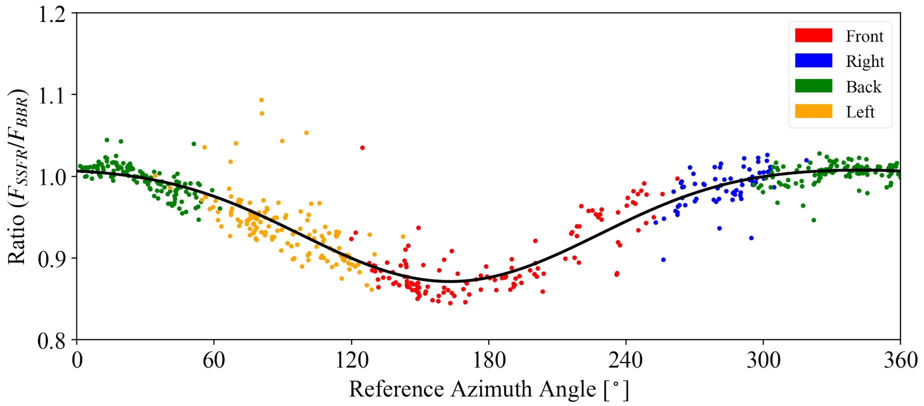

Figure 2.A1. Ratio between spectrally integrated SSFR downwelling irradiance and broadband downwelling irradiance from BBR as a function of reference azimuth angle (solar azimuth position with respect to the sensor, 0 degree pointing north) during 1:00 UTC – 1:36 UTC on 2014-10-03. The relative positions of the sun with respect to the aircraft are indicated by different colors. The black curve is a fitted function using a second order Fourier series.

2.C Adaptive thresholding

The threshold value at each pixel location of the image depends on the neighboring pixel intensities I. For a pixel located at (x, y), the threshold value $T(x, y)$ is calculated through the following steps:

1). A subdomain of size $d \times d$ is selected with (x, y) at the center of the subdomain;

2). The weighted average $C(x, y)$ is calculated for the subdomain using Gaussian weights (Davies 1990) $W(x, y)$, $C(x, y) = \sum_{i=0}^{d} \sum_{j=0}^{d} I(i, j) \cdot W(i, j)$;

3). The threshold for the pixel at (x, y) is the difference of the weighted average calculated in the previous step and a constant C_0, $T(x, y) = C(x, y) - C_0$.

d and C_0 are input parameters that can be adjusted to improve the results. In this study, d is set to 1501 and C_0 is set to 0.

2.D Uncertainty estimation

1). SSFR-BBR irradiance product

For the SSFR spectral measurements, the nominal radiometric uncertainty is 5% (Schmidt et al., 2010a). The nominal uncertainty of BBR measurements is 3% (Smith et al., 2017). As we described in Section 2.2, we corrected the azimuthal dependence of SSFR downwelling irradiance based on the BBR measurements using the method described in Appendix 2.B. After the correction, the SSFR downwelling and upwelling irradiances are still slightly inconsistent with BBR due to an imperfect cosine response comparing to BBR (although they agree with BBR within the range of uncertainty). In addition, the different sun-sensor geometries between the calibration flight (2 October, 2014) and the "0911-above-cloud" case mean that the azimuthal response as measured during the calibration flight does not necessarily fully apply to the case under study. In order to reference SSFR to BBR and simultaneously estimate the uncertainty of the merged product (SSFR-BBR), we applied a scaling method as shown in Figure 2.A2. Figures 2.A2 (a) and (b) show the azimuthally corrected SSFR downwelling and SSFR upwelling irradiance versus BBR. The wide spread of downwelling irradiance indicates that even after applying azimuthal correction for SSFR, some residual uncertainty of the azimuthal response obtained in Appendix 2.B remains in the SSFR measurements after the azimuthal correction. In the upwelling irradiance, the SSFR is more closely related to BBR. Figures 2.A2 (c) and (d) illustrate how we correct for the remaining biases between SSFR and BBR and estimate the uncertainties of the SSFR-BBR product. Figures 2.A2 (c) and (d) show the histogram of the ratio of SSFR and BBR measurements. The ratio histograms indicate a scale factor of 1.006 and 0.946 for the SSFR downwelling and upwelling, with standard deviations of 0.025 and 0.01 when referencing to BBR. The scale factors of 1.006 and 0.946 are applied as divisor to SSFR downwelling and upwelling irradiance respectively. The SSFR irradiance after scaling (referred to as SSFR-BBR) versus BBR is shown in Figures 2.A2 (a) and (c) in green. After scaling, the SSFR-BBR and BBR achieve a better consistency. The standard deviations of 0.025 and 0.01 represent the precision for the downwelling and upwelling irradiance of SSFR-BBR. Thus, we use 2.5% (0.025/1.006*100%) and 1% (0.01/0.946*100%) as the precision estimates for SSFR-BBR downwelling and upwelling, whereas the uncertainty propagates from BBR into the SSFR-BBR product (3%).

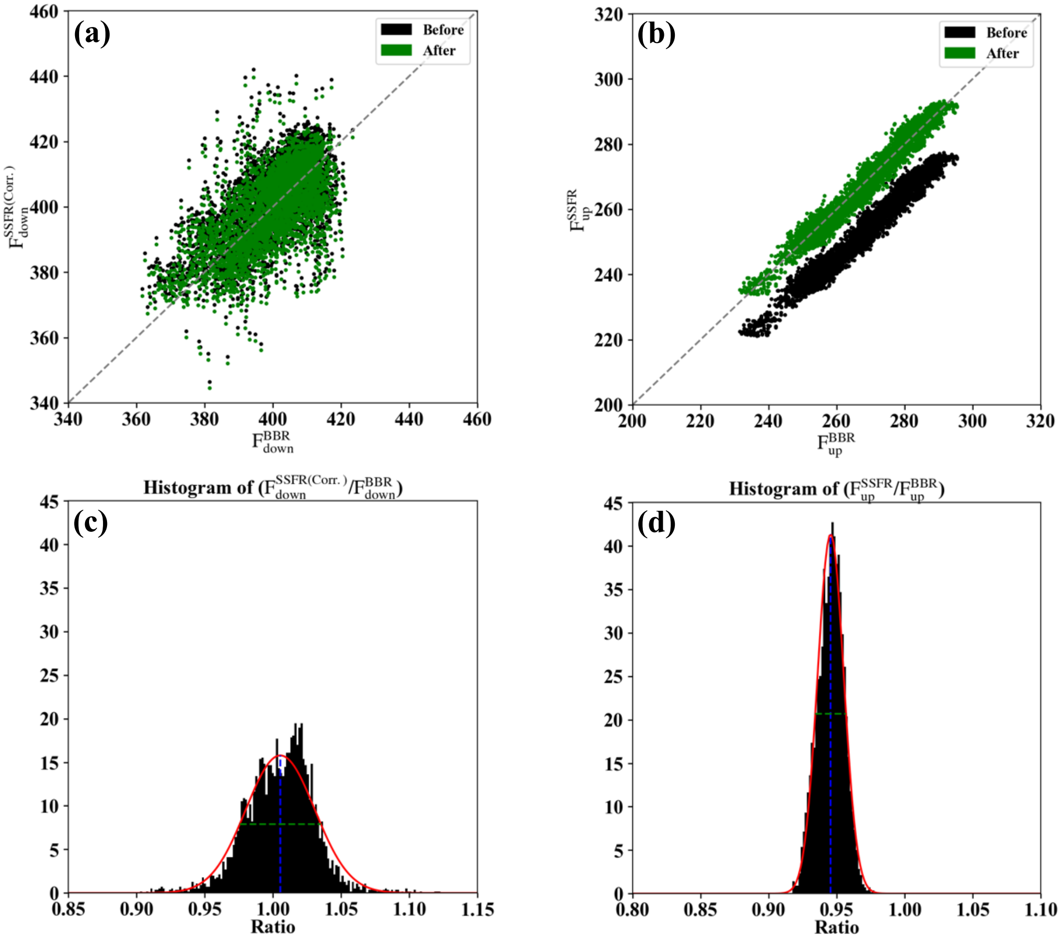

Figure 2.A2. SSFR integrated broadband irradiance versus BBR broadband irradiance (a: downwelling; b: upwelling) and the histograms of the ratio of SSFR integrated broadband irradiance to BBR broadband irradiance (c and d) for the “0911-above-cloud” case. The mean and the full width half maximum of the Gaussian distribution of the ratio are indicated as blue and green dashed lines in the histogram plots. The SSFR-BBR data (SSFR after applying the scale factor as indicated by the blue dashed line) versus BBR is indicated in green in (a) and (b).

2). Snow fraction and surface albedo

When calculating the surface albedo from SSFR-BBR using Equation (2.4), we use the precision as determined above because the uncertainty cancels out for the ratio between the upwelling and downwelling irradiance. The uncertainty estimate of 2.7% for the surface albedo α is then obtained through error propagation using Equation (2.4), where

$$\frac{u(\alpha(\lambda))}{\alpha(\lambda)} = \sqrt{\left(\frac{u(F(\lambda)^{\uparrow})}{F(\lambda)^{\uparrow}}\right)^2 + \left(\frac{u(F(\lambda)^{\downarrow})}{F(\lambda)^{\downarrow}}\right)^2} \tag{2.A6}$$

The uncertainty of the snow fraction described in Section 2.3 is estimated based on two main sources of error:

1. Angle of the field of view (FOV): defined the circular area of the image pixels that were selected for processing;
2. The subdomain size d specified in the adaptive thresholding method described in Appendix 2.C.

When the FOV size mentioned gets too large, pixels affected by the vignette effect and beyond correction is included, which will bias the results. When the FOV size gets too small, we would lose the variation of the snow fraction due to a relative small area. To use as many pixels as possible while avoiding to include contaminated pixels due to vignette effect at the corners, we found the best FOV angle to be 140°. In addition, changing the subdomain size d would slightly change the results. Thus, we obtained 5 sets of snow fraction estimates using FOV angle of 120°, 140°, 160° and a subdomain size d of 1401, 1501, and 1601. Figure 2.A3 shows the 5 sets of snow fractions estimated from nadir camera images using before-mentioned FOV angles and subdomain sizes. The standard deviation of the 5 sets of snow fraction is used as the uncertainties for the snow fraction for each data point.

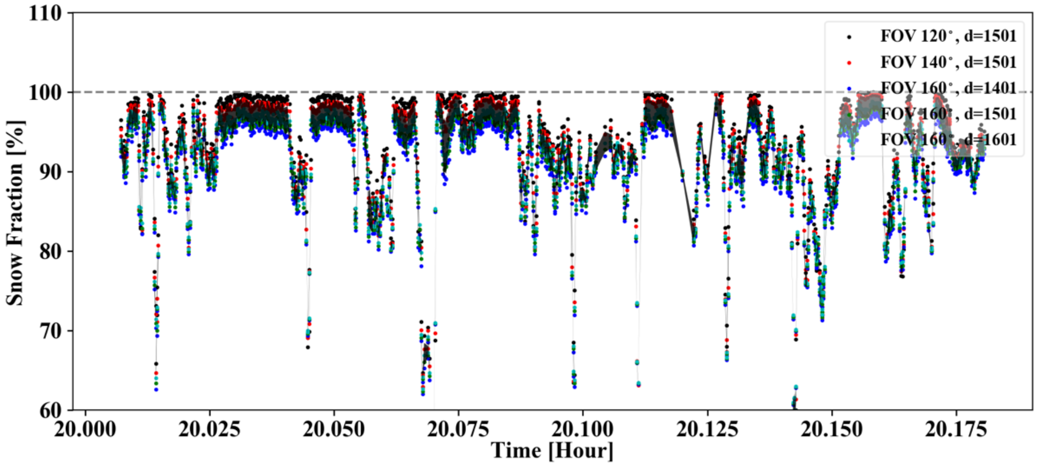

Figure 2.A3. Snow fraction estimated using different FOV angles and subdomain sizes in the adaptive thresholding. The standard deviation of the 5 sets of snow fraction is shaded in black.

3). Radiative transfer calculations

The uncertainty of the radiative transfer (RT) calculations for the "0911-above-cloud" was estimated through the two-stream approximation of the reflectance R

$$R = \frac{\tau+\alpha\cdot(\frac{2\mu}{1-g})}{\tau+(\frac{2\mu}{1-g})} \tag{A6}$$

where τ is the cloud optical thickness, α is the surface albedo, μ is the cosine of the solar zenith angle, and g is the asymmetry parameter. The value of 0.85 is assume for g. In addition, we assume that the two main sources for the uncertainty are from the cloud optical thickness τ and surface albedo α. The uncertainty of R due to the change of τ and α is therefore

$$u(R) = \sqrt{\left(\frac{\partial R}{\partial \tau}u(\tau)\right)^2 + \left(\frac{\partial R}{\partial \alpha}u(\alpha)\right)^2} \tag{A7}$$

This analytical formula allows to calculate uncertainties without numeric radiative transfer calculations.

2.E Atmospheric correction

The following steps describe the atmospheric correction applied to the flight level albedo measured by SSFR-BBR.

1) The spectral flight level albedo from SSFR-BBR (referred to as x_0) was scaled by 0.6, 0.7, 0.8, 0.9, and 1.0 (referred to as y_1, y_2, y_3, y_4, and y_5) – each of these are spectra;
2) Five sets of downwelling and upwelling irradiances were obtained from the RTM by changing surface albedo to y_1, y_2, y_3, y_4, and y_5 while keeping the other model inputs the same;
3) From the five sets of downwelling and upwelling irradiances calculated at flight altitude, we can derive five corresponding flight level albedo x_1, x_2, x_3, x_4, and x_5 using Equation (2.4);
4) The five pairs of $\{x, y\}$ provide a relationship between surface albedo and flight level albedo (nearly linear), $y = ax + b$;
5) The linear relationship was inverted to infer the surface albedo spectrum from the measurements at flight level ($ax_0 + b$).

The atmospheric correction corrected less than 0.2% on flight level albedo at the non-absorbing wavelengths.

2.F Extending spectral surface albedo

To obtain the spectral surface albedo for a wavelength range from 200 nm to 3600 nm, several techniques were performed. Using the spectral surface albedo for “0911-above-cloud” (Figure 2.6) as an example, the following steps were followed:

1) The spectral surface albedo was calculated from Equation (2.5), e.g., with *SF*=76.4% (marked in red in Figure 2.6);

2) In the gas absorption bands (red area in Figure 2.6), the surface albedo was replaced with interpolated values;
3) From 1800nm to 1900nm (yellow area in Figure 2.6), a polynomial fit was used for extrapolation, based on the spectral dependence from 1650 nm to 1800 nm;
4) For the wavelengths shorter than 350 nm and greater than 1900 nm (green area in Figure 2.6), a modeled snow albedo (Wiscombe and Warren, 1981) was used, multiplied with a scale factor to match the measurements at the joinder wavelengths.

3.A Cloud Detection/Identification

Cloudy pixels are identified through a simple thresholding method based on the red, green, and blue channels of MODIS. When the radiance values of the red, green, and blue channels of a pixel are all greater than the corresponding median value, the pixel is considered as cloudy, as illustrated by the following equation

$$\textbf{If}\quad \begin{matrix} Red > Median(Red)\ \& \\ Blue > Median(Blue)\ \& \\ Green > Median(Green) \end{matrix} \begin{cases} \textbf{Yes}, \text{cloudy} \\ \textbf{No}, \text{clear sky} \end{cases} \tag{3.A1}$$

Note that this only works for partially cloud-covered scenes, and may lead to false positives if there is brightness contrast from objects other than clouds. This method was specifically applied for the cases in this paper and should be changed as appropriate for future applications.

3.B Two-Stream Approximation

The two-stream approximation of the reflectance R is calculated using Equation D2 from Chen et al. (2021), as follows:

$$R = \frac{\tau + \alpha \cdot \left(\frac{2\mu}{(1-g)\cdot(1-\alpha)}\right)}{\tau + \left(\frac{2\mu}{(1-g)\cdot(1-\alpha)}\right)} \tag{3.A2}$$

where τ is the cloud optical thickness, α is the surface albedo, μ is the cosine of the solar zenith angle, and g is the asymmetry parameter. A value of 0.85 is assumed for g. The domain average of the solar zenith angle and surface albedo are calculated and used for estimating μ and α. Then, for a range of τ, we calculated the R and obtained the relationship of $R(\tau)$. For those cloudy pixels identified through A1, the inverse relationship of $\tau(R)$ is then used for estimating τ at any given R. Note that this approach does not take into account any cloud reflectance anisotropies.

3.C Parallax Correction

From the satellite's view, the clouds (especially high clouds) will be placed at inaccurate locations on the surface, which have shifted from their actual locations due to the parallax effect. We followed simply trigonometry to correct for it, as follows:

Longitude correction (positive from west to east):

$$\delta lon = \frac{\left(z_{cld} - z_{sfc}\right) \cdot \tan(\theta) \cdot \sin(\phi)}{\pi \cdot R_{Earth}} \times 180° \qquad \text{(B1)}$$

Latitude correction (positive from south to north):

$$\delta lat = \frac{\left(z_{cld} - z_{sfc}\right) \cdot \tan(\theta) \cdot \cos(\phi)}{\pi \cdot R_{Earth}} \times 180° \qquad \text{(B2)}$$

where $(lon_{sat}, lat_{sat}, z_{sat})$ is the satellite location and θ and ϕ (0° at north, positive clockwise) are the sensor viewing zenith and azimuth angles. z_{cld} and z_{sfc} are the cloud top height and the surface height. R_{Earth} is the radius of the Earth. Figure 3.A1 shows an illustration of parallax correction for the black-boxed cloud field in Figure 3.2.

3.D Wind Correction

The wind correction aims at correcting the movement of clouds when advected by the wind between two different satellites' overpasses.

Longitude correction (positive from west to east):

$$\delta lon = \frac{\bar{u} \cdot \delta t}{\pi \cdot R_{Earth}} \times 180° \qquad \text{(B3)}$$

Latitude correction (positive from south to north):

$$\delta lat = \frac{\bar{v} \cdot \delta t}{\pi \cdot R_{Earth}} \times 180° \qquad \text{(B4)}$$

where $\bar{u}$ and $\bar{v}$ are the domain-averaged 10 m zonal and meridional wind speeds, and δt is the time difference between two different satellites that fly on the same orbit. Figure 3.A1 shows the cloud location after applying the parallax (Appendix 3.C) and wind correction for the cloud field in the black box from Figure 3.2.

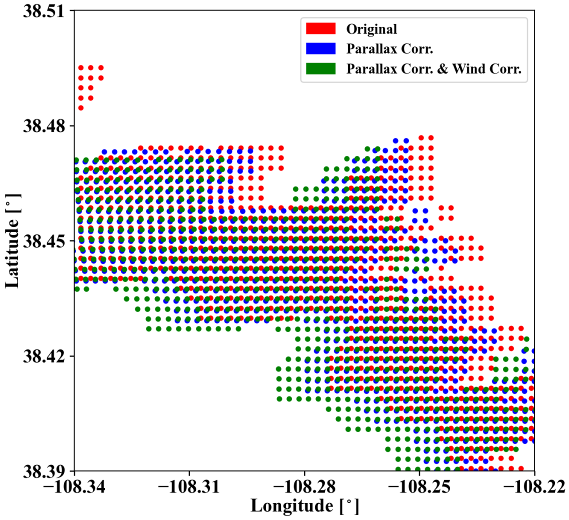

Figure 3.A1. An illustration of correcting cloud location (red) for parallax effect (blue) and wind effect (green) for the black-boxed cloud field in Figure 3.2.

4.A Reflectance and Albedo

From the radiance Rad at the top of the atmosphere (TOA), reflectance can be calculated through the following equation assuming the radiation is isotropic:

$$Ref = \frac{\pi \cdot Rad}{F_{TOA} \cdot \cos(\theta)}$$

where F_{TOA} is the incident irradiance at TOA and θ is solar zenith angle.

From the upwelling and downwelling irradiances of $F_{\uparrow}$ and $F_{\downarrow}$, albedo can be calculated through the following equation:

$$Albedo = \frac{F_{\uparrow}}{F_{\downarrow}}$$